Thermal Behaviour of a Lithium Self-Field Magnetoplasmadynamic Thruster

Kazuki Tojo, '24

Submitted to the
Department of Mechanical and Aerospace Engineering
Princeton University
in partial fulfillment of the requirements of
Undergraduate Independent Work.

Final Report

April 24, 2024

Prof. E. Y. Choueiri
Prof. E. Kolemen
MAE 442
115 pages
reader Copy

This thesis represents my own work in accordance with University regulations.

Abstract

Electric propulsion is the focus of significant research in rocket propulsion due to its high efficiency. However, the high efficiency comes at a cost of low thrust density, and its applications are often limited to low thrust manoeuvres such as station-keeping and attitude control. The magnetoplasmadynamic (MPD) thruster is a form of high power electric propulsion, with the potential to propel heavy-cargo, piloted missions to the Moon and Mars. The Princeton University Electric Propulsion and Plasma Dynamics Laboratory (EPPDyL) is currently collaborating with NASA-JPL to develop lithium MPD thruster technology.

This thesis studies the thermal behaviour of the EPPDyL 30 kW MPD thruster, numerically capturing the conductive and radiative heat transfer during the heat-up phase and thruster firing. The motive is to analyse the structural integrity of the thruster under thermal loads, as well as to investigate future possibilities for cost reductions through material adaptation. The thermal model was generated using ANSYS Steady-State Thermal, and experimental validation of the heat-up phase simulation showed broad agreement of 1.3 % to 19.5 % in magnitude at four thermocouple locations. The behaviour of the thruster during firing was also simulated, finding increased temperatures towards the front of the thruster at the anode nozzle, anode plate and cathode plate relative to the heat-up phase.

The thruster firing procedure is also discussed in detail through an investigation of the lithium handling process. Techniques were explored to improve the safety of thruster firing due to significant risks from the involvement of lithium. Specifically, this thesis seeks to reliably automate the lithium handling glovebox, which must be maintained at a slight positive internal pressure of argon to prevent lithium from reacting with air. A Proportional-Integral-Derivative (PID) pressure control system was designed, developed and implemented using an Arduino, with a pressure transducer to obtain the state (pressure) and a mechanically integrated motor-valve system to control to input (argon flow rate). PID tuning was conducted to optimise the control system and the setup was experimentally verified through dress rehearsals.

Acknowledgements

This thesis is the culmination of my undergraduate degree at Princeton University. None of this would have been possible without the support of those around me, through an unimaginably rewarding journey during which I have been able to grow and learn so much.

I would first like to express my sincere gratitude for Professor Edgar Choueiri, whose wisdom and guidance have instilled a robust habit of rigorous scientific research and communication. I can always rely on your insights to open up new dimensions of scholarly exploration.

As my very first experience in electric propulsion, I would still be learning my ways around the laboratory, both experimentally and theoretically, without the help of Emil Broemmelsiek. From grasping the fundamental principles of the thruster to light conversations about life in general, I have truly appreciated your company during the many hours spent in the laboratory.

Such a multidimensional project was only possible with the help and expertise of various domains. I would like to thank Glenn Northey, Jonathan Prevost and Jeff Addo for IT and technical guidance in machining, microcontrollers and software. I am grateful for Dr. Jay Polk's suggestions with thruster plasma modelling, as well as Professor Luigi Martinelli's general thesis advice throughout the past year.

My sincere appreciation also goes to Professor Howard Stone, whose continued support since sophomore year has been instrumental in the shaping of my journey at Princeton, Oxford and beyond. Discussions with you are always enlightening, whether on research directions or graduate school destinations, and I strive to take inspiration from your guidance in my pursuit for novel scientific discoveries.

Finally, I am deeply indebted to my friends and family for their company as I navigated this challenging adventure, halfway across the world in a continent I had never been to prior. I will forever cherish the daily dose of laughter with my friends who welcomed me so warmly upon my return from Oxford. As for my family, I would not be where I am now without your relentless love and ruthless drive to constantly strive for better, through both difficult and joyous times.

Thank you all so much for being a part of this journey. This memorable time at Princeton has truly changed my life. As I dream towards ambitious endeavours, I hope I can repay the same love and happiness.

"Earth is the cradle of humanity, but one cannot live in a cradle forever."
— Konstantin E. Tsiolkovsky

Contents

List of Tables

List of Figures

List of Abbreviations

ADC Analogue-to-Digital Converter. 55, 74

ANLG Analogue. 55

CAD Computer-Aided Design. xii, 2, 6, 7, 16, 21, 30, 32, 33, 44, 51, 52

DC Direct Current. 55

ECD Encoder. 55

EP Electric Propulsion. 1, 3, 4, 6, 28, 40, 70, 71

EPPDyL Electric Propulsion and Plasma Dynamics Laboratory. iii, x, 1, 5–10, 16, 24, 25, 39–41, 66, 70, 71

GND Ground. 55

GRC Glenn Research Center. 6

IR InfraRed. 13, 14, 20

JPL Jet Propulsion Laboratory. iii, 1, 5, 6, 28, 40, 41, 70, 71

LiLFA Lithium Lorentz Force Accelerator. vi, x, xi, 1, 2, 5, 7–9, 11, 14–19, 21, 25, 35, 40–43, 46, 70

MAI Moscow Aviation Institute. 5

MFC Mass Flow Controller. xii, 48

MPD MagnetoPlasmaDynamic. iii, vi, x, 1, 4–6, 11, 17, 70

NASA National Aeronautics and Space Administration. iii, 1, 5, 6, 28, 40, 41, 70, 71

PID Proportional-Integral-Derivative. iii, vii, ix, xii, xiii, 9, 47, 48, 50, 53–55, 57, 63–70, 72–74, 97

PLA Polylactic Acid. 52

PPE Personal Protective Equipment. x, 8, 10

PWM Pulse Width Modulation. 54, 73

USD United States Dollars. 68, 69, 72, 74

List of Symbols

α	Absorptivity	
$\dot{m}$	Mass flow rate of propellant	$\mathrm{kg\,s^{-1}}$
ϵ	Emissivity	
κ	Thermal conductivity	$\mathrm{W\,m^{-1}\,K^{-1}}$
λ	Mean free path	m
ϕ	View factor for grey bodies	
ϕ	Work function	eV
ρ	Density	$\mathrm{kg\,m^{-3}}$
ρ	Resistivity	$\Omega\,\mathrm{m}$
σ	Stefan-Boltzmann constant	$5.67 \times 10^{-8}\mathrm{W\,m^{-2}\,K^{-4}}$
τ	Thrust	N
τ	Transmissivity	
θ	Valve angle	$^\circ$ / rad
A	Area	$\mathrm{m^2}$
A	Richardson constant	$\mathrm{A\,m^{-2}\,K^{-1}}$
c	Specific heat capacity	$\mathrm{J\,kg^{-1}\,K^{-1}}$
D	Channel diameter	m
d	Rod diameter	m
e	Error	psi/Pa
F	View factor for blackbodies	
F_{ext}	External force	N
G	Transfer function	

I	Current	A
J	Current density	$\mathrm{A\,m^{-2}}$
k_B	Boltzmann constant	$1.3806\,\mathrm{J\,K^{-1}}$
K_D	Derivative coefficient of PID	
K_I	Integral coefficient of PID	
K_n	Knudsen number	
K_P	Proportional coefficient of PID	
L	Lorenz number	$2.45 \times 10^{-8}\mathrm{W\,\Omega\,K^{-2}}$
M	Mass of vehicle	kg
m	Mass	g / kg
M_f	Final mass of vehicle	kg
M_i	Initial mass of vehicle	kg
m_p	Mass of expended propellant	kg
M_r	Molecular weight	$\mathrm{g\,mol^{-1}}$
n	Number of moles	mol
P	Pressure	psi / Pa
Q	Heat	J
q	Heat flux	$\mathrm{W\,m^{-2}}$
R	Ideal gas constant	$8.314\,\mathrm{J\,K^{-1}\,mol^{-1}}$
r	Molecular radius	m
r	Set point	psi / Pa
s	Complex frequency	
T	Temperature	°C / K
t	Time	s
U	Internal energy	J
u	Input	° / rad
u_e	Exhaust velocity of propellant	$\mathrm{m\,s^{-1}}$
u_i	Initial velocity of propellant	$\mathrm{m\,s^{-1}}$
V	Voltage	V

V	Volume	m^3
v	Velocity of vehicle	$\mathrm{m\,s}^{-1}$
v_f	Final velocity of vehicle	$\mathrm{m\,s}^{-1}$
v_i	Initial velocity of vehicle	$\mathrm{m\,s}^{-1}$
W	Work	J
x	Distance	m
y	Output	psi/Pa

Chapter 1

Introduction

Currently, electric propulsion (EP) is widely used in the space industry due to its high efficiency. Whilst its low thrust density has often limited its applications to small-thrust manoeuvres such as attitude control, station-keeping and primary propulsion systems of small spacecraft, development has resulted in increasing thrust density throughout the years. Amongst many forms of EP, magnetoplasmadynamic (MPD) thrusters achieve the highest thrust density, as high as 10^5 N m^2 [1], and possess the potential for high-thrust applications in piloted, heavy-cargo missions to the Moon and Mars.

A steady-state model of the MPD thruster is the Lithium Lorentz Force Accelerator (LiLFA), which ionises lithium propellant and accelerates the ions with the Lorentz force induced by a self-field magnetic field. The Princeton Electric Propulsion and Plasma Dynamics Laboratory (EPPDyL) operates a 30 kW LiLFA thruster and the National Aeronautics and Space Administration's (NASA) Jet Propulsion Laboratory (JPL) is developing MPD thrusters of higher power.

1.1 Motive

Capturing the thermal behaviour of a setup is important in many fields. Thermal analyses of electric thrusters are of particular interest as thruster firings involve extremely high temperatures. On a high level, it is critical that the thruster maintains structural integrity for consistent performance. It is also worthwhile to investigate the mounting surface temperature and thereby the thruster's impact on other components of the spacecraft. A thermal analysis also allows for exploration of future possibil-

ities, such as material substitution for cost reduction and adjustments to cooling mechanisms. Ideally, experimental verification is conducted through thruster firing for stronger confidence in the validity of a numerical model.

1.2 Principle of Thruster Thermal Analysis

The principle of this thermal analysis lies in conduction and radiation. As electric thrusters operate in the vacuum of space, this condition is recreated in a vacuum tank and reflected in the negation of convection. Once computational simulations are performed to capture the heat transfer during nominal conditions, parameters can subsequently be altered to explore further possibilities.

1.3 Goal

The objective is to capture, with high fidelity, the thermal behaviour of the LiLFA. Numerical simulations on the computer-aided design (CAD) model of the thruster will be conducted to obtain the steady-state temperatures across the setup due to conduction and radiation. In addition, experimental validation of the thermal simulations will be explored, with an investigation to improve the lithium handling aspect of the experimental procedure. Specifically, the aim is to improve the safety of the lithium handling glovebox.

Chapter 2

Literature Review

2.1 Electric Propulsion

Broadly, EP operates by ionising the propellant and accelerating the ions by manipulating electric and magnetic fields. It is a field of aerospace engineering that has, and is currently ongoing, rapid research and development. This is largely due to the fact that EP technology achieves propulsion efficiencies unmatched by conventional chemical propulsion by ejecting the propellant at significantly higher velocities. This coupling of propellant exhaust velocity and propulsion efficiency can be demonstrated with the Rocket Equation.

The Rocket Equation can be derived [2] starting with an equation of motion for rocket propulsion,

$$M\frac{dv}{dt} = \tau + F_{ext}, \tag{2.1.1}$$

where M is the vehicle mass, v is its velocity and τ is the thrust. F_{ext} is any external force in parallel with the direction of motion, which will be neglected considering the vacuum and microgravity conditions of space.

The thrust can be obtained from momentum change as $\tau = \dot{m}(u_e - u_i)$, where u_e is the propellant exhaust velocity and $\dot{m}$ is the propellant mass flow rate. The propellant initial velocity, u_i, will be taken as zero. Equation 2.1.1 is then expressed as

$$M\frac{dv}{dt} = \dot{m}u_e. \tag{2.1.2}$$

By setting the mass flow rate equal to the rate of change of mass of the entire vehicle,

and with some rearranging and integration, Equation 2.1.2 develops to

$$M\frac{dv}{dt} = -u_e\frac{dM}{dt}, \tag{2.1.3}$$

$$\int_{M_i}^{M_f}\frac{dM}{M} = -\frac{1}{u_e}\int_{v_i}^{v_f} dv, \tag{2.1.4}$$

$$\frac{M_f}{M_i} = e^{-\frac{\Delta v}{u_e}}. \tag{2.1.5}$$

Equation 2.1.5 is Tsiolkovsky's Rocket Equation, where M_f and M_i are the final and initial vehicle masses, and v_f and v_i are the final and initial vehicle velocities. It is preferable to express this equation in terms of the propellant mass fraction $\frac{m_p}{M_i}$, where m_p is the total mass of expended propellant. This means that $M_i = M_f + m_p$, allowing Equation 2.1.5 to become

$$\frac{m_p}{M_i} = 1 - e^{-\frac{\Delta v}{u_e}}. \tag{2.1.6}$$

This expression clarifies the physical meaning of the Rocket Equation, which is that, by increasing the propellant exhaust velocity, u_e, it is possible to exponentially decrease the propellant mass fraction and therefore the propellant mass required for a particular manoeuvre.

With EP, it is possible to achieve propellant exhaust velocities well beyond $10\,\mathrm{km\,s^{-1}}$, whereas the value for chemical propulsion averages around $3\,\mathrm{km\,s^{-1}}$ [2]. In fact, ion thrusters using xenon propellant can perform at up to $u_e = 90\,\mathrm{km\,s^{-1}}$ [2]. As such, EP has become a critical technology for space exploration and is currently a significant focus of rocket research.

2.1.1 Magnetoplasmadynamic Thrusters

Amongst various forms of EP thrusters, which all generate thrust through different methods, the self-field MPD thruster (Fig. 2.1) is unique in its ability to produce the highest thrust density of up to $10^5\ \mathrm{N\,m^{-2}}$ [1].

The underlying structure of the MPD thruster is a coaxial geometry, with a central cathode, an annular anode and an interelectrode insulator [1]. Gaseous propellant is fed through the thruster channel, where it is ionised with an electric arc in the interelectrode gap. These ions are then accelerated downstream by an azimuthal magnetic field and exhausted as plasma, generating thrust. The force responsible for

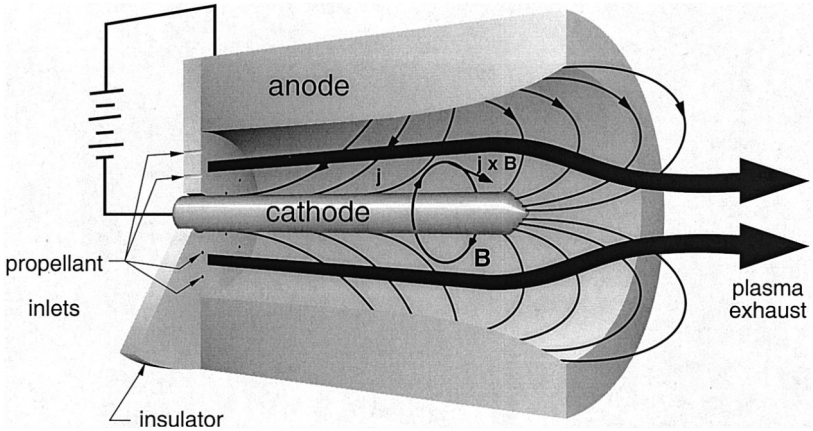

Figure 2.1: Schematic of the MPD thruster. From Jahn and Choueiri (2002) [1].

this acceleration is the Lorentz force.

The MPD thruster is capable of operating at specific impulses from 1500 s to 8000 s [1]. It has demonstrated efficiencies of over 40 %, although high efficiency, defined as > 30 %, is possible only at high power levels of over 100 kW [1]. In theory, even higher efficiencies can be achieved, with Choueiri determining a theoretical limit of 79.8 % for lithium MPD thrusters under nominal operating conditions [3].

There are two broad forms of the MPD thruster: applied-field and self-field. EP-PDyL currently operates a 30 kW self-field MPD thruster. It is also known as the LiLFA and is fuelled by lithium propellant, based on original design developed by the Moscow Aviation Institute (MAI) with NASA in 1995 [4].

Currently, the MPD thruster is largely limited by its high power requirement and cathode erosion rates [1]. However, with the development of nuclear power generation in space, NASA-JPL has identified MPD technology as a promising solution to high power and high efficiency propulsion to the Moon and Mars.

2.2 Thermal Analysis

Thermal analysis is an integral component of a vast majority of engineering design projects. It is critical that a design can withstand the heat transfer involved to operate as reliably and efficiently as intended. Beyond nominal operation, engineering projects often face a trade-off between heat management and design redundancy, which means that high quality heat analysis has the potential to eliminate excessive redundancy and reduce costs.

In particular, thermal analysis of space technology is of special importance due to

the harsh environments of space. In the vacuum environment of space, temperatures can range extremely widely, and internal heat generation from flight hardware poses further challenges to thermal control. Thrusters operate at especially high temperatures, often around the range of 2000 °C to 3000 °C as shown by simulations in later sections. Finally, reliability in the thermal management of space technology is critical as mission duration is typically of several years, and in many missions it is not possible to service broken hardware after launch.

2.2.1 Electric Propulsion Modelling

There is thorough documentation in the literature of thermal modelling for EP. These simulations are typically motivated by specific heat transfer issues, and commonly performed numerically using computational software such as ANSYS, NX and Thermal Desktop.

Reilly et al. at NASA-JPL performed a thermal analysis of the 100 kW X3 Hall thruster [5]. The X3, being a nested Hall thruster with three channels in a concentric arrangement [5], posed challenges with regard to thermal modelling due to its unique structural geometry. To capture the heat transfer between multiple heat generating components, the NX steady-state thermal program was used. A mesh was created from the imported mechanical drawing file of the thruster, and analysis was conducted. This numerical analysis was validated with experimental data using thermocouples. It was found that, whilst the steady-state assumption was valid for most components, it resulted in significant temperature discrepancies for several other components [5]. This may have been due to the effects of an insulator plate not reflected in the CAD model [5].

Van Noord at NASA Glenn Research Center (GRC) conducted a similar analysis on the NEXT ion thruster [6]. The primary purpose of the thermal model was to support the prediction of component temperatures during various missions. Whilst the paper does not explicitly mention the name of the software, it explains that the modelling and mesh generation was done with "commercially available thermal software." [6] In comparison to experimental tests on the NEXT Prototype Model 1 thruster, the numerical simulation returned temperatures within 5 °C to 10 °C for most components.

Likewise, Hollingsworth used a commercial software, COMSOL, to analyse thermal and static loads of an orificed graphite cathode for the argon-fed MPD thruster in EPPDyL [7]. The exact meshing process was not depicted in the thesis, although it

is clear that a CAD geometry was imported into COMSOL Multiphysics and used to perform the numerical calculations [7]. Whilst the thruster was fired experimentally, validation of the thermal modelling was not presented.

Finally, Emsellem et al. at Princeton University's EPPDyL have conducted a thermal analysis of an alternative LiLFA in an attempt to investigate heat transfer issues that arose with the open lithium heat pipe implemented as the propellant feeding system [8]. The 100 kW LiLFA in this study is different to the 30 kW LiLFA currently operated in EPPDyL. The study used ANSYS and its roughest meshing setting to perform the numerical simulation, and thermocouple experimental verification upon thruster firing revealed disagreements of $\leq 5.1\,\%$ for all components except for the anode lip, which differed by $8.5\,\%$ [8].

2.3 Experimental Thruster Firing

Firing the LiLFA is an extremely logistically intensive procedure. A significant contribution to this is the easily reactive and therefore hazardous nature of lithium. This lithium propellant must be fed into the thruster with a controlled flow rate and temperature, melting from a solid and evaporating into a gas through the process [9]. The heat involved in the high power 30 kW operation of the thruster is also a challenge, as it can only be cooled through conduction and radiation in the vacuum environment [9]. The whole procedure relies on five broad systems to operate effectively, almost symbiotically: feed system, thermal control, thruster control, vacuum system and lithium handling [9]. This entire setup in EPPDyL is shown in Figure 2.2.

The feed system is responsible for injecting lithium propellant into the thruster setup at a specified constant flow rate [9]. The objective of thermal control is to melt the lithium propellant for the feed system, as well as to manage the temperature of temperature-sensitive components [9]. Thruster control involves managing the firing of the thruster, including current control [9]. The vacuum system (Fig. 2.3) brings the tank down to an operational level of vacuum and relies, sequentially, on the roughing pump, the roots blower and the diffusion pump. The three pumps respectively operate in different pressure ranges, and contribute consecutively to achieve the final vacuum pressure in the region of 10^{-5} Torr [9]. Finally, lithium handling consists of lithium safety management, propellant loading and tank cleaning post-firing [9].

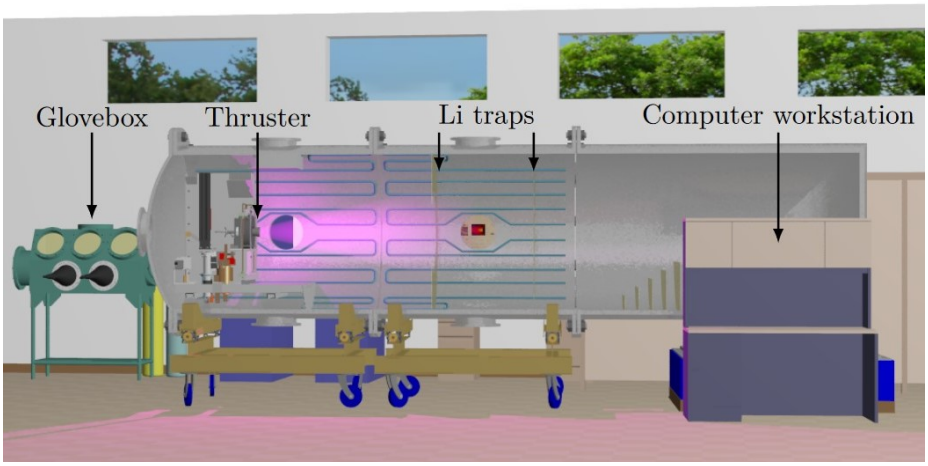

Figure 2.2: The entire LiLFA setup in EPPDyL. From Coogan (2018) [10].

2.3.1 Lithium Handling Glovebox

Lithium reacts violently with water, and the chemical reaction is as follows [9]:

$$\mathrm{Li} + \mathrm{H_2O} \longrightarrow \mathrm{LiOH} + \frac{1}{2}\,\mathrm{H_2} + 508\,\mathrm{kJ\,mol^{-1}}. \tag{2.3.1}$$

All three products are dangerous for different reasons. LiOH is extremely corrosive, H_2 is explosive and $508\,\mathrm{kJ\,mol^{-1}}$ of heat is generated from this highly exothermic reaction [9].

A glovebox (Fig. 2.4) is used for a significant portion of lithium handling. The glovebox is essentially a small vacuum chamber, used to fill with argon to create an inert environment to handle lithium in. It has three chambers: the main chamber, the ante chamber and the gloveport [9].

The main chamber is the largest chamber, and it is where lithium propellant is handled. To prevent the reaction of lithium with air, this chamber must be maintained at a slight positive gauge pressure whenever lithium is being handled within [9]. This is a significant safety risk, and the glovebox operation protocol requires one other individual in addition to the glovebox operator to monitor the pressure gauge and ensure a slight positive gauge pressure by controlling the argon inflow. For reference, when handling lithium that has reacted with air post-firing, the EPPDyL protocol is to wear personal protective equipment (PPE) and a respirator, as seen in Figure 2.5.

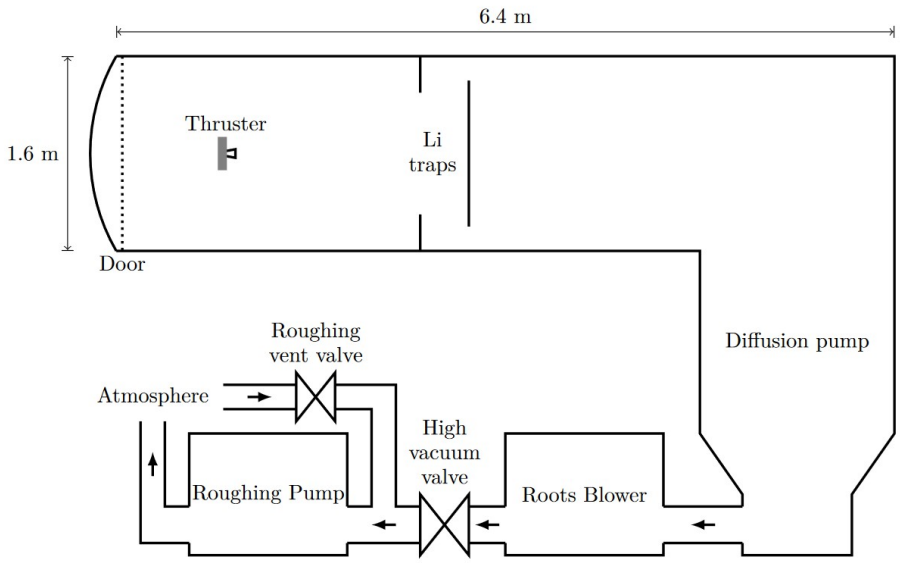

Figure 2.3: The internal schematic of the LiLFA vacuum tank. From Coogan (2018) [10].

2.4 Research Question

This thesis examines the research question, "What is the thermal behaviour of the EPPDyL LiLFA thruster?" Furthermore, it investigates the design question, "How could we improve the safety of the lithium handling process?"

The thermal behaviour of the EPPDyL LiLFA thruster is not yet understood, and quantifying its heat transfer will enable the exploration of thruster thermal improvements. We approach this by performing numerical thermal simulations using ANSYS Steady-State Thermal. Additionally, the safety of the lithium handling process is critical to ensure successful firing of the thruster. We examine this by developing a Proportional-Integral-Derivative (PID) pressure controller to maintain a slight positive argon gauge pressure in the lithium handling glovebox, preventing the hazardous reaction of lithium and air.

Figure 2.4: The glovebox in EPPDyL.

Figure 2.5: The PPE and respirator worn to clean lithium reaction products post-firing. From Lev and Stein (2011) [9].

Chapter 3

Thermal Behaviour of the LiLFA

3.1 Principles of Heat Transfer in MPD Thrusters

The heat transfer involved in the firing of an MPD thruster is defined by conduction and radiation. Convection is assumed to be negligible in the vacuum environment of space. Specifically for spacecrafts and spacecraft components, radiation is the dominant form of heat exchange between the spacecraft and the environment, and conduction is responsible for internal heat exchange between spacecraft components [11]. With regard to the LiLFA, both radiation and conduction are significant internally, especially due to the heat transfer from the heater to the rest of the body.

The foundation of radiation and conduction, as well as convection, lies upon the first law of thermodynamics, which states that the rate of change of internal energy of a system is equal to the heat flow into the system minus the work done by the system [11]. This can be expressed by

$$Q - W = \frac{dU}{dt}, \tag{3.1.1}$$

where Q is the heat flow into, W the work done by and U the internal energy of the system.

3.1.1 Conduction

The principle of conduction begins with Fourier's law of thermal conduction:

$$\dot{Q} = -\kappa A \frac{dT}{dx}, \tag{3.1.2}$$

where κ is thermal conductivity, A is area and T is temperature. It is often expressed in terms of heat flux, $q \equiv \frac{\dot{Q}}{A}$, and vectorially for isotropic materials, such that

$$\boldsymbol{q} = -\kappa \boldsymbol{\nabla} T. \tag{3.1.3}$$

With Equation 3.1.3, it is possible to see the physical meaning of Fourier's law that the heat flux is negatively proportional to the temperature gradient.

To consider internal heat generation, $g(\boldsymbol{r}, t)$, it is possible to apply Gauss' law and the law conservation of energy to obtain the governing equation [12] [13],

$$\nabla^2 T(\boldsymbol{r}, t) + \frac{g(\boldsymbol{r}, t)}{\kappa} = \frac{\rho c}{\kappa} \frac{\partial T(\boldsymbol{r}, t)}{\partial t}, \tag{3.1.4}$$

where specific heat capacity, c, and density, ρ, are introduced. This governing equation (Eqn. 3.1.4) also includes the thermal diffusivity term, $\frac{\kappa}{\rho c}$, whose physical meaning refers to the rate at which temperature change diffuses through a material [11].

Whilst analytical solutions of Equation 3.1.4 are desirable to obtain the exhaustive temperature distribution of an object, such solutions are only practical for simple geometries. In reality, it is most common to work towards numerical solutions, commonly performed by industrial software such as ANSYS in recent years. These software implement a finite-element approach, discretising complex objects into numerous nodes of simple geometries.

3.1.2 Radiation

Radiation is the energy emitted through electromagnetic waves by any surface above 0 K. It does not require a medium to travel through and is therefore the sole form of heat exchange between spacecraft components and their vacuum surroundings [11]. In such an environment, radiative heat transfer is a function of the emitting and receiving bodies':

1. temperatures,

2. absorptivity and emissivity,

3. relative geometry. [11]

The principle of radiation is founded upon the behaviour of a blackbody. A blackbody does not reflect or transmit incident waves—instead, it is a perfect radiator and absorber of all incident wavelengths and angles [11]. However, in reality, surfaces are not blackbodies and their radiative behaviour are dependent on several properties, one of which is emissivity. Emissivity, ϵ, is typically a function of wavelength, λ, and it is possible to obtain the total radiated power of a body by implementing it in the numerator of Planck's equation and integrating over all wavelengths [11]. Alternatively, if emissivity is taken to be a constant, the same integration leads to the Stefan-Boltzmann equation [11]:

$$q = \epsilon \sigma T^4, \tag{3.1.5}$$

where q is the radiant flux, $\sigma = 5.67 \times 10^{-8} \mathrm{W\,m^{-2}\,K^{-4}}$ is the Stefan-Boltzmann constant and T is absolute temperature. It should be noted that the emissivity for a blackbody is 1.

For thermal management of a spacecraft, there must be consideration for two separates bands of radiation. The solar wave band captures the energy emitted by the sun, whilst the infrared (IR) wave band covers heat transferred within and from the spacecraft. As this thesis' focus is on the thruster's thermal behaviour, it is sufficient to limit analysis to the IR wave band.

To determine the energy balance for a thruster, it is first necessary to obtain the absorptivity, defined as the ratio of absorbed power to incident power, and emissivity in the IR wave band for all involved surfaces [11]. In equation form, the definition of absorptivity, α, is

$$\alpha \equiv \frac{Q_{abs}}{Q_{inc}}. \tag{3.1.6}$$

Furthermore, Kirchhoff has demonstrated that the absorptivity and emissivity of a particular surface for a particular wavelength are equal [11]:

$$\alpha(\lambda) = \epsilon(\lambda). \tag{3.1.7}$$

These two equivalent values are determined starting with the experimental measurement of a parameter called reflectivity, ρ. It is also useful to understand the

parameter of transmissivity, τ. The experimental measurement of ρ is straightforward, and the definitions of ρ and τ are

$$\rho \equiv \frac{Q_{ref}}{Q_{inc}}, \tag{3.1.8}$$

$$\tau \equiv \frac{Q_{trans}}{Q_{inc}}, \tag{3.1.9}$$

where Q_{ref} is the reflected power and Q_{trans} is the transmitted power. After applying the conservation of energy and normalising all terms by Q_{inc}, the result is

$$\alpha + \rho + \tau = 1. \tag{3.1.10}$$

Since all surfaces of the thruster are opaque, meaning that $\tau = 0$, emissivity and absorptivity are calculated as

$$\epsilon = \alpha = 1 - \rho. \tag{3.1.11}$$

To calculate the emissivity over the entire IR wave band, the result from Equation 3.1.11 is applied to the explicit form of Equation 3.1.6 [11]:

$$\epsilon_{IR} = \frac{\int_0^\infty [1 - \rho(\lambda)] e_b(\lambda) d\lambda}{\int_0^\infty e_b(\lambda) d\lambda}. \tag{3.1.12}$$

This result (Eqn. 3.1.12) is typically solved numerically by

$$\epsilon_{IR} = \frac{\sum_1^n [1 - \rho(\lambda_i)] e_b(\lambda_i)}{\sigma T^4}, \tag{3.1.13}$$

where the denominator is evaluated as the energy emission from a blackbody of the same temperature and $e_b(\lambda_i)$ depicts the total power density of centre λ_i within the wavelength band [11]. As such, it is possible to see that ϵ_{IR} is a function of temperature, which is an important consideration as thrusters typically operate across large temperature ranges. As an example, the cooled mounting surface of the LiLFA is at 22 °C, whilst the heater can reach temperatures above 3000 °C.

It is usually sufficient to assume that spacecraft components have diffuse-grey surfaces, meaning that the emissivity and absorptivity are independent of angles of incidence and emission [11]. The net heat transfer between two surfaces, from surface 1 to surface 2, at respectively different temperatures, T_1 and T_2, is evaluated as the energy transferred from surface 1 to surface 2 minus the energy transferred from

surface 2 to surface 1:

$$Q_{12} = \epsilon_2 \sigma T_1^4 F_{12} A_1 - \epsilon_1 \sigma T_2^4 F_{21} A_2. \tag{3.1.14}$$

In Equation 3.1.14, F_{ij} is the view factor term, which captures the relative geometry and orientation between two surfaces. The view factor satisfies reciprocity, $F_{ij}A_i = F_{ji}A_j$, and normalisation, $\sum_{i=1}^{n} F_{ij} = 1$ for $j = 1$ to $j = n$ [11].

It should be noted that Equation 3.1.14 assumes that both surface are blackbodies, where $\epsilon_1 = \epsilon_2 = 1$, in the sense that it does not capture the infinite reflections of incident energy between the two surfaces. Using the reciprocity of the view factor, Equation 3.1.14 can be simplified to

$$Q_{12} = \sigma F_{12} A_1 (T_1^4 - T_2^4). \tag{3.1.15}$$

It is possible to develop Equation 3.1.15 beyond blackbodies for applicability to grey bodies by broadening the view factor to cover the geometry, configuration, emissivity and reflectivity of the surfaces. The physical meaning of this more general form of the view factor, ϕ_{ij}, is the fraction of energy emitted from surface 1 that is ultimately absorbed by surface 2, whether directly or after a number of reflections. Equation 3.1.15 can then be rewritten as

$$Q_{12} = \sigma \phi_{12} A_1 (T_1^4 - T_2^4). \tag{3.1.16}$$

Whilst the calculation of view factors F_{ij} and ϕ_{ij} are not particularly complex, there is inherently an extremely large number of such calculations that must be performed to account for the surfaces involved in the complex geometries of spacecraft components. As a result, this process is often done by computational software, through a finite-difference approach similar to that of conduction in Section 3.1.1.

3.1.3 Thruster Structure and Composition

The self-field LiLFA thruster (Fig. 3.1 & 3.2) is of simpler structure and composition than an applied-field thruster as it does not require an external magnet.

The whole thruster is mounted on a molybdenum base, underneath which exists a water-cooled MACOR® plate. The cooling power is approximately 0.5 GPM to 1.0 GPM at room temperature, the equivalent of 32 mL s^{-1} to 63 mL s^{-1} at 22 °C.

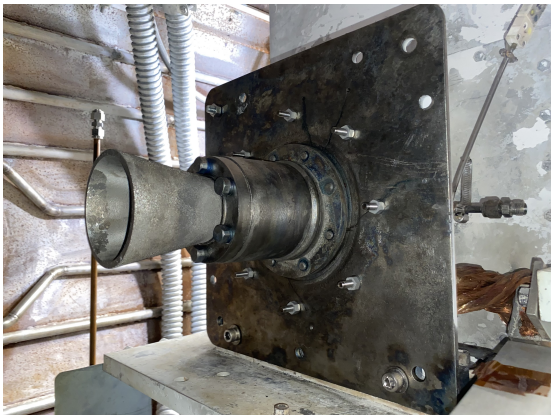

Figure 3.1: Image of the front of the LiLFA thruster, mounted inside the EP-PDyL vacuum tank.

Figure 3.2: Image of the back of the LiLFA thruster, mounted inside the EP-PDyL vacuum tank.

The thruster itself consists of an inner tungsten cathode and an outer tungsten anode, respectively connected to a molybdenum back cathode plate and a molybdenum front anode plate, separated by a hexagonal boron nitride electrical insulator. Within the cathode shell is a tungsten vaporiser, heated from the inside by a graphite heater. The cathode shell is also connected to a tungsten feed pipe, through which lithium propellant is fed between the vaporiser and the cathode shell. The vaporised lithium then travels through multi-channel tungsten rods at the tip of the cathode for thermionic emission, before exiting the cathode and out of the nozzle. The entire setup is fastened by molybdenum nuts, bolts, rods and washers, with the exception of alumina shelf washers used to electrically separate but structurally integrate the anode and cathode plates.

A CAD model of the overall thruster is available in Figure 3.3, as well as a cross-section view in Figure 3.4. Alternatively, there is also a labelled cross-section schematic in Figure 3.5, whilst Figure 3.6 zooms into the tungsten multi-channel cathode rods. Finally, during analysis of the ANSYS temperature distribution results in later sections, the locations labelled in Figures 3.7 and 3.8 will be focused upon.

3.1.4 Thermal Conductivity and Emissivity

The operation of the LiLFA thruster is steady-state, meaning that thermal equilibrium is attained during its firing. The two defining parameters of this equilibrium are thermal conductivity, κ, and emissivity, ϵ. Each material holds a unique, temperature-dependent thermal conductivity, and each surface possesses a unique, temperature-

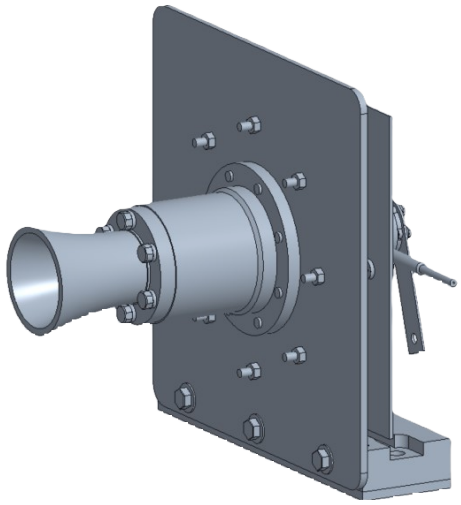

Figure 3.3: CAD model of the LiLFA thruster.

dependent emissivity. The thruster is composed of six different materials: molybdenum, alumina, tungsten, graphite, hexagonal boron nitride and MACOR®. A thorough literature review was conducted to obtain all temperature dependent values of κ and ϵ.

Molybdenum is the material used for the majority of components on the thruster. The reason for this is its high melting point of 2622 °C [14], which is the sixth highest amongst all natural elements. Due to the high temperatures involved in the firing of an MPD thruster, molybdenum is suitable for many components. The thermal conductivity of molybdenum is available in a 1960 paper by Rasor and McClelland [15] from 810 °C to 2604 °C. However, as the thruster begins heating at room temperature, it is useful to understand the thermal properties below 810 °C as well. As such, the Wiedemann-Franz law was used to determine the rest of the temperature-dependent thermal conductivity values as a function of resistivity, ρ [15]:

$$\kappa = L\frac{T}{\rho}, \tag{3.1.17}$$

where $L = \frac{\pi^2 k^2}{3e^2} = 2.45 \times 10^{-8} \mathrm{W\,\Omega\,K^{-2}}$ is the Lorenz number. The temperature-dependent resistivity of molybdenum was taken from Northcott (1956) [16]. Northcott also included temperature-dependent emissivity values from 1000 K to 2895 K. The compiled thermal conductivity and emissivity of molybdenum are presented in Figures 3.9 and 3.10.

Alumina is sparsely used on the thruster in the form of shelf washers. Its property

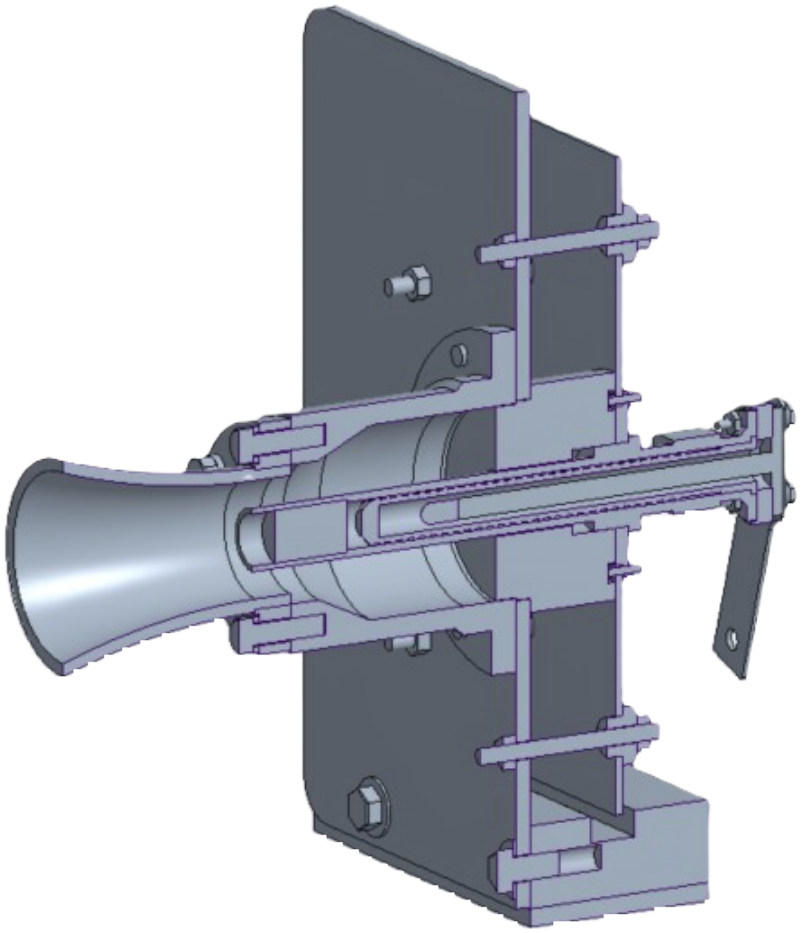

Figure 3.4: Cross-section CAD model of the LiLFA thruster.

as an electrical insulator is desirable to separate the potentials of the anode and cathode plates. Thermal conductivity values were taken from Dörre and Hübner (1984) [17] for a temperature range of 20 °C to 1895 °C, and emissivity values from Bauer et al. (2005) [18] for a temperature range of 201 °C to 1200 °C. These findings are plotted in Figures 3.11 and 3.12.

Tungsten is another critical material within the thruster, also for its high melting point which, at 3414 °C, is even higher than that of molybdenum. It is used for the cathode shell, cathode rods, vaporiser and anode nozzle, all components subject to high temperatures. The thermal conductivity and emissivity of tungsten is well documented over a large range of temperatures. Thermal conductivity data was obtained for 1 K to 3000 K from Hust and Lankford (1984) [19], whilst emissivity data was collected for 400 K to 3600 K from Lassner and Schubert (1999) [20]. These data are presented in Figures 3.13 and 3.14.

The graphite used for the heater is of a particular grade called AXM-5Q. It is

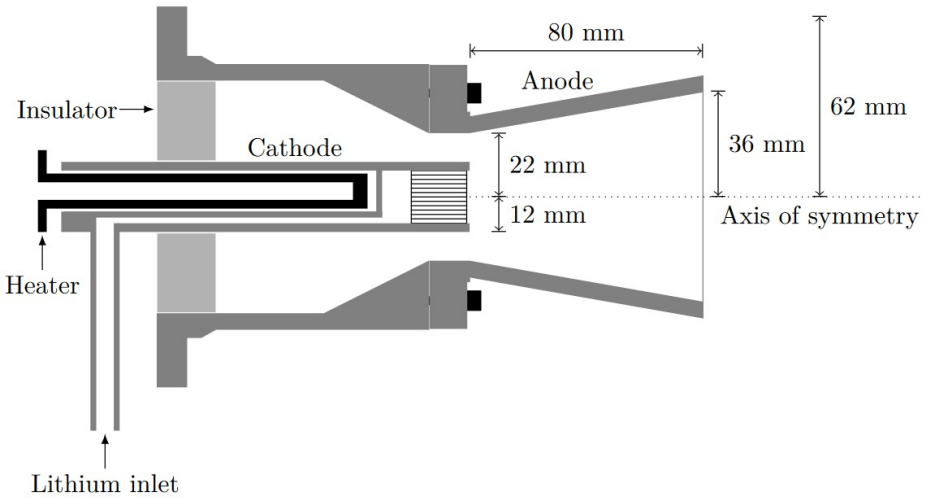

Figure 3.5: Labelled cross-section schematic of the LiLFA thruster.

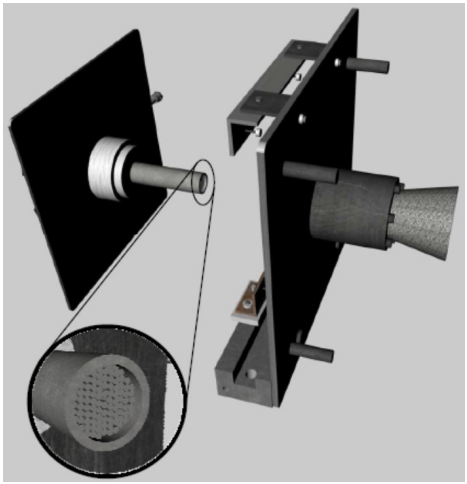

Figure 3.6: Zoomed-in schematic of the multi-channel cathode rods.

manufactured by Entegris and holds a melting point of 3500 °C [21]. The material brochure includes thorough documentation of various properties of AXM-5Q, including thermal conductivity and emissivity. From the brochure [21], thermal conductivity values from 28 °C to 1630 °C, as well as emissivity values from 1800 K to 2900 K, were retrieved. These values are plotted in Figures 3.15 and 3.16.

Similarly, the grade of hexagonal boron nitride is known as BN99, manufactured by QS Advanced Materials [22]. The material is advantageous in its ability to act as a good thermal conductor whilst also being a strong electrical insulator. However, it was challenging to obtain reliable temperature-dependent thermal conductivity and emissivity data of BN99. As such, the values used are constant in temperature, with

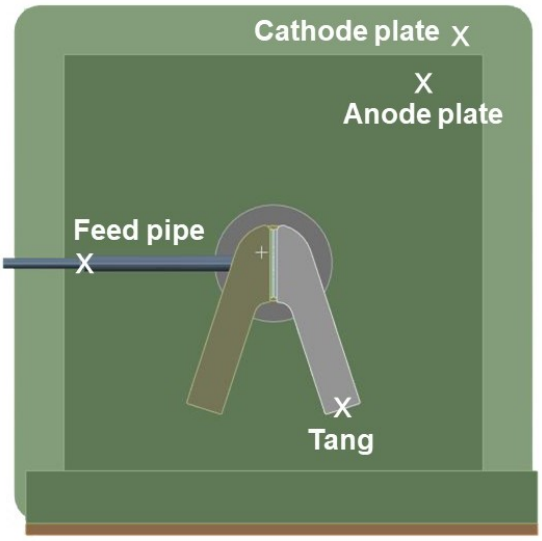

Figure 3.7: Foci of temperature distribution analyses on the back of the thruster.

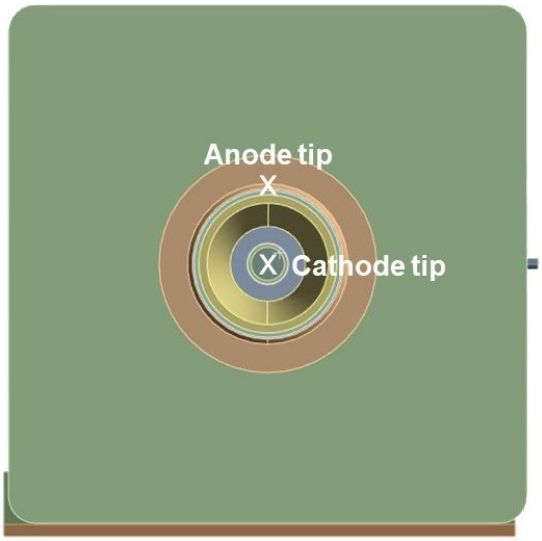

Figure 3.8: Foci of temperature distribution analyses on the front of the thruster.

$\kappa = 40\,\mathrm{W\,m^{-1}\,K}$ [22] and $\epsilon = 0.86$ [23]. The value for emissivity was taken from Chen et al. (2021), where the emissivity of hexagonal boron nitride was found to be at least 0.86 in the IR wave band [23].

Finally, MACOR® is a machinable glass ceramic manufactured by Corning [24], known for its low thermal conductivity. Specifically, the thermal conductivity is plotted in Figure 3.17 from 24 °C to 800 °C, obtained from Corning's MACOR® specification [24]. With regard to emissivity, a study by Cardone et al. determined a value of 0.934 [25]. No temperature-dependent emissivity could be found.

Unfortunately, the computer running the ANSYS simulation had insufficient memory to implement temperature-dependent emissivity. Instead, a technique similar to the Newton-Raphson method was used to iterate through a range of temperature-constant emissivity values until the results converged at the correct temperature. However, the computation time of each simulation was too long to perform large numbers of iterations, meaning this iterative technique still had room for improvement. The ANSYS Steady-State Thermal program also linearly interpolates between data points. There is no extrapolation performed. Rather, the material property value of the data point at the closest temperature is used beyond the provided range. The individual data points on Figures 3.9-3.16 are those entered as tabular data in ANSYS, also available in Tables A.1-A.9.

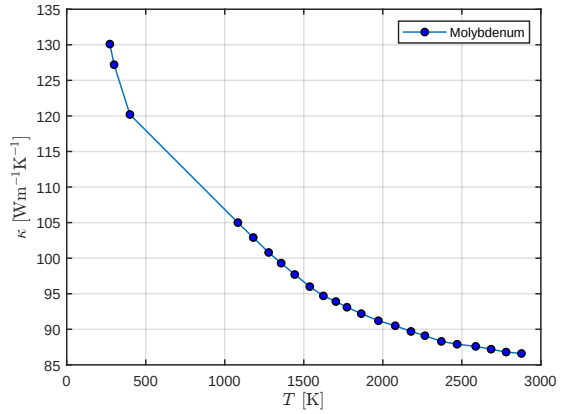

Figure 3.9: Temperature-dependent thermal conductivity of molybdenum.

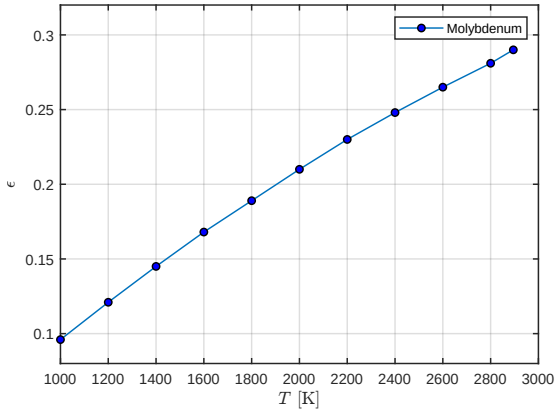

Figure 3.10: Temperature-dependent emissivity of molybdenum.

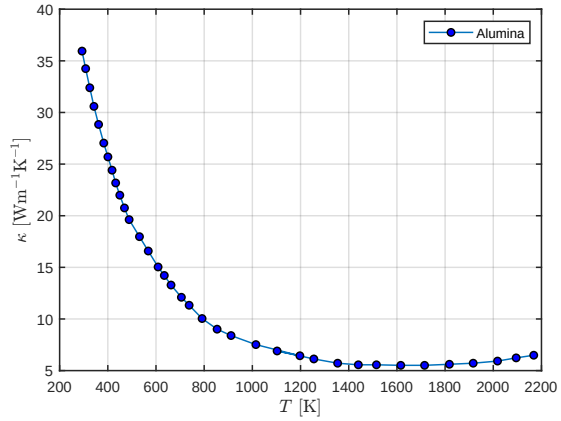

Figure 3.11: Temperature-dependent thermal conductivity of alumina.

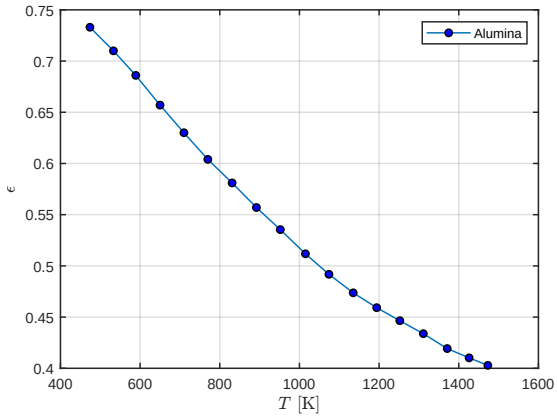

Figure 3.12: Temperature-dependent emissivity of alumina.

3.2 Experimental Methods

3.2.1 Setup

ANSYS Steady-State Thermal

All simulations were performed using ANSYS Steady-State Thermal, set up from ANSYS Workbench and operated within ANSYS Mechanical Enterprise. It is not necessary to perform any transient analyses as the LiLFA operates in steady-state. A detailed CAD model of the thruster was imported into ANSYS, after which materials were assigned to each component. Temperature-dependent material properties from Section 3.1.4 were entered manually into the program.

The ANSYS software implements a finite-difference approach, as outlined theo-

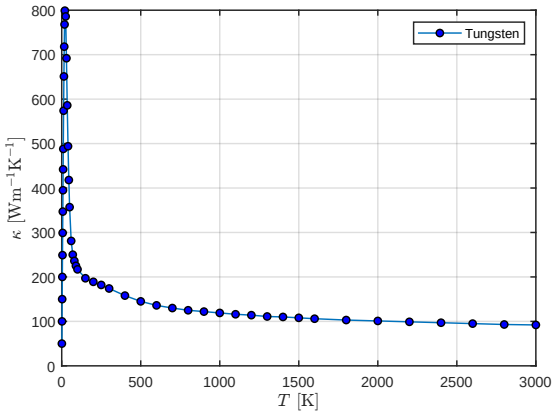

Figure 3.13: Temperature-dependent thermal conductivity of tungsten.

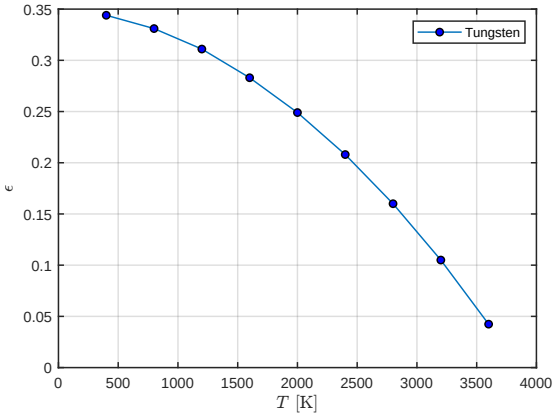

Figure 3.14: Temperature-dependent emissivity of tungsten.

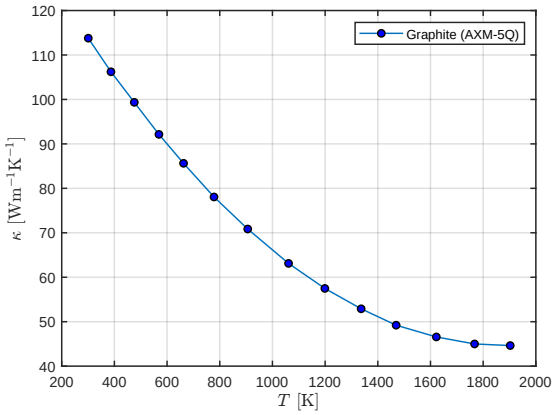

Figure 3.15: Temperature-dependent thermal conductivity of graphite (AXM-5Q).

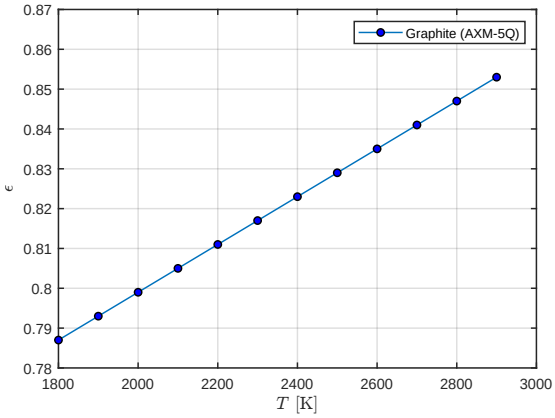

Figure 3.16: Temperature-dependent emissivity of graphite (AXM-5Q).

retically in Sections 3.1.1 and 3.1.2, by meshing an object into incremental nodes and performing calculations between each of them. Due to the steady-state nature of this analysis, it is possible to perform all calculations with inputs of geometry, meshing, thermal conductivity and emissivity. This captures view factor calculations, the details of which are available within the program by analysing the Solver Output tab.

Thruster Mesh

The thruster meshing process was performed largely automatically by ANSYS Mechanical, with global meshing controls selected manually to achieve an optimal balance between meshing quality and simulation time. In particular, careful attention

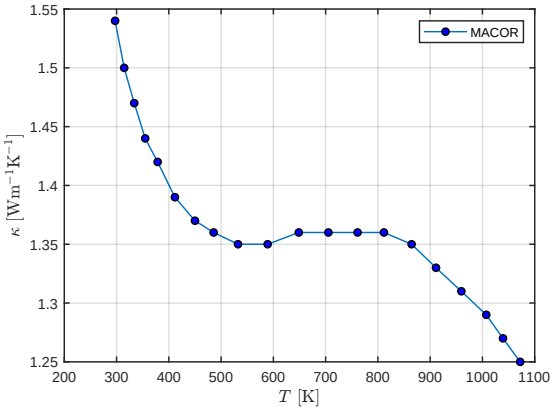

Figure 3.17: Temperature-dependent thermal conductivity of MACOR®.

was paid to small and detailed parts such as the nuts, bolts, rods and washers, as well as the complex geometry of the vaporiser.

With regard to global meshing settings, several parameters were varied from the default selection:

1. The transition setting was changed from Fast to Slow. This parameter defines the rate at which node sizes change, meaning this change ensured a more gradual transition between nodes of large size differences.

2. The span angle centre was changed from Coarse to Fine. In doing this, it was ensured that angles in the corner of elements were more mild.

3. The initial size seed was set to a Part-by-Part seeding approach, such that smaller parts get a finer mesh than their larger counterparts.

4. The error limits were set to Aggressive Mechanical to set higher standards for element shaping such that they are closer to the ideal geometry.

5. The smoothing parameter was set to High to allow for local node refinement after the initial mesh iteration.

Whilst the element size was also decreased throughout the testing process, it was ultimately reverted back to the default size to minimise the computation time. Thorough testing by Emsellem et al. found that rough mesh sizes are sufficient for ANSYS thermal analyses, and the effects of a decreased element size was not noticeable [8]. The final global mesh settings are available in Figure B.1, as well as a plot of the element quality distribution in Figure 3.18. The resultant quality distribution is generally of high standard, with the distribution heavily skewed towards 1. Visually, the

final external meshing is displayed in Figure 3.19 and the vaporiser meshing is shown in Figure 3.20.

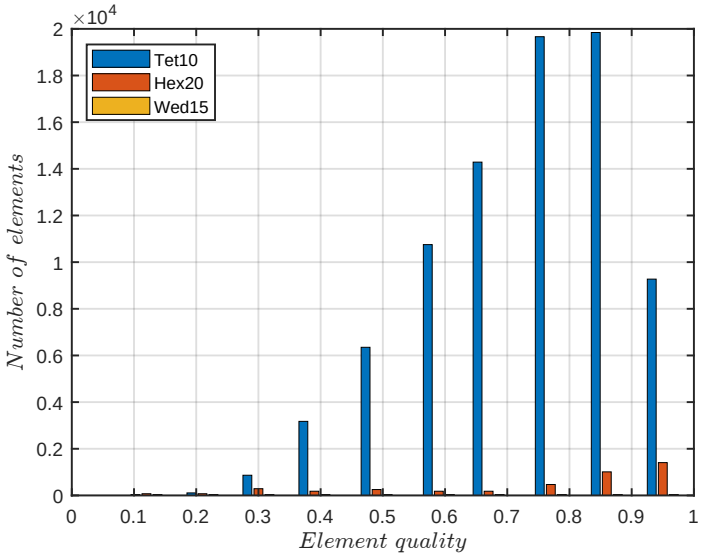

Figure 3.18: Quality distribution of the mesh elements. Tet10, Hex20 and Wed15 are different solid element geometries. The number of Wed15 elements is non-zero but extremely small relative to Tet10 and Hex20.

3.3 Preliminary Simulation

To start the thermal analysis, a preliminary investigation was set up, inspired by the problem simulated by Emsellem et al. in 1999 [8].

The paper, also coming out of EPPDyL, worked to address a heat transfer issue persisting in a different Lorentz force accelerator. With the multi-channel cathode tip operating at well below the boiling point of lithium, the lithium vapor would condense in the cathode before exiting [8]. As such, a set of closed heat pipes were installed. However, due to thermal sinks, the heat pipes did not operate properly and an ANSYS simulation was set up to study the nature of the heat sinks. The numerical model proved to be successful, leading to the eventual successful firing of the thruster [8].

3.3.1 Boundary Conditions

The boundary conditions imposed by Emsellem et al. for their thermal problem were as follows. First, the cathode component located under the cathode heater was set to

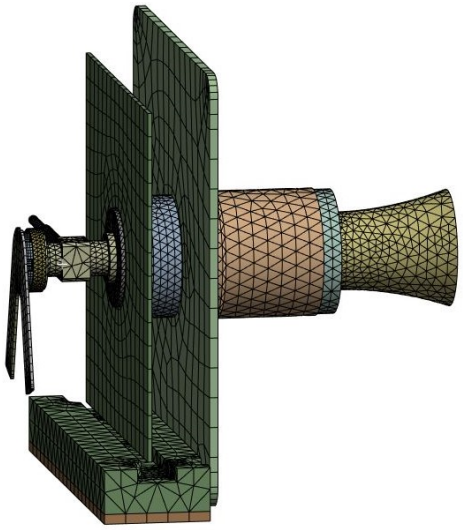

Figure 3.19: Meshing of the whole thruster.

a constant temperature of 1720 °C [8]. Second, the outer border of the cooled power leads were set to a constant temperature of 25 °C [8]. Finally, all surfaces were covered to emit radiation to ambient space at 25 °C, with no surface-to-surface radiation [8].

Whilst there are some insufficiencies to these boundary conditions, it served as a solid starting point to prepare for more complex problems. Some adaptations were made for simulation on the current LiLFA. The bottom surface of the actively cooled MACOR® plate was set to the EPPDyL room temperature of 22 °C, and a constant temperature of 1720 °C was set to the heater itself. Importantly, these boundary conditions were preliminary, although they provided key insights for the purpose of developing towards higher fidelity problems. The boundary conditions are visualised in Figures 3.21 and 3.22.

3.3.2 Results

This preliminary analysis returned results to validate key performance criteria of ANSYS thermal modelling. The temperature profile is shown in Figures 3.23 and 3.24, where it is possible to see significant heating at the heater and conductive heat transfer to the rest of the thruster. Especially from the cross-section view (Fig. 3.24), it is clear that there was no radiative heat transfer from the heater to the vaporiser. This is consistent with the simulation setup, where radiative surfaces were only set to emit to ambient space.

Quantitatively, the maximum temperature was 871 °C at the heater, along with a minimum of 22 °C at the bottom of the MACOR® plate. The temperature of the

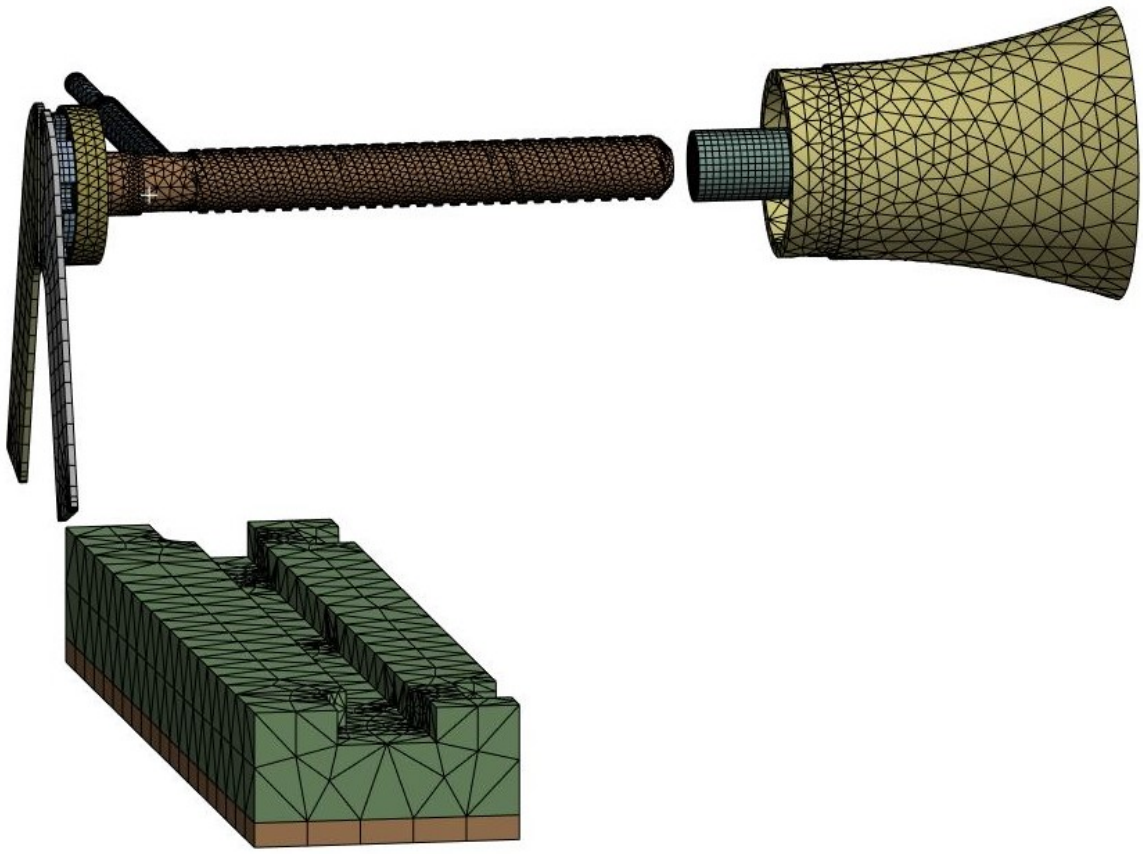

Figure 3.20: Meshing of the vaporiser.

heater rod contradicts with the constant temperature boundary condition of 1720 °C imposed on its surface. The exact reason behind this phenomenon could not be identified within the timeline of this thesis, but one possibility could be the influence of imperfect mesh geometries on local calculations. Whilst there was the option of investigating higher quality element sizes and geometries, it was deemed infeasible for the timeline of this project for two reasons. First, mesh creation in itself is a sophisticated area of study. Second, and more practically, a finer mesh would have significantly increased the computation time of each simulation, which already exceeded 3 hours.

Temperatures at other key locations were in broad agreement with the temperatures obtained by Emsellem et al., which ranged from 580 °C at the anode lip to 580 °C on the insulator ring by the backplate [8]. At the transition between the thick and thin sections of the feed pipe, the temperature was 346 °C. The ends of the molybdenum heater tangs were at 466 °C, whilst the top left corner of the cathode plate was at 204 °C. The top left corner of the anode plate was slightly cooler at

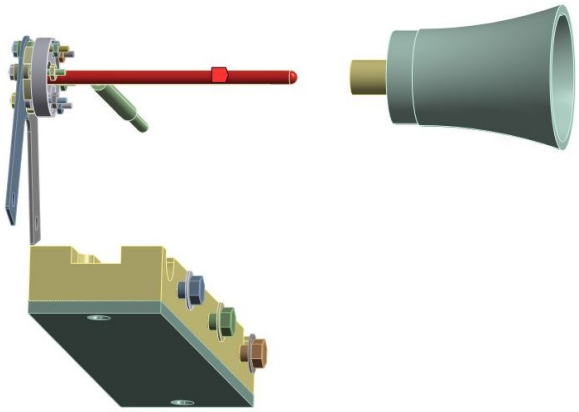

Figure 3.21: Preliminary boundary condition of constant temperature 1720 °C applied to the heater rod.

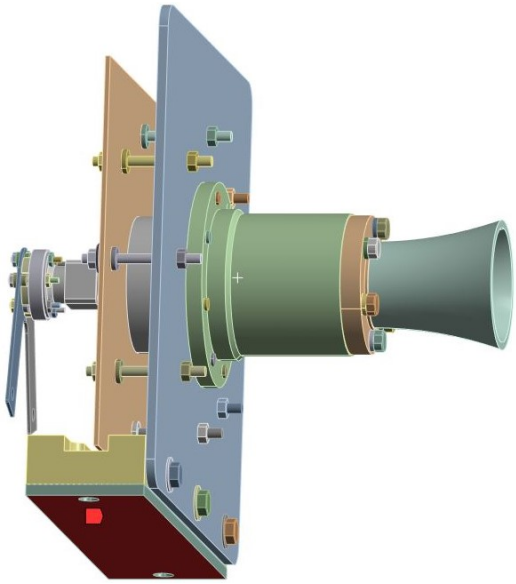

Figure 3.22: Preliminary boundary condition of constant temperature 22 °C applied to the bottom surface of the cooled MACOR® plate.

176 °C, and the anode tip was at 175 °C. Finally, the cathode tip was at 217 °C and the temperature profile on the vaporiser approximately ranged from 220 °C to 260 °C. These are all consistent with the fact that no radiative heat was transferred from the heater to the vaporiser.

Overall, this preliminary analysis was critical in verifying a nominal performance of the broader steady-state thermal analysis program, particular with regard to conduction.

3.4 Heat-Up Phase: Initial Simulation

A simulation was then set up to model the heat-up phase of the thruster, built on the foundations formed by the preliminary investigation in Section 3.3. The heat-up phase refers to the steady-state condition of the thruster when its heater is turned on without the ignition of plasma. In ideal conditions, the heater produces sufficient heat to raise the temperature of the vaporiser above the boiling point of lithium. This heat transfer occurs through a combination of radiation, directly from the heater to the vaporiser, and conduction, indirectly to the back of the heater and forward through an electrical insulator. The exact material of this insulator is not documented, and an

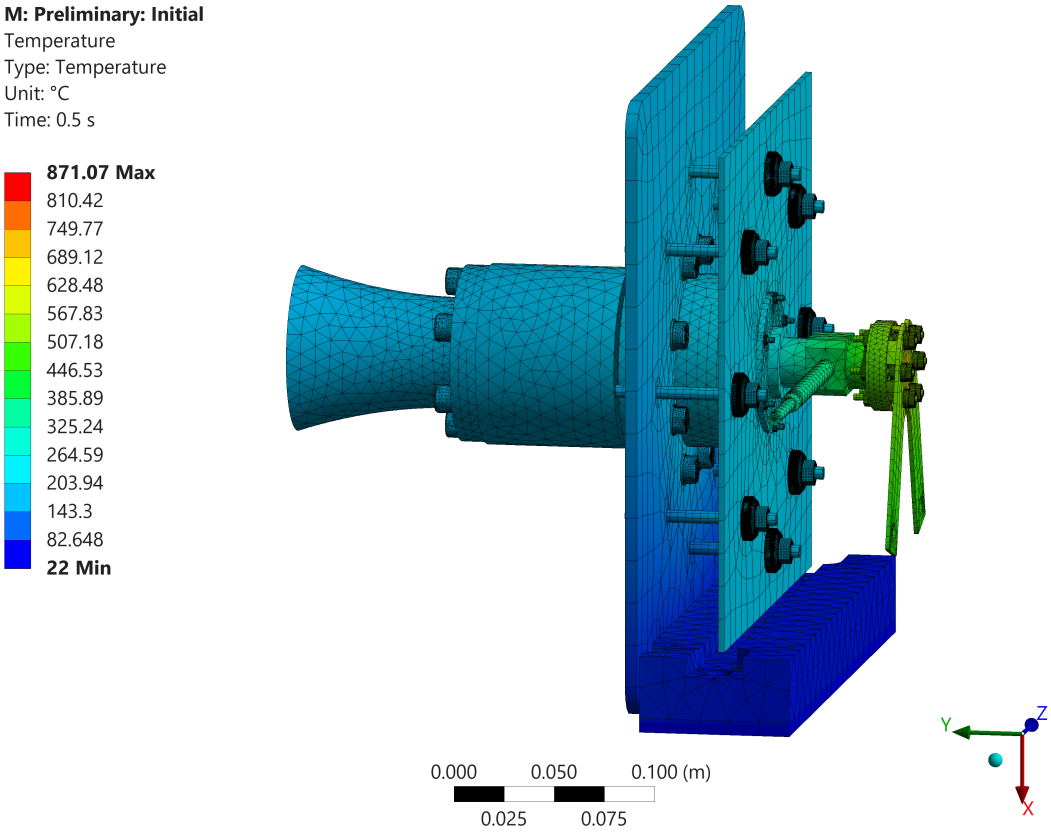

Figure 3.23: Temperature distribution results of the preliminary simulation over the whole thruster.

educated assumption was made for hexagonal boron nitride as the insulator between the cathode and anode plates is of the same material.

Two significant changes were made in preparation for this heat-up analysis. First, the thruster geometry was simplified to reduce the simulation time by minimising the total node count. Specifically, nuts, bolts, rods and washers were removed from the design, and the remaining holes were filled in. This also significantly reduced points of simulation failure, especially with the complex contact surfaces involved with small parts. There was confidence in the validity of this simplification as the EP team at NASA-JPL also implements similar modifications to their thermal simulations. The CAD model of the simplified thruster is available in Figures 3.25 and 3.26.

Second, the radiation emitted from the thruster surfaces was changed from ambient radiation to surface-to-surface radiation. This was the most critical change implemented, as radiation between surfaces is a significant contributor of internal heat transfer within the thruster, particularly between the heater and the vaporiser. Since there are no perfectly enclosed volumes within the thruster, the enclosure type

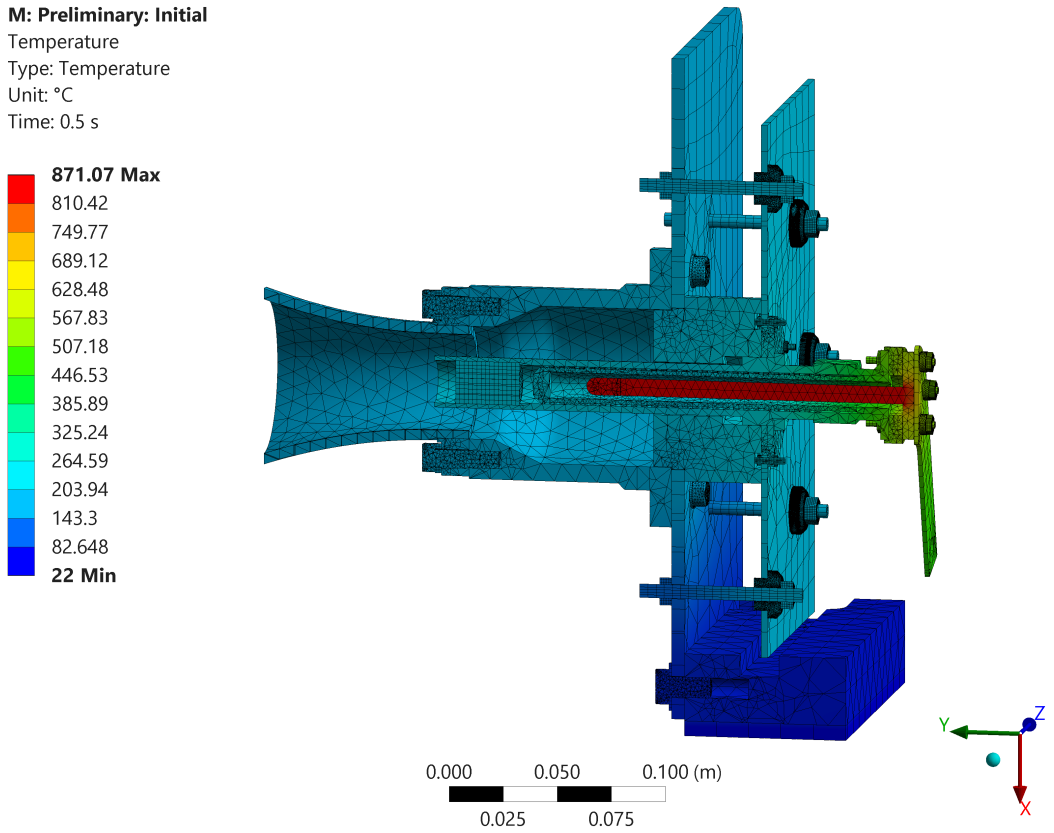

Figure 3.24: Temperature distribution results of the preliminary simulation across a cross-section of the thruster.

was set to Open to allow for radiation waves to escape into ambient space if reflections resulted in such trajectories. ANSYS computes all such reflections, capturing both waves absorbed internally within the thruster and those emitted into ambient space.

The implementation of surface-to-surface radiation was of slight concern during early tests, as the vaporiser appeared not to be receiving sufficient thermal energy from the heater. However, a fundamental plate-to-plate problem was set up to confirm this radiative heat transfer. As such, there is confidence in the proper operation of surface-to-surface radiation during this initial analysis of the heat-up phase.

3.4.1 Boundary Conditions

A slight modification was made the boundary conditions from the preliminary simulation. Instead of the constant 1720 °C temperature clamped on the heater rod surface, an area heat flux was applied to the same surface to progress towards higher fidelity. The heat flux was set to 4×10^6 W m^{-2}, which equates to a total heater

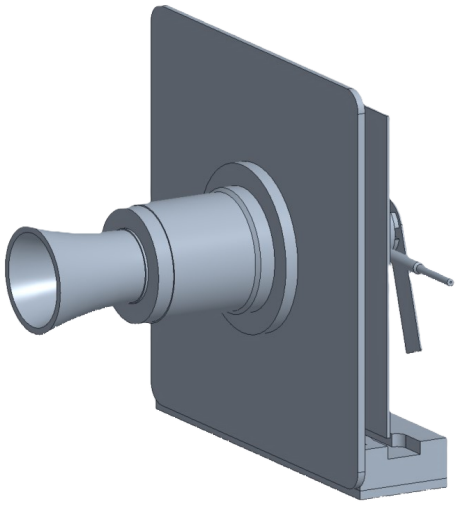

Figure 3.25: CAD model of the simplified thruster.

power of 22.6 kW given the heater rod surface area of 5.64×10^{-3} m^2 from the CAD model. The cooling boundary condition of the MACOR® bottom surface remained unchanged from 22 °C.

3.4.2 Results

This initial simulation of the heat-up phase significantly improved in fidelity upon the preliminary analysis in Section 3.3. By implementing surface-to-surface radiation, the behaviour of the heater in particular was substantially different. The resultant temperature distribution is available in Figures 3.27 and 3.28.

Due to boundary conditions with more thermal input, the temperature exhibited at key thruster locations were significantly higher than the preliminary investigation. The thin-thick transition of the feed pipe was at 766 °C, whilst the ends of the tangs were at 1011 °C. Furthermore, the top left corner of the cathode plate was at 780 °C, with the top left corner of the anode plate at 726 °C. The anode tip was at 645 °C. Finally, the central tip of the multi-channel cathode rods were at 1171 °C, and the temperature profile over the vaporiser ranged from 1430 °C to 1800 °C.

It is particularly interesting to analyse the cross-section results (Fig. 3.28) as they exhibit key characteristics of radiative heat transfer. The heater itself ranges from 2704 °C at the tip of the rod, to around 3230 °C in the middle, to 2052 °C at the back of the rod. Instead of solely conductive dissipation through the back of the thruster and forward through the boron nitride insulator, there was also significant direct heating of the vaporiser through radiation. As such, the vaporiser achieves a

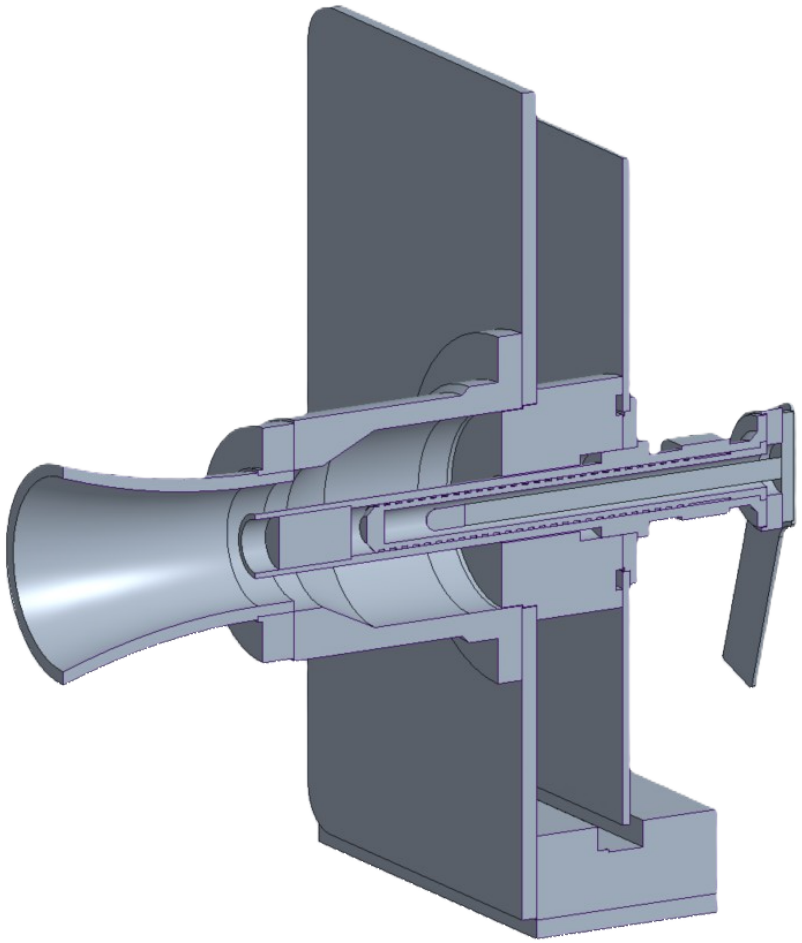

Figure 3.26: Cross-section CAD model of the simplified thruster.

peak temperature of 1781 °C at a location that correlates to the front of the heater rod.

As a whole, this initial analysis of the heat-up phase was an important first step towards a high fidelity model. Some refinements were made subsequently to achieve a more accurate simulation.

3.5 Heat-Up Phase: Refined Simulation

The heat-up phase model was refined upon analysis of the initial results in Section 3.4. In particular, three key changes were implemented.

First, the area heat flux on the heater was adapted to a volumetric heat flux. This achieves higher fidelity, as the heater operates by conducting current through its cross sections with the resistivity of graphite. The current runs internally and generates

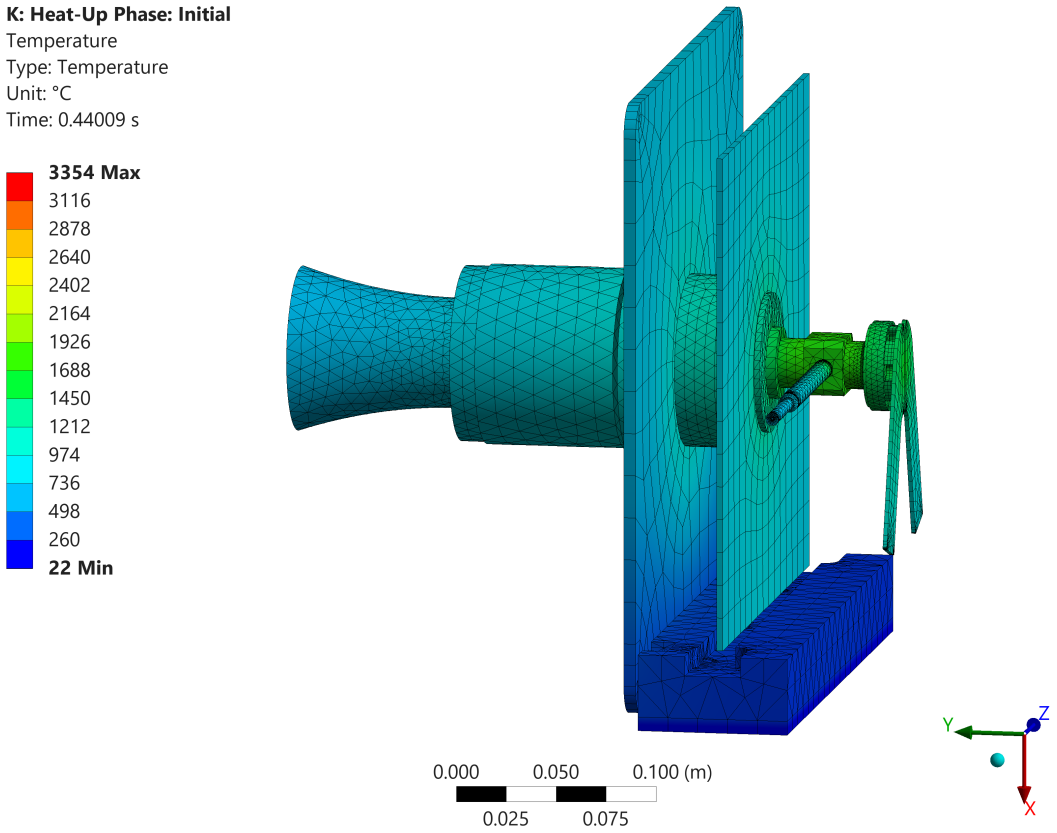

Figure 3.27: Temperature distribution results of the initial heat-up phase simulation over the whole thruster.

heat across the entire cross section, not just on the outer edges. Therefore, it is more accurate to model this heat generation with a volumetric heat flux as opposed to an area heat flux.

With the implementation of a volumetric heat flux, it was no longer possible to apply the heat flux solely to the heater rod and not the back plate. The more accurate modelling technique is to generate heat within the rod but not the back plate, as the significantly larger cross section of the back plate results in substantially less relative heat generation. As such, the thruster CAD model was adjusted to figuratively separate the heater rod and the heater back plate, in order to apply internal heat generation to the rod but not the back plate. Physcially, the rod and the back plates were still in direct contact.

Finally, the goal of this refined simulation was to ensure temperatures across the vaporiser surface of at least the boiling temperature of lithium, 1342 °C [26]. During full operation of the thruster, the lithium propellant must be fully vaporised at the vaporiser stage before reaching the multi-channel cathode rods. Whilst a sufficient

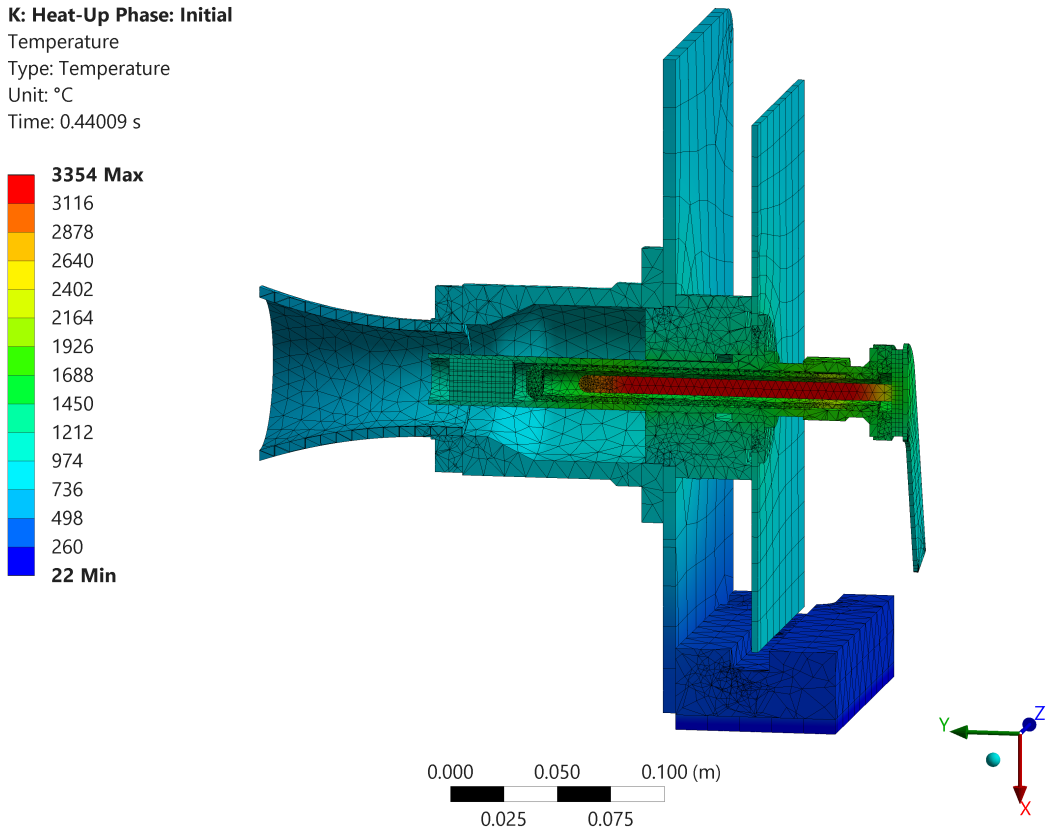

Figure 3.28: Temperature distribution results of the initial heat-up phase simulation across a cross-section of the thruster.

vaporiser temperature profile was attained during the initial simulation, it was of particular importance that this refined simulation achieved the same.

3.5.1 Boundary Conditions

The boundary conditions of the refined heat-up simulation were different to the initial simulation only for the heat flux of the heater. As mentioned earlier, the area heat flux was altered to a volumetric heat flux. A volumetric heat flux of 3.47×10^9 W m^{-3} was selected, equivalent to the 22.6 kW heater power from Section 3.4. The volume of the heater rod is 6.51×10^{-6} m^3, taken from the CAD file. Finally, the cooling condition was maintained at 22 °C on the bottom surface of the MACOR® plate.

3.5.2 Results

This refined simulation returned results largely similar to that of the initial simulation, which is expected since the total thermal input is the same despite the difference in area and volumetric heat flux. The temperature profile is presented in Figures 3.29 and 3.30.

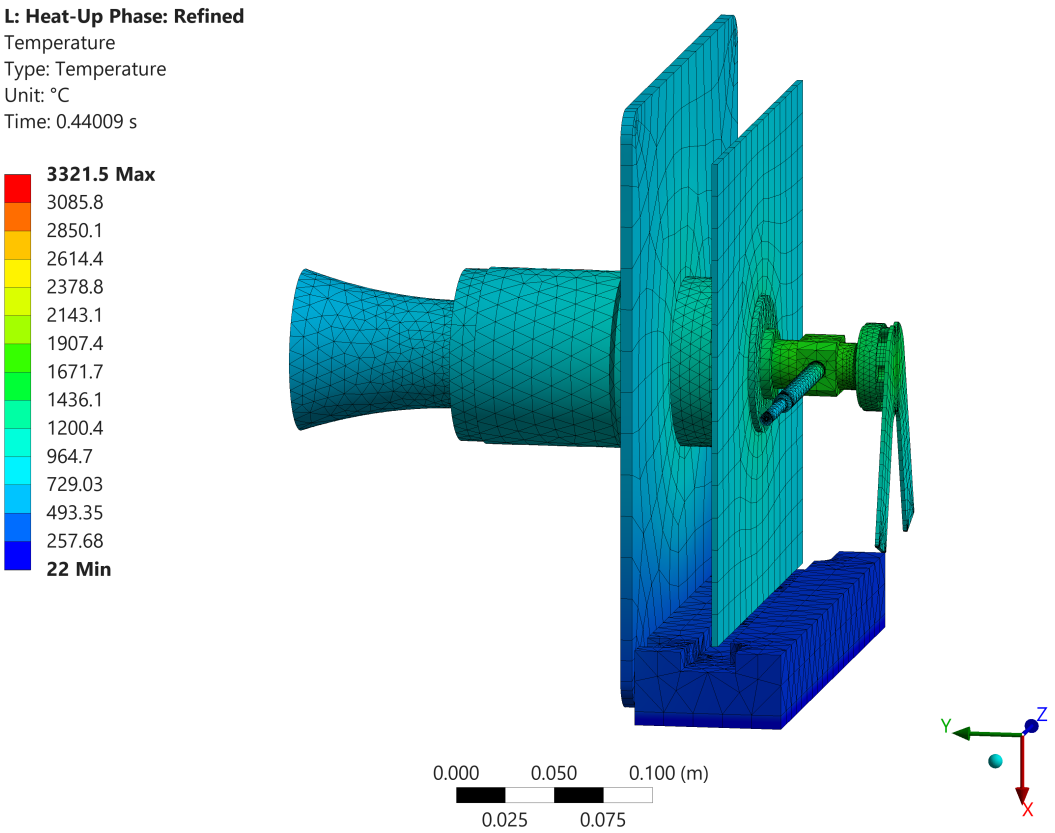

Figure 3.29: Temperature distribution results of the refined heat-up phase simulation over the whole thruster.

At first glance, the temperature distributions of the initial simulation (Fig. 3.27 & 3.28) and the final simulation (Fig. 3.29 & 3.30) were almost identical. The maximum temperature of both simulations only varied by 32.5 °C on a scale of up to 3627 K, a 0.90 % difference. Upon closer examination, the thin-thick feed pipe transition was at 755 °C and the tang ends were at 907 °C. The top left corner of the cathode plate and anode plate are 770 °C and 720 °C, respectively. The anode tip was at 644 °C, with the multi-channel cathode tip at 1208 °C. The temperature range of the vaporiser is 1433 °C to 1864 °C, and the heater is 2907 °C at the tip of the rod to 3200 °C in the middle. These ranges are comparable to the initial heat-up simulation, and the

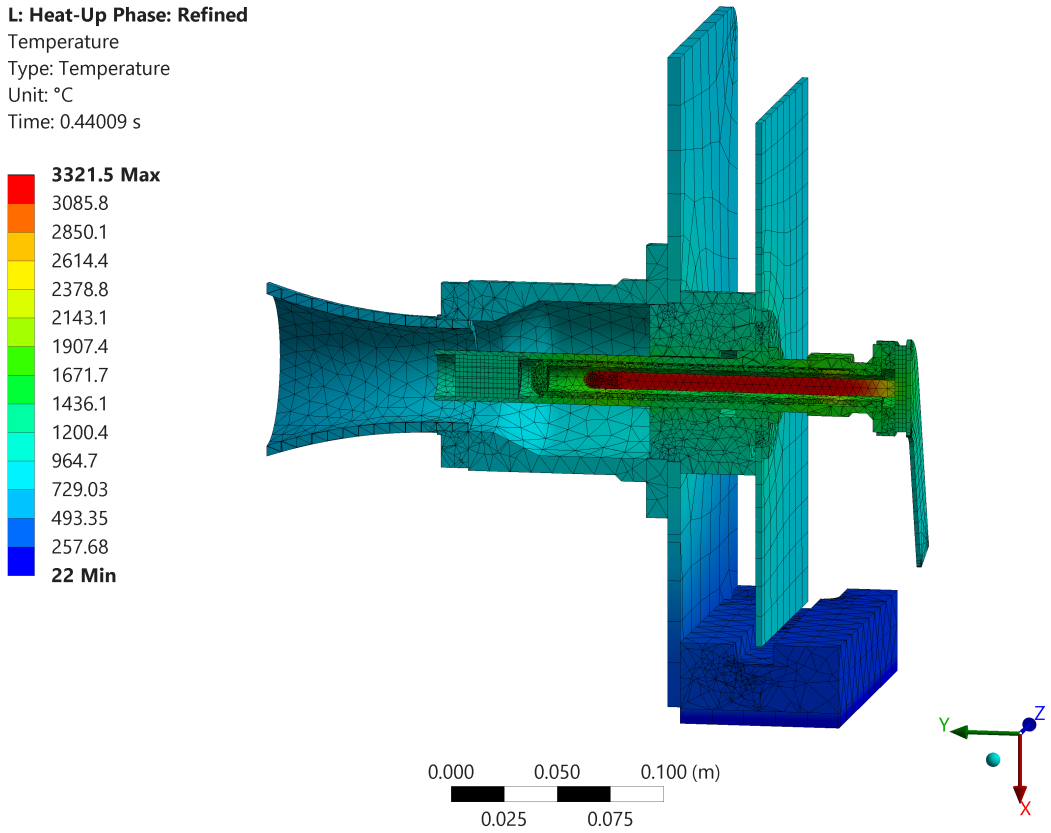

Figure 3.30: Temperature distribution results of the refined heat-up phase simulation across a cross-section of the thruster.

largest difference is 205 K at the tip of the cathode.

It appears that volumetric heat flux gives a slightly more even temperature distribution over the heater rod itself but the effect does not propagate to the rest of the thruster. In fact, the temperature profiles over the rest of the thruster were strongly similar. This quantitative comparison is presented in Table 3.1. With the results of this refined investigation, it was possible to perform some experimental validation of the ANSYS model.

3.6 Heat-Up Phase: Experimental Validation

With a well-refined model of the heat-up phase formed, an experiment was set up to empirically verify the thermal simulation. The LiLFA thruster was installed in the tank, which was pumped down using the roughing pump and the roots blower. The diffusion pump was not used.

Table 3.1: Comparison between initial and refined simulations of the heat-up phase.

Location	**Initial (°C)**	**Refined (°C)**
Feed pipe (thin-thick neck)	766	755
Tang (end)	1011	907
Cathode plate (top left)	780	770
Anode plate (top left)	726	720
Anode tip	645	644
Multi-channel cathode tip	1171	1208
Vaporiser	1430-1800	1433-1864
Heater	2704-3230	2907-3200

3.6.1 Thermocouple Diagnostics

The method of verification was to obtain the steady-state temperature at various points across the thruster. Specifically, four Type K thermocouples were placed: one on the lithium feed pipe, one on the top left corner of the cathode plate, one on the top left corner of the anode plate and one by the base of the thruster. The positions of each thermocouple are visualised in Figures 3.31 and 3.32. The thermocouple on the feed pipe was directly clamped onto the pipe itself, whilst those on the cathode and anode plates were wrapped around a $\frac{3}{8}$" bolt secured with a nut and washer. The fourth thermocouple at the base of the thruster was weighted down by a thick molybdenum block, with the bottom surface covered in thermally resistant Kapton® tape.

These placements were chosen due to their reasonably low temperature profiles from the simulation results. Thermocouples are inevitably limited by their melting points, and the Type K thermocouple has a maximum operating range of 1260 °C [27]. Therefore, a cautious effort was made to balance the temperature between scientific interest and practicality.

3.6.2 Experimental Procedure

Before heating up the thruster, the vacuum tank was pumped down using the roughing pump and the roots blower, in that order. The roughing pump brought the pressure down to approximately 2 Torr, after which the roots blower was turned on to lower it further to around 10^{-1} Torr. For thruster firing, the diffusion pump would then be switched on to achieve a final starting pressure in the region of 10^{-5} Torr. Once the thruster firing begins, this pressure can rise up to 10^{-4} Torr. However, the entire

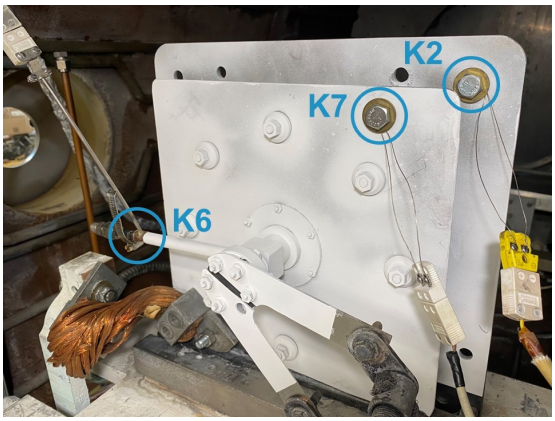

Figure 3.31: Respective placements of three Type K thermocouples. The K2 connection is on the anode plate, K7 on the cathode plate and K6 on the propellant feed pipe.

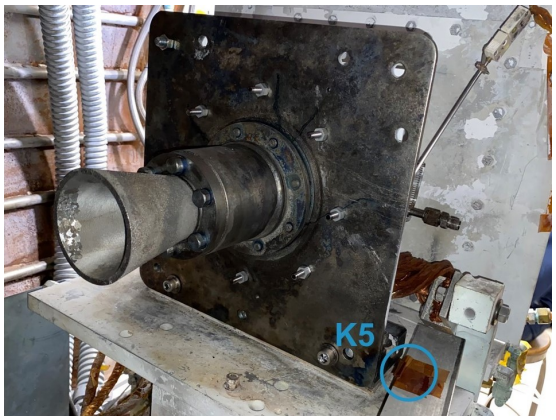

Figure 3.32: Position of the fourth Type K thermocouple, connected to the K5 port and placed at the base just next to the MACOR® plate.

vacuuming process until the completion of the diffusion pumping can take several days. Given the limited timeline of the remainder of the project, the 10^{-1} Torr attained using the roots blower was deemed sufficient to run experiments of the heat-up phase.

Whilst 10^{-1} Torr is four orders of magnitude smaller than the atmospheric pressure of 760 Torr, it is also three orders of magnitude larger than the nominal thruster firing pressure of 10^{-4} Torr. As such, it is important to investigate the validity of negating convection in this environment.

The mean free path, λ, is defined as the average distance travelled by a gas particle between consecutive collisions. It is expressed as

$$\lambda = \frac{k_B T}{4\pi\sqrt{2} r^2 P}, \tag{3.6.1}$$

where $k_B = 1.3806\,\mathrm{J\,K^{-1}}$ is the Boltzmann constant, T is temperature, r is molecular radius and P is pressure. Furthermore, the Knudsen number, K_n, is the normalisation of this mean free path by a length scale, L:

$$K_n \equiv \frac{\lambda}{L}. \tag{3.6.2}$$

The dimensionless Knudsen number is one method of determining the mode of heat

transfer in an environment. The vacuum environment of space, which correlates to the free molecular regime, is represented by a Knudsen number of over 0.3 [28].

As the dominant component of air, nitrogen will be taken as the molecule in question. The Van der Waals radius of N_2 is 332 pm [29]. The ambient temperature of the vacuum tank is 22 °C, and the length scale can be estimated conservatively using the largest separation between thruster components as 10 cm. Using Equations 3.6.1 and 3.6.2, the Knudsen number at the roots blower pressure of 10^{-1} Torr can be calculated as 0.00156. Whilst this calculation was performed using conservative values, it is an indication that there must be consideration for non-zero convection when analysing results from this experiment. It should be noted that, at the thruster firing pressure of 10^{-4} Torr, the Knudsen number is well above 0.3 at 1.56. Therefore, there is confidence that nominal thruster firing occurs in the free molecular regime.

With the vacuum tank down to a stable pressure of approximately 10^{-1} Torr, the cooling valves were opened. The heater was then turned on at a constant current of 70 A. With the power supply displaying a voltage of 8.5 V, there was an upper bound of 595 W internal heat generation at the heater. This was the power used for the equivalent ANSYS simulation.

3.6.3 Experimental Results

Temperatures at the four thermocouple locations were collected and plotted over time, shown in Figure 3.33. Data collection was started before the heat-up phase at initial thermal equilibrium, and it was stopped after the final thermal equilibrium was established.

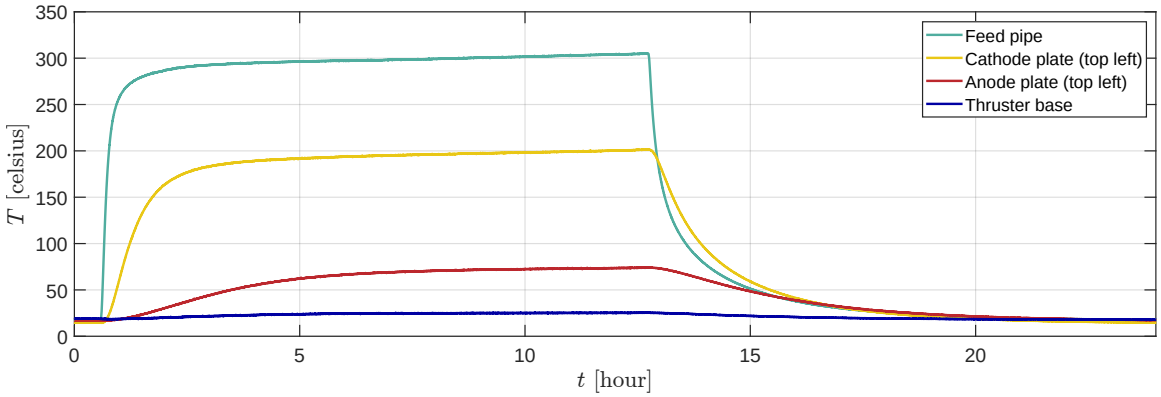

Figure 3.33: Experimental temperature over time at four thermocouple locations during the heat-up phase.

It is clear that the feed pipe reaches the highest temperature at 305.1 °C, followed

by the cathode plate at 201.4 °C, the anode plate at 74.5 °C and the thruster base at 25.9 °C. The same order is followed with regard to the rate of response to the heater powering, which is consistent with the time taken for thermal information to travel from the heater to the respective components. The feed pipe is closest to the heater, followed by the cathode plate and finally the anode plate. Due to active cooling, the thruster base remains close to the EPPDyL room temperature of 22 °C, although there is a slight increase of 3.9 °C. The temperature curves are still gradually rising when the heater is turned off, indicating that steady-state equilibrium was nearly but not fully achieved. However, the heater had to be turned off after just over 12 hours to conclude the experiment within practical time contraints of the experimental setup.

These experimental results were compared to the refined heat-up phase simulation rerun with the equivalent power input of 595 W. In general, the experiment returned higher temperatures than the simulation, except for at the top left corner of the anode plate. A quantitative comparison is document in Table 3.2, along with disagreement calculations, and these results will be discussed in Section 3.8.

Table 3.2: Comparison of absolute temperature during the heat-up phase between experiment and simulation.

Location	**Experiment (K)**	**Simulation (K)**	**Disagreement (%)**
MACOR® base	299.0	295.2	-1.3
Feed pipe	578.3	476.2	-17.7
Cathode plate	474.6	440.2	-7.2
Anode plate	347.6	415.4	+19.5

The cooling curve is consistent with the heating curve in terms of the heat transfer rate. It appears to have taken approximately 12 hours to reach thermal equilibrium at room temperature. Whilst this time-dependency cannot be compared to the steady-state simulations, transient thermal modelling is certainly a possibility in the future.

3.7 Thruster Firing: Initial Simulation

The firing of the thruster takes place after, and in addition, to the heat-up process. It is substantially more complex to model than the heat-up process, as there is propellant flow, propellant vaporisation, thermionic emission and potential between the anode and cathode, just to name a few key additions.

3.7.1 Boundary Conditions

Thruster firing involves several key thermal boundary conditions in addition to those already in place for the heater. These additional boundary conditions are at the anode and the cathode, and capture the thermal effects of the plasma. These boundary conditions are also those implemented by the EP team at NASA-JPL, recreated for the EPPDyL LiLFA thruster through discussion with Principal Engineer Dr. Jay Polk.

With regard to the anode, there are three possible options for the boundary condition. All options are applied to the inner surface of the anode and amount to a heat flux of 12 kW, which is 40 % of the total thruster power of 30 kW:

1. A uniform heat flux.
2. A linearly increasing heat flux from zero at the upstream end and maximum at the downstream end.
3. A uniform but concentrated heat flux in the downstream half.

For this simulation, a uniform heat flux was implemented.

The boundary condition at the cathode is more complicated. Whilst it is simply the clamping of a constant temperature over electron emitting surfaces at the tip of the cathode, this temperature is a function of current density and work function. This calculation is performed using the Richardson-Dushman equation for thermionic emission:

$$J = AT^2 e^{-\frac{\phi}{k_B T}}. \tag{3.7.1}$$

J is current density and $k_B = 1.3806\,\mathrm{J\,K^{-1}}$ is the Boltzmann constant. ϕ and A are work function and the Richardson constant, respectively, both unique to a given material. The work function of tungsten is well documented at 4.52 eV [20]. The physical meaning of work function is the minimum energy required for an electron to escape from a crystalline solid surface [20]. The Richardson constant of pure tungsten is $60.2 \times 10^4\ \mathrm{A\,m^{-2}\,K^{-2}}$ [20].

The current density is a more complex value to parameterise as it is a function of the surface area of emission. In this problem, the emitting surface area is taken to be the total area through the multi-channel cathode rods (Fig. 3.34). Whilst several approaches were considered for this calculation, such as implementing theories from the circle packing problem, a simpler, and arguably more accurate, solution was implemented. From Figure 3.34, it was first determined that the outermost

rod arrangement of diameter D had space for 26.5 individual rods of diameters d. Furthermore, the outermost width of the channel was obtained as 20 mm. Therefore,

$$\frac{\pi D}{d} = 26.5, \tag{3.7.2}$$

$$D = 20\,\text{mm} - d. \tag{3.7.3}$$

Upon solving the simultaneous equations (Eqn. 3.7.2 & 3.7.3), the rod diameter was evaluated as 2.12 mm on average. From Figure 3.34, the total number of rods in the multi-rod channel was also determined as 72. By combining the rod diameter and the total number of rods with the length of the rods, 30 mm, it was possible to calculate the total area by

$$\text{Area} = 72 \cdot \pi d \cdot 30\,\text{mm} = 1.44 \times 10^{-2}\text{m}^2. \tag{3.7.4}$$

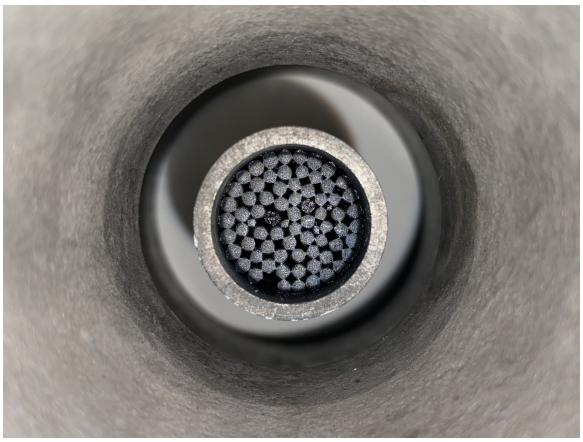

Figure 3.34: Parallel view into the multi-channel tungsten rods at the cathode tip.

All obtained parameters were then combined to solve the Richardson-Dushman equation (Eqn. 3.7.1) over a range of currents. This current range was set from 50 A to 900 A, as the maximum range over which experimental data was collected for the applied-field version of the same EPPDyL LiLFA by Lev [30]. A MATLAB script was written to calculate and graph the current-dependent thermionic emission temperature of the thruster and the plot is shown in Figure 3.35. Ultimately, the highest temperature of 2600 °C was clamped at the multi-channel cathode tip, corresponding to a current of approximately 900 A.

These boundary conditions also possess some limitations. In particular, it neglects the fact that the passing lithium propellant absorbs most of the heat from the heater at the vaporiser. The team at NASA-JPL hired external specialists to capture this

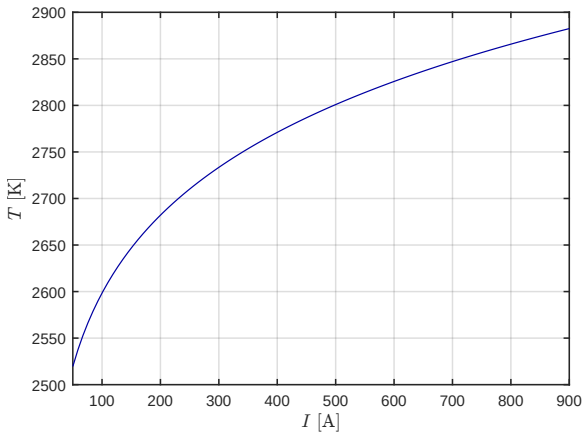

Figure 3.35: Thermionic emission temperature of the LiLFA from 50 A to 900 A.

effect that is beyond the scope of this thesis. Alternatively, it is possible to model this phenomenon more simply by taking the product of lithium latent heat and mass flow rate as the power absorbed when the lithium reaches vaporisation temperature. In this study, however, this effect will be neglected and the worst-scenario will be explored to determine the upper bound of the thermal model with zero lithium heat absorption.

3.7.2 Results

Compared to the heat-up phase, the temperatures of this thruster firing simulation were largely similar on the back of the thruster, with higher temperatures exhibited at the front. This is expected since the heater settings remained the same, whilst heating due to plasma was superimposed. The temperature distribution over the thruster is presented in Figures 3.36 and 3.37.

The thin-thick transition of the feed pipe was recorded at 751 °C and the tang ends were at 899 °C. The top left section of the cathode plate was at 774 °C and the corresponding segment of the anode plate was at 751 °C. This anode plate temperature was 31 °C higher than during the heat-up phase. The anode tip was at 1497 °C, which is significantly higher than that of the heat-up phase, and the multi-channel cathode tip was surprisingly lower at 1157 °C. Whilst the cathode tip temperature should not be lower during thruster firing compared to the heat-up phase, it is also concerning as a boundary condition was placed to clamp the temperature at 2600 °C. This must be investigated in the future and will be discussed in greater detail later in Section 3.8.

Finally, the temperature profile over the vaporiser was 1408 °C at the tip to 1806 °C

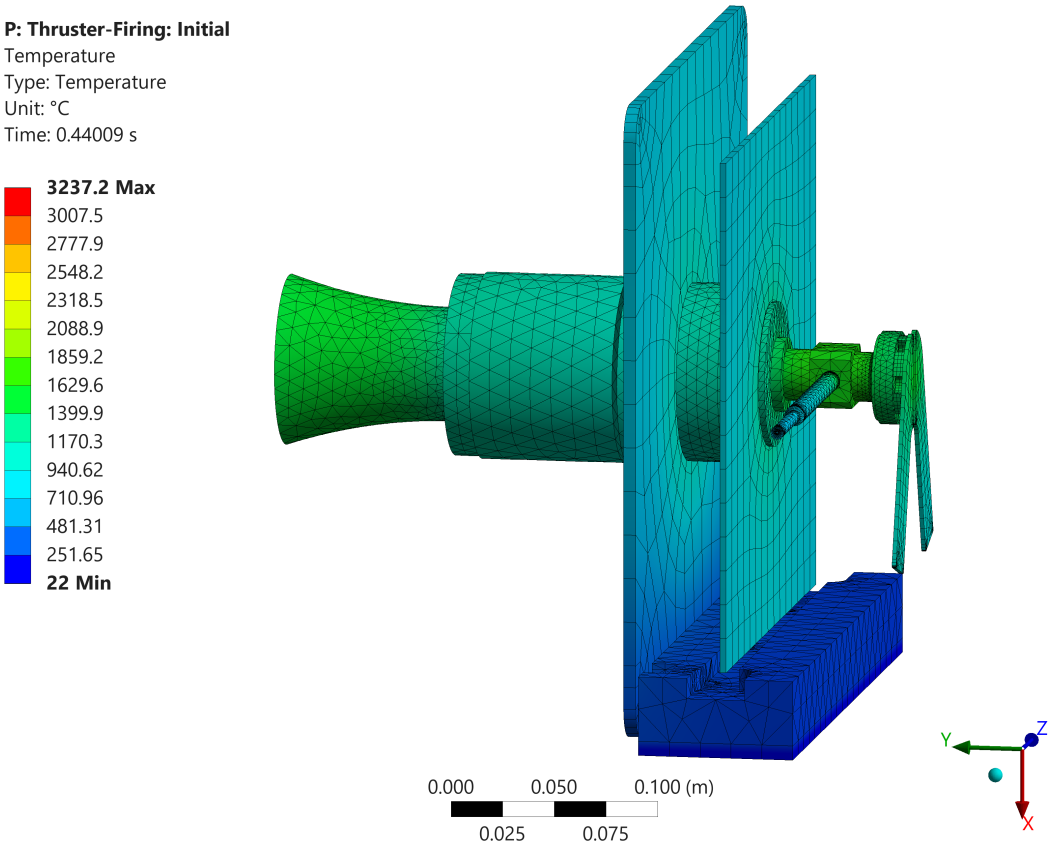

Figure 3.36: Temperature distribution results of the thruster firing simulation over the whole thruster.

in the middle. For the heater, it was 2847 °C at the tip to 3126 °C in the middle. Both distributions are similar to those during the heat-up phase, albeit slightly cooler. This quantitative comparison is summarised in Table 3.3.

3.8 Discussion

This investigation of the thermal behaviour of the LiLFA yielded valuable results, significantly improving on limited previous understanding.

The preliminary investigation returned results in broad agreement with those of Emsellem et al. [8], which justified confidence in the general performance of the ANSYS thermal setup. Due to unfeasible computation times, the thruster geometry was simplified with the removal of small parts such as nuts, bolts, rods and washers. This likely reduced the fidelity of the simulations.

The heat-up phase was then modelled through an initial simulation and a re-

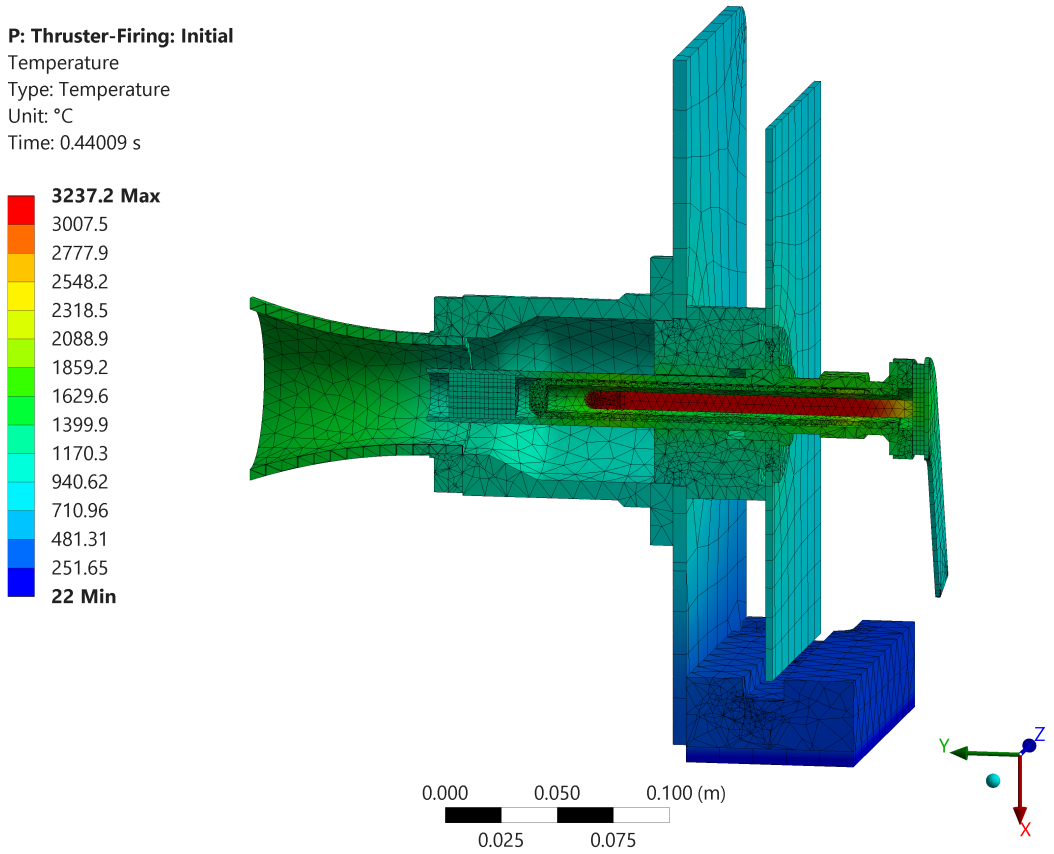

Figure 3.37: Temperature distribution results of the thruster firing simulation across a cross-section of the thruster.

fined simulation, which laid the foundations for an experimental verification of the numerical analysis. The heater was powered at 595 W, and subsequently compared to an equivalent ANSYS simulation. The comparison showed reasonable differences between the two results, with the magnitude of disagreement ranging from 1.3 % to 19.5 % across four thermocouple locations.

There are likely many reasons for this discrepancy. As mentioned earlier, the thruster geometry was simplified. Perhaps, the molybdenum rods were a significant contributor the thermal dissipation through the thruster. Furthermore, the contacts between surfaces may have been different between the experiment and simulations. For instance, two surfaces in perfect contact within the CAD model may in fact be marginally separated in actuality, severely affecting the heat transfer. A simpler factor may be that the thruster hadn't completely reached steady-state yet, although this reasoning would only be valid for the anode plate where the temperature was lower in simulation than from empirical data. It was noticed, however, that the voltage of the heater was gradually yet constantly rising throughout the heat-up phase. This is

Table 3.3: Comparison between the refined heat-up and initial thruster firing simulations.

Location	**Heat-up (°C)**	**Thruster firing (°C)**
Feed pipe (thin-thick neck)	755	751
Tang (end)	907	899
Cathode plate (top left)	770	774
Anode plate (top left)	720	751
Anode tip	644	1496
Multi-channel cathode tip	1208	1157
Vaporiser	1433-1864	1408-1806
Heater	2907-3200	2847-3126

understandable as the resistance, and therefore heat generation, of the heater circuit rises with temperature. Such an effect was not reflected in the simulation. Also, the negation of conduction may not have been entirely valid, as discussed in Section 3.6.2. However, this contribution should have increased convective cooling of the thruster, which is inconsistent with three of four thermocouple data. Similarly, the back surfaces of the thruster were coated with boron nitride powder to prevent arcing during thruster firing. Whilst this was not considered in the thermal simulations, it must have led to an increased cooling effect with the substantially higher emissivity of boron nitride compared to molybdenum.

It is important to analyse each thermocouple location in more detail. The discrepancy at the MACOR® base plate can be explained simply. It is clear that the cooling power was insufficient to maintain the base at room temperature, and thus a slightly higher equilibrium was achieved. As for the feed pipe, one theory is that the insulator between the heater back plate and the rest of the thruster was not made of boron nitride. A possible alternative is aluminium nitride, which would be suitable for direct contact with the heater due to its low thermal expansion. As the thermal conductivity of aluminium nitride is approximately four times larger than that of boron nitride [31], this would have resulted in substantially more thermal conduction towards the feed pipe, justifying its higher experimental temperature. Similarly. this effect would have propagated to the cathode plate, but not as much to the anode plate. Another explanation that would have the same effect is that there was substantial heating from the heater back plate, which was not reflected in the simulation. This is likely as the heater back plate was visibly glowing during the heat-up phase.

These two sources of unaccounted conductive heating from the back of the heater towards the rest of the thruster are consistent with the higher experimental tempera-

tures at the feed pipe and the cathode plate. On the other hand, the anode plate was cooler during the experiment compared to the simulation. This may be that extra cooling due to the boron nitride coating and incorrectly negated conductive effects outweighed the unaccounted heating, as the anode plate is further away from the thermal source than its counterparts.

This study concluded with an exploration of the LiLFA thermal behaviour during thruster firing. Boundary conditions were implemented to model the thermal effects of plasma, and the results showed greater heating towards the front of the thruster, particular on the anode nozzle, anode plate and cathode plate. Whilst there is insufficient justification to propose any cost-reducing material changes, there is confidence to suggest the use of Type C thermocouples directly on the outer surface of the anode during thruster firing to obtain accurate temperature measurements beyond numerical simulations. The Type C thermocouple is rated up to 2320 °C [32]. This will subsequently allow for further refinement of the ANSYS thermal model, resulting in higher fidelity understanding of the thruster's thermal behaviour.

Chapter 4

PID Pressure Control of Lithium Handling Glovebox

4.1 Experimental Design

To prevent the hazardous reaction of lithium and water, air must never enter the argon-filled lithium handling glovebox. Therefore, the pressure of argon in the glovebox must be maintained higher than the atmospheric pressure to avoid inward air leakage. Previously, a second operator was required, in addition to the primary glovebox operator, to monitor the pressure gauge, ensure a positive argon pressure and act promptly in response to any issues. However, this is labour intensive, and there is a significant safety concern in the form of human error.

4.1.1 PID Control System

A PID control system was devised to maintain a constant slight positive gauge pressure of argon within the glovebox. Three requirements were outlined:

1. Pressurise the glovebox with argon from vacuum to slightly above 1 atm.
2. Maintain the slight positive argon gauge pressure.
3. Allow for manual override of the system in case of technical malfunctions.

The high level design involved a pressure transducer to obtain pressure information, an Arduino to perform PID calculations and a motor-controlled rotational valve to adjust the argon flow into the glovebox.

The choice of a motor-valve system was made due to the costly price of conventional mass flow controllers. On the current market, mass flow controllers compatible for this application cost at least $1,000, often several factors larger [27]. However, the motor-valve system posed several design constraints, largely deriving from the mechanical limitations of a one-way rotational valve:

1. The motor could not vent argon—it could only control zero to positive flow towards the glovebox.

2. Fine adjustments were required.

3. Reliable closing of the valve was required.

4. The motor required the ability to detect zeroing out.

To address these constraints, it was decided that a sufficiently torque-rated motor with encoder was the optimal solution.

Considering all of the above design objectives and requirements, a system layout was created (Fig. 4.1). The glovebox is central to the system, in which a slight positive gauge pressure of argon must be maintained. A pressure transducer quantitatively obtains the pressure of the chamber, and the information is relayed to an Arduino. The Arduino processes the data through a PID code, obtaining instructions that are then communicated to the mechanically integrated motor-valve system. This is labelled as the mass flow controller (MFC) in Figure 4.1. Whilst the MFC will be the primary form of argon flow control, there is also a physical valve in parallel to allow for manual override of the system. The two connect back to the glovebox together.

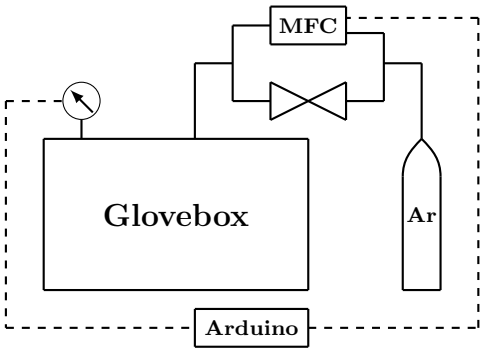

Figure 4.1: Block diagram of the system setup. “MFC” stands for “mass flow controller” and “Ar” refers to “argon”. Solid lines represent physical pipe connections, whilst dashed lines represent digital connections.

Derivation

With a block diagram of the system setup in place, the control system theory was derived. The state, x, was set to the tank pressure, P, as the variable to be maintained at a set point. The input, u, was set to the motor encoder position, θ, as the parameter directly proportional to the argon mass flow rate. Finally, the output, y, was also set to the tank pressure, P.

The derivation starts with the Ideal Gas Law, where P is the pressure, V is the volume, n is the number of moles of gas and R is the ideal gas constant:

$$PV = nRT, \tag{4.1.1}$$

$$P = \frac{nRT}{V}. \tag{4.1.2}$$

Since $n(t) = \frac{m(t)}{M_r}$, where $m(t)$ is the mass as a function of time and M_r is the molecular weight,

$$P(t) = \frac{RT}{VM_r} m(t) = k_1 m(t), \tag{4.1.3}$$

where k_1 is taken as $\frac{RT}{VM_r}$. By taking the time derivative of Equation 4.1.3, it is possible to obtain

$$\dot{P}(t) = k_1 \dot{m}(t) = k_1 \dot{m}_{in} - k_1 \dot{m}_{out}, \tag{4.1.4}$$

$$= k_1 k_2 \theta, \tag{4.1.5}$$

where $\dot{m}_{in} = k_2\theta$. Physically, this means the argon mass flow rate into the glovebox, $\dot{m}_{in}$, is proportional to the valve angle, θ. It should also be noted that the argon mass flow rate out of the glovebox into the atmosphere, $\dot{m}_{out}$, is close to zero. Now, it is possible to obtain the full linear dynamical system, represented by two sets of equations:

$$\dot{x} = Ax + Bu, \tag{4.1.6}$$

$$\dot{P} = 0P + k_1 k_2 \theta. \tag{4.1.7}$$

$$y = Cx + Du, \tag{4.1.8}$$

$$P = 1P + 0\theta. \tag{4.1.9}$$

Through this, the constants are determined as $A = 0$, $B = k_1 k_2$, $C = 1$ and $D = 0$.

Furthermore, the controllability matrix is $P = B = k_1 k_2$ which is full rank, and the observability matrix is $Q = C = 1$ which is also full rank. The control system is therefore both controllable and observable. Finally, the transfer function of the system can be evaluated as

$$G(s) = C(sI - A)^{-1}B + D = \frac{k_1 k_2}{s}. \tag{4.1.10}$$

This PID control system can be visualised through a block diagram, as shown in Figure 4.2. $r(t)$ is the set point, in this case the desired pressure of the glovebox. $e(t)$ is the error, in this case the difference between the actual and desired pressures of the glovebox. $u(t)$ is the input, in this case the valve angle, θ. $y(t)$ is the output, in this case the actual pressure of the glovebox.

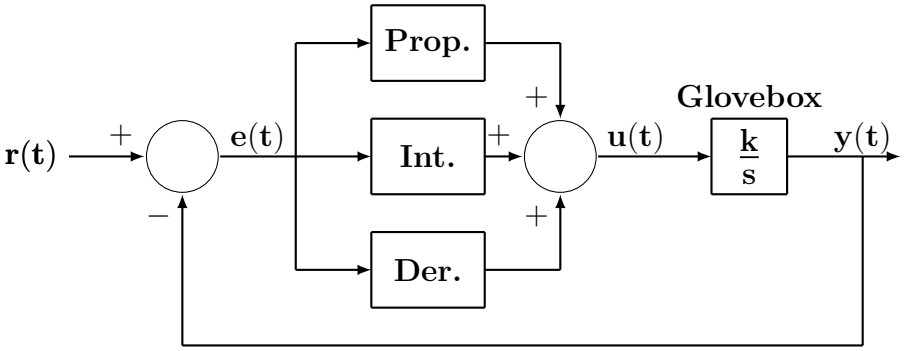

Figure 4.2: Block diagram of the PID control system.

4.1.2 Design Setup

The setup is based on the configuration presented in Figure 4.1. The pressure state is obtained by a SMC ZSE20AF pressure transducer (Fig. 4.3), which has a digital monitor to display the real-time pressure. This is critical in the event the control system malfunctions, as it allows the operator to visually ensure the pressure remains within safe margins and manually override the system if necessary. The rest of this setup can be categorised into mechanics, electronics and software. Mechanics include the mechanically integrated motor-valve system and the piping between the argon cylinder and the glovebox, whilst electronics are the wiring and circuitry of the Arduino. Additionally, there is a software aspect in the form of Arduino code.

Figure 4.3: Image of the SMC ZSE20AF pressure transducer. From SMC Corporation (2024) [33].

Motor-Valve Mechanical Integration

The mechanically integrated motor-valve system allows for precise control of argon flow from the cylinder to the glovebox without the use of an expensive mass flow controller. Specifically, this was achieved by attaching a motor with an encoder to a rotational valve. The motor implemented in this project is the BEMONOC 12 V DC Motor with Encoder (Fig. 4.4), and the valve in use is the Swagelok SS-3NTRS4 Union Bonnet Needle Valve (Fig. 4.5).

Figure 4.4: Photo of the BEMONOC 12 V DC Motor with Encoder. From BEMONOC (2024) [34].

Figure 4.5: Photo of the Swagelok SS-3NTRS4 Union Bonnet Needle Valve. From Swagelok (2024) [35].

To mechanically integrate the motor and the valve, a coupler was required to connect the motor shaft to the valve shaft, as well as a torque fixture to prevent free rotation of the combined fixture. The torque fixture was designed, with the CAD software Creo Parametric, as a two-piece system fastened by nuts and bolts. The design is shown in Figure 4.6.

With regard to the coupler, a 3D printed component was initially designed (Fig.

4.7). The design made use of the D-profile shaft on the motor and the handle of the valve. To allow for rapid iteration, the coupler was first printed with polylactic acid (PLA), with the intention to perform the final print with nylon for increased printing precision and durability.

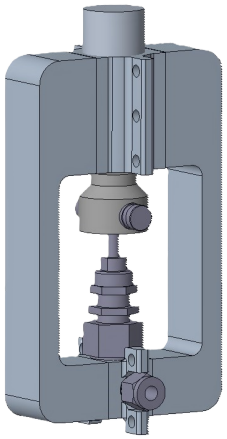

Figure 4.6: Initial CAD design of the whole motor-valve system.

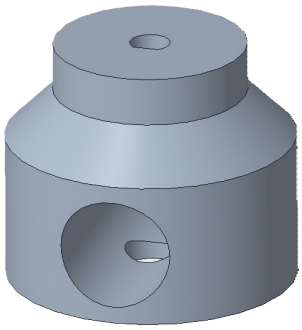

Figure 4.7: Zoomed-in CAD design of the motor-valve coupler.

However, due to an unexpectedly fast rate of erosion of the PLA coupler's D-profile, the decision was made to machine a new, robust coupler out of aluminium. The intuition of the new coupler was such that, rather than utilising the D-profile shaft, two metallic rings would tightly grip the motor and valve shafts by tightening a small gap with a screw. Two rods, one press fit into the top ring and the other placed loosely through the bottom ring, would ensure rotational coupling whilst allowing for vertical sliding of the valve shaft. This new coupler was designed (Fig. 4.8-4.10) and machined from scratch. The result is an extremely durable coupler that will certainly last as long as the system operates.

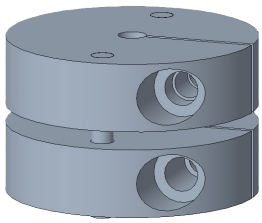

Figure 4.8: CAD model of aluminium coupler.

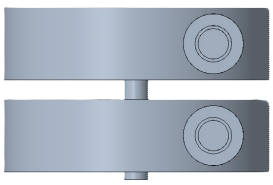

Figure 4.9: Side view of aluminium coupler.

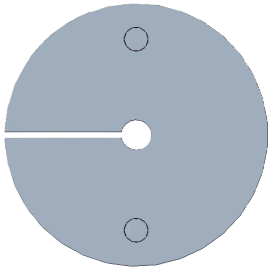

Figure 4.10: Top view of aluminium coupler.

Piping

To ensure a robust connection from the argon cylinder to the glovebox whilst allowing for parallel manual override as shown in Figure 4.1, the preexisting piping prior to the development of the PID system were disassembled and new piping connections were installed.

For materials, $\frac{1}{4}$" copper tubing and brass Yor-Lok fitting were used as an optimal balance between reliable gas sealing and cost. A manual tube bender was used to form the perpendicular turns to allow for parallel piping. Whilst new components were implemented directly, old components being reused from the laboratory were first scrubbed, internally and externally, with a wire brush, after which they were soaked in a warm mixture of vinegar, dish detergent and water for 24 hours to react with oxides and remove debris. Furthermore, the ends of all cut copper tubing were filed and chamfered. All of this was the ensure reliable seals at each connection. Additionally, thread seal tape was applied to all male adapters before connection. The final piping system is shown in Figure 4.11, as well as in Figure 4.12 where it is installed between the argon cylinder and the glovebox.

Figure 4.11: Parallel piping system without the motor integrated with the valve.

Figure 4.12: Parallel piping system installed between the argon cylinder and the glovebox.

4.1.3 Electronics and Circuitry

The initial design of the electronics was such that all components were, either directly or indirectly, powered by the ALITOVE 12 V power supply. These components include the Arduino and its motor shield (Fig. 4.13), the motor and its encoder and the pressure transducer. This layout of the power supply and the Arduino is visualised in Figure 4.14.

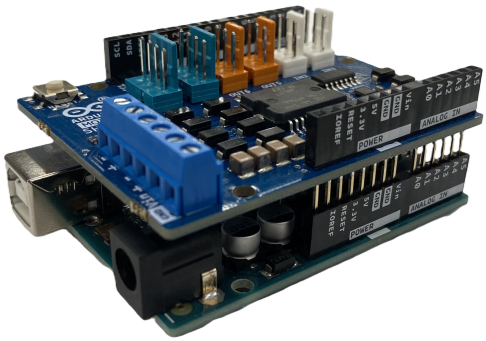

Figure 4.13: Image of the Arduino and its motor shield stacked vertically.

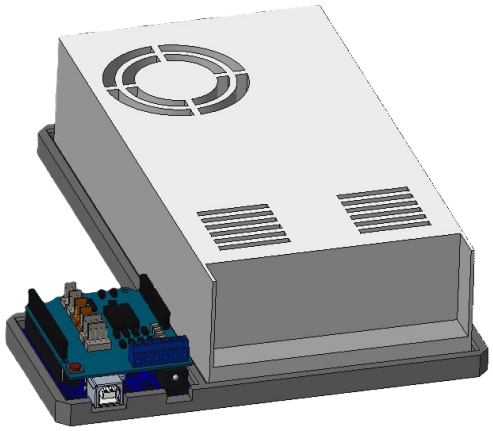

Figure 4.14: Layout of the 12 V power supply and the Arduino with its motor shield stacked vertically.

With regard to the circuitry, components were directly connected to the power supply where possible. The exception was the motor, which was required to be powered by the Arduino motor shield to achieve directional and pulse width modulation (PWM) control of the rotational velocity, depending on the output of the PID code within the Arduino. Furthermore, the motor's encoder was connected to the Arduino's 3.3 V internal power supply due to its minimal power requirement.

In terms of data connections, the two encoder branches were connected to Pin 2 and Pin 4 of the Arduino. The analogue signal from the pressure transducer was connected to Pin A5 on the analogue section of the Arduino. The circuitry is displayed in Figure 4.15 and the connections are summarised in Table 4.1.

4.1.4 PID Code

The code for the PID control system was written in Arduino, to process inputs from the pressure transducer and motor encoder and control the speed and direction of the motor depending on the output.

The code was developed around a fundamental Arduino PID loop introduced by The Bored Robot [36]. Specifically, The Bored Robot's code has been utilised to the extent of keeping track of the encoder position and creating a PID function that takes in the current state, pressure P, and returns the subsequent input, valve area θ. The loop operates by determining the time interval and error, then using the value, along with adjusted PID coefficients, to calculate the input. Mathematically, the code can

Table 4.1: List of all connections within the circuitry. DC stands for direct current, ANLG for analogue, ECD for encoder and GND for ground.

Component	**Connection**
12 V DC^+	Arduino Motor Shield V_{IN}
12 V DC^-	Arduino Motor Shield GND
Pressure Transducer V^+	12 V DC^+
Pressure Transducer V^-	12 V DC^-
Pressure Transducer $ANLG_{OUT}$	Arduino Motor Shield Pin A5
$Motor^+$	Arduino Motor Shield A^+
$Motor^-$	Arduino Motor Shield A^-
Motor ECD^+	Arduino Motor Shield 3.3 V
Motor ECD^-	Arduino Motor Shield GND
Motor ECD_1	Arduino Motor Shield Pin 2
Motor ECD_2	Arduino Motor Shield Pin 4

be depicted as follows:

$$dt = t_i - t_{i-1}, \tag{4.1.11}$$

$$e_i = P_i - P_{i-1}, \tag{4.1.12}$$

$$e_i^{der} = \frac{e_i - e_{i-1}}{dt}, \tag{4.1.13}$$

$$e_i^{int} = e_{i-1}^{int} + e_i dt, \tag{4.1.14}$$

$$u_i = K_P \cdot e_i + K_D \cdot e_i^{der} + K_I \cdot e_i^{int}. \tag{4.1.15}$$

Since the loop is performed at incrementally short time intervals, a numerical approach is sufficient. This PID loop, inspired by The Bored Robot [36], is labelled amongst the rest of the code in Listing C.1.

The overall code begins with a calibration of the motor to identify the encoder position when the valve is closed. Specifically, the motor turns the valve clockwise until no movement is detected, at which point the encoder count is reset and calibrated as the zero position. After waiting five seconds, the rest of the code is resumed. The next stage of the code is where the current pressure is obtained. This is performed by reading the analogue signal from the pressure transducer at the Arduino's Pin A5, which is then used to calculate the voltage at the pin. The voltage is subsequently used to deduce the pressure reading that it correlates to.

The details of this process are as follows. The Arduino contains a 10-bit analogue-to-digital converter (ADC), which results in the mapping of input voltages, ranging from zero to a reference voltage, into integer values between 0 and 1023 [37]. The

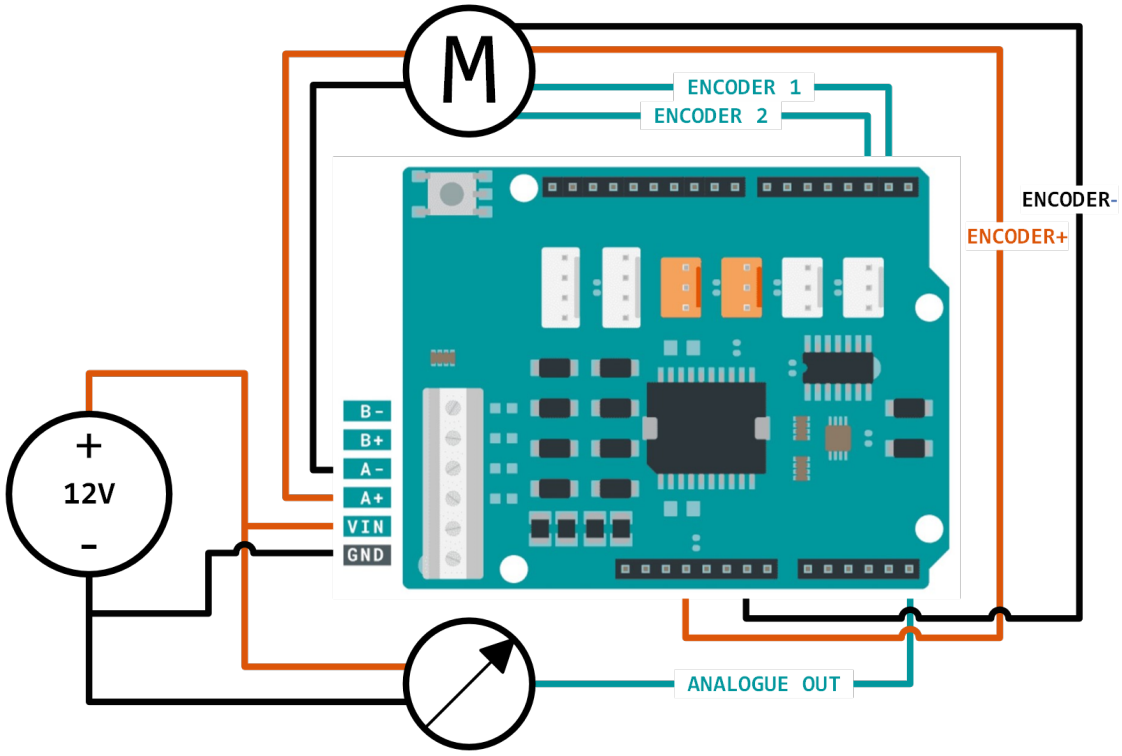

Figure 4.15: Circuitry of the setup, centred about the Arduino and its vertically stacked motor shield.

reference voltage is 5 V by default, but can be set to a custom external reference voltage or the internal reference voltage of approximately 1.1 V [38]. Whilst this calculation may appear fundamental, the Arduino community has historically been divided on the matter. Specifics of this discussion will not be covered in this thesis, but the majority of the debate stems from whether or not to use 1023 or 1024, combined with the fact that the input voltage is inevitably rounded to an integer value. In this project, a well-justified method of calculation by Gammon [39] was implemented.

Once the input voltage is determined, it is possible to obtain the pressure with a voltage-pressure relation outlined in the operation manual of the SMC ZSE20AF pressure transducer [40]. The output voltage of the pressure transducer ranges from 1 V to 5 V, which captures the pressure range of −100 kPa to +100 kPa, where 0 kPa is calibrated to 1 atm [40].

As such, the conversion of the Arduino Pin A5 analogue reading to gauge pressure is performed as follows, where n is the analogue integer between 0 and 1023, V_{ref} the reference voltage of the Arduino, V_{PT} the input voltage from the pressure transducer

and P_{PT} the gauge pressure measured by the pressure transducer:

$$V_{PT} = \frac{n + 0.5}{1024} \cdot V_{ref}, \tag{4.1.16}$$

$$P_{PT} = \frac{V_{PT} - 3}{4} \cdot 2 \times 10^5. \tag{4.1.17}$$

The obtained gauge pressure is then passed through the PID function introduced earlier to calculate the new input into the system. There is a line of code that scales the input variable by the $k_1 k_2$ constant from Equation 4.1.7 to achieve the desired valve area from the valve angle. The code then sets the motor speed and direction to adjust the valve area to the calculated value. This entire process is looped through to maintain a constant gauge pressure of 0.15 psi.

Throughout the code, there are methods in place to cover edge cases and prevent the PID system from behaving uncontrollably. These details are included in the full code, available in Listing C.1.

4.1.5 Troubleshooting

As is the nature of a project of this kind, there were constant obstacles that required troubleshooting. This section will introduce several of the main troubleshooting efforts taken on, by discussing issue identification, solution approach and results.

Arduino Motor Fluctuations

The most significant challenge to this project was the issue of voltage fluctuations during the drawing of current by the motor. Specifically, the problem was such that the internal voltage level of the Arduino and its motor shield would slightly fluctuate whenever the motor was in operation, affecting the pressure transducer reading as the measurement was taken relative to the Arduino's voltage reference. Given the large range of the pressure transducer, from -14.5 psi to $+14.5$ psi, relative to the desired set point of 0.15 psi, this fluctuation led to significant disturbance of the pressure measurement. As a result, the PID controller behaved unpredictably and often uncontrollably.

Several solutions were devised and implemented, some of which were futile and others which contributed to the final solution. Seven of these ideas will be discussed in the following sections.

External Reference Voltage

The first intuition was to investigate the Arduino reference voltage, since the analogue signals are read relative to the reference voltage. Whilst the default Arduino reference voltage of 5 V is typically of sufficient quality, it appeared to be fluctuating and therefore the idea was to find a technique to stabilise it.

The initial plan was to implement a stable external voltage of the same voltage, 5 V. This was achieved with the use of a voltage regulator, specifically the Analog Devices REF02C chip [41] (Fig. 4.16). The circuitry inside the voltage regulator ensures that, given an input voltage and a connection to ground, the third reference pin outputs a stable voltage of 5 V (Fig. 4.17). By connecting this reference pin to Pin AREF of the Arduino and adjusting the code, it was possible to override the default voltage reference. The idea was implemented in the circuit as shown in Figure 4.18. However, despite official documentation of the Arduino's compatibility with an external reference voltage of up to 5 V [38], the AREF pin seemed to be limited to 3.3 V which was insufficient to cover the output voltage range of the pressure transducer from 1 V to 5 V. Ultimately, this concept was unsuccessful.

Figure 4.16: Image of the Analog Devices REF02C precision voltage regulator.

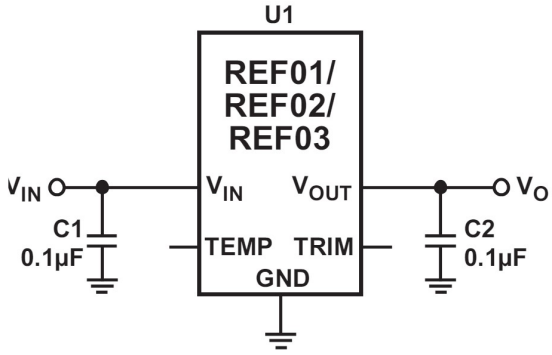

Figure 4.17: Schematic of the basic configuration of the Analog Devices REF02C for basic reference application. From Analog Devices (2016) [41].

Internal Reference Voltage

Operating on a similar principles as the external reference voltage initiative, a plan was devised to make use of the Arduino's internal reference voltage of 1.1 V. The Arduino internal reference voltage is widely regarded as reliable and stable. It should

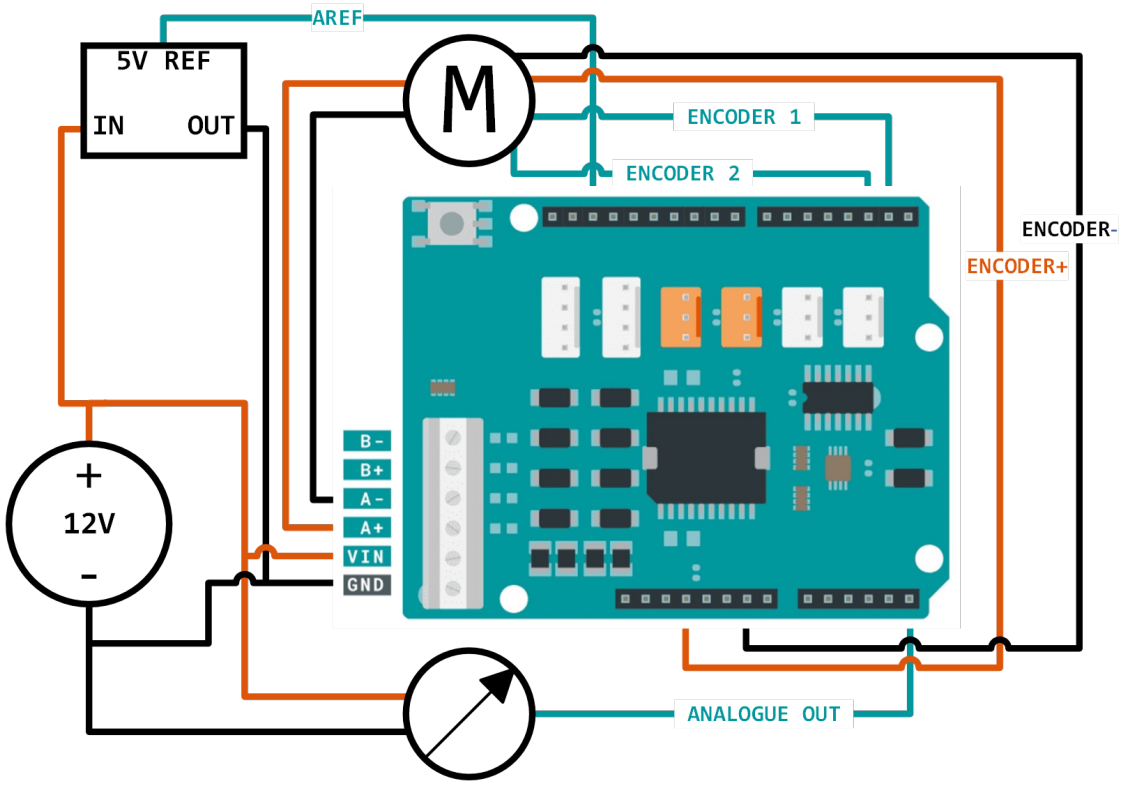

Figure 4.18: Circuitry with the external reference voltage idea implemented through the use of a 5 V voltage regulator.

be noted that, whilst the internal reference voltage of all Arduinos are approximately 1.1 V, the actual voltage varies slightly from device to device. For the device used in this project, this voltage was 1.078 V.

To read the output voltage of the pressure transducer against the internal reference voltage, it was necessary to scale down the output voltage to a maximum of 1.078 V. This was done by setting up a voltage divider with two resistors, represented by R_1 and R_2 in Figure 4.19. The values of R_1 and R_2 were determined through theoretical calculations followed by refinement with trial and error.

The theoretical calculations were based on two values: the desired voltage downscale factor and the nominal output current of the pressure transducer. The voltage downscale factor was easily determined and maintained constant through subsequent iterations. Since the pressure transducer's maximum output voltage of 5 V had to be scaled down to under 1.078 V, the factor was taken as $\frac{1}{5}$, including a safety margin. The output current of the pressure transducer was less robust, with limited documentation in the operation manual. An initial value of 20 mA was taken as a reasonable estimate considering several other mentions of the current magnitudes involved in the

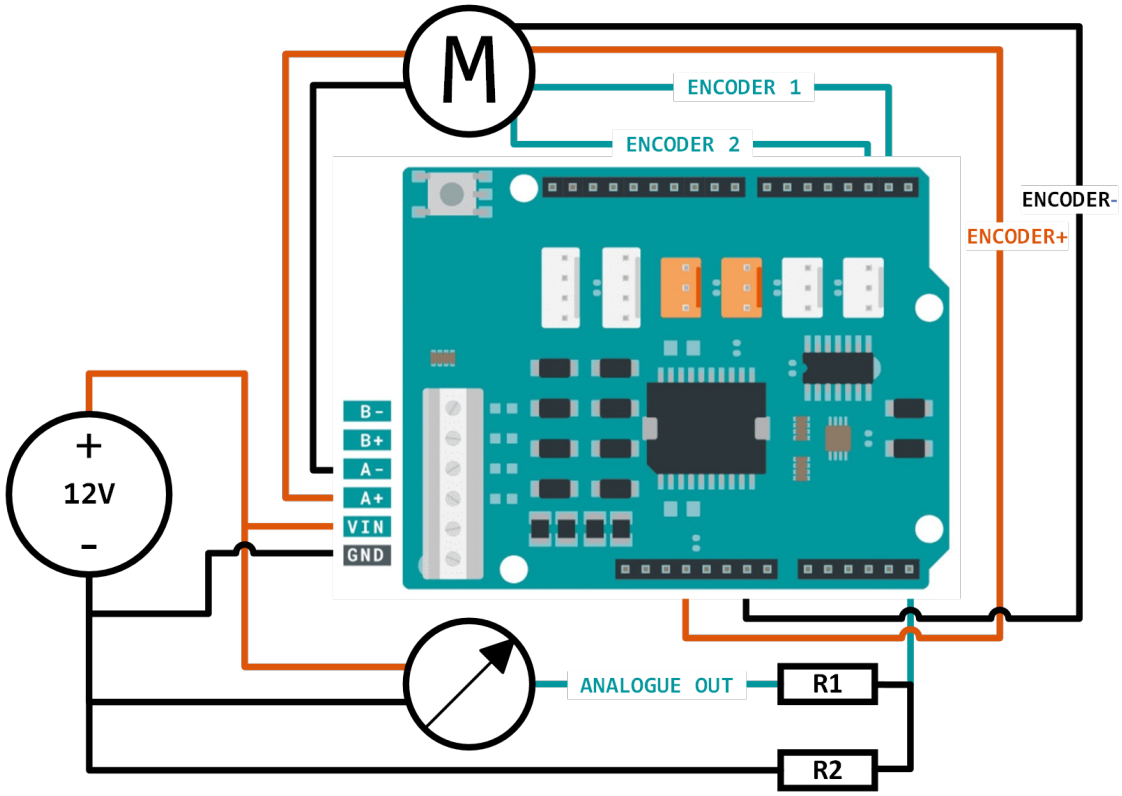

Figure 4.19: Circuitry with the internal reference voltage idea implemented through the use of a voltage divider.

operation of the pressure transducer [40]. The initial calculations, using these values, begins with two simultaneous equations:

$$I = 20 \times 10^{-3} = \frac{V_{in}}{R_1 + R_2}, \tag{4.1.18}$$

$$\frac{V_{out}}{V_{in}} = \frac{1}{5} = 1 - \frac{R_1}{R_1 + R_2}. \tag{4.1.19}$$

Solving Equations 4.1.18 and 4.1.19 results in $R_1 = 200\,\Omega$ and $R_2 = 50\,\Omega$, and the circuit was adapted to install a voltage divider of these resistors. However, upon testing, this set of resistance values returned output voltages different from the desired and theoretically imposed downscale factor of $\frac{1}{5}$.

Subsequently, several iterations were performed with resistance orders of magnitude ranging from 10^1 to 10^5, balancing the effects of excessive impedance and a desirable output voltage ratio. Ultimately, R_1 was chosen as $22.47\,\text{k}\Omega$ and R_2 as $5.86\,\text{k}\Omega$. This combination of resistors resulted in a voltage ratio of $\frac{V_{out}}{V_{in}} = 0.207$,

within a reasonable margin from $\frac{1}{5}$.

As a result, it was possible to scale down the pressure transducer output voltage range of 1-5 V to 0.207-1.034 V, which lies within the Arduino internal reference voltage of 1.078 V. The objective of referencing the pressure transducer output voltage against a stable voltage reference source, within the constraints of the Arduino's low internal reference voltage, was achieved. However, the fluctuations continued to persist.

Hardware Smoothing

As such, further efforts were made to make the fluctuations smoother. The next initiative was hardware smoothing, where capacitors were installed in parallel to key components of the circuit. Specifically, 100 nF capacitors were placed across the power supply, the motor and between ground and the pressure transducer output voltage. This arrangement is presented in Figure 4.20. However, despite this effort, the fluctuations did not improve noticeably.

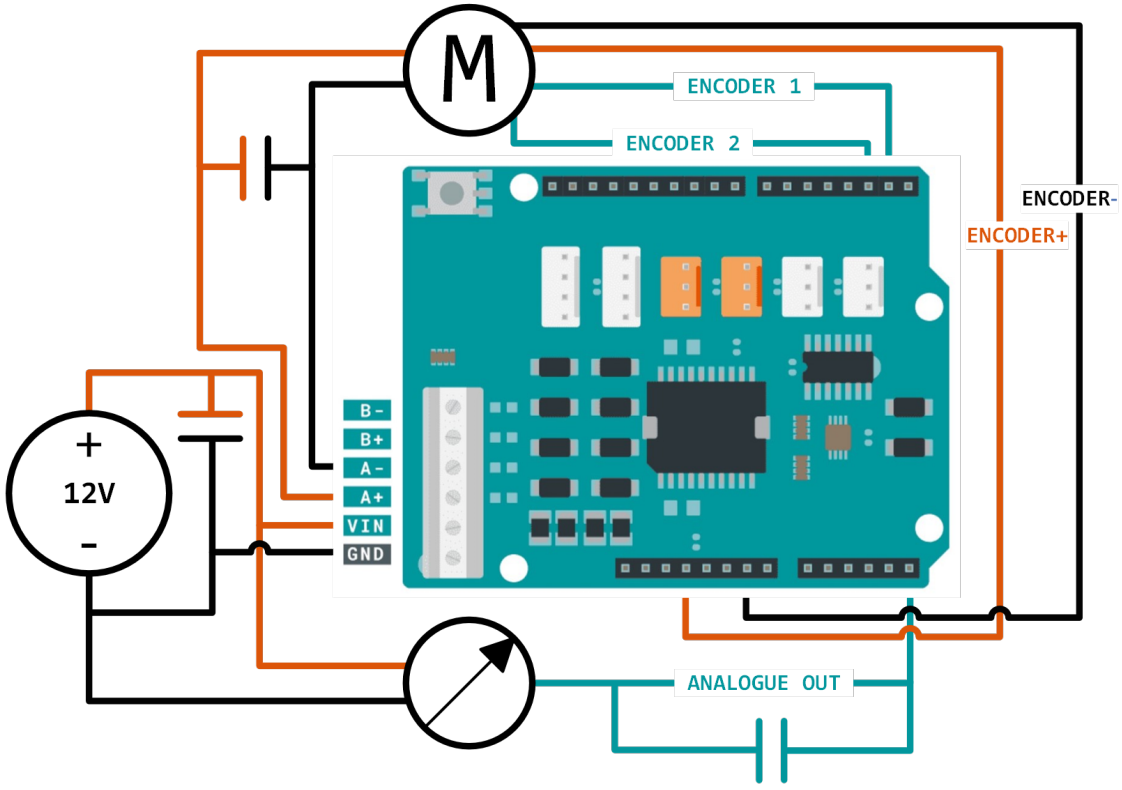

Figure 4.20: Circuitry with capacitors placed in parallel across key components for hardware smoothing.

Power Source Separation

Alternatively, a second initiative was taken to drive the motor and the pressure transducer using two separate power sources (Fig. 4.21). The intuition behind this change was that, by implementing electrical separation between the motor and the pressure transducer, the effect of motor powering on the pressure transducer output voltage would be reduced or completely eliminated. Whilst this proved to be untrue after testing, it offered critical information in terms of identifying the root cause of this voltage fluctuation behaviour. This finding eliminated numerous possibilities, highlighting the fact that the fundamental issue was with a fluctuating internal voltage within the Arduino.

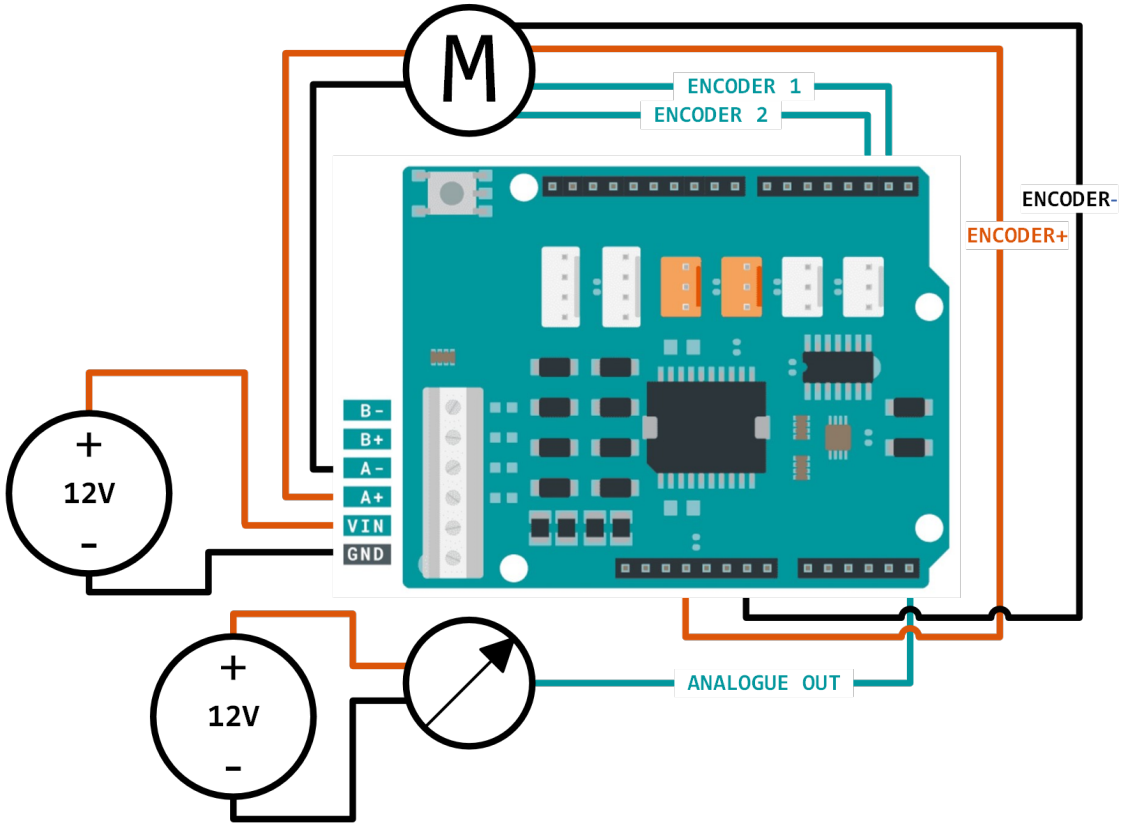

Figure 4.21: Circuitry with separate power supplies for the motor and the pressure transducer.

Software Smoothing

Given the unsuccessful efforts of hardware smoothing, a parallel approach was explored to conduct software smoothing through adaptation of the Arduino code. Two

techniques were implemented and tested, both based on the fundamental principle of time-averaging a large set of data.

The first concept was a `for` loop, within each high-level PID loop, to gather a large set of pressure readings and calculate a mean of the obtained data. Starting with a sample size of 10, which did not improve the data stability noticeably, the number was increased gradually up to 100, at which point there was some noticeable decrease in fluctuations. The size was further increased to several hundred and beyond, up to 1000, where the time-averaged data had attained sufficient stability for reliable use in the PID control system. Whilst this may appear to be a large number of cycles to loop through, the Arduino executes operations at 16 MHz [42], meaning that 1000 operations occur almost instantaneously at 6.25×10^{-5}s.

A potential improvement was identified to enhance the efficiency of the first concept. The idea, inspired by an Arduino post on analogue input smoothing [43], was to create a large array of pressure readings, removing the last entry and inserting the latest entry upon each PID loop. The logic was that this would make it unnecessary to perform 1000 operations within each loop, but rather a single operation, allowing for more efficient execution of the PID control system. However, there was a major flaw in this concept in the form of limited array size. Due to the maximum array size imposed by the Arduino compiler, the pressure data size was limited to approximately 400 entries, which provided insufficient smoothing. Therefore, the code was reverted back to the original version, which has since operated with sufficient frequency and reliability. This code is available in Listing C.1.

Circuit Adjustment to Separate V_{in} of Motor Shield and Arduino

Despite the successful implementation of software smoothing, there still remained a fundamental issue in the fluctuation of the Arduino internal voltage due to motor activity. As such, microcontroller specialist Jonathan Prevost was contacted for advice.

Prevost noticed that there was a direct circuit connection between the V_{IN} pin of both the Arduino and its motor shield. On the motor shield, this voltage is used to power the motor, whilst on the Arduino itself, this voltage is relevant to the reference voltage of the analogue reading from the pressure transducer. Therefore, the suggestion made was to severe this connection for the two to operate separately. This was conducted by physically cutting the circuit board connection using a craft cutter. Despite this effort, the voltage fluctuation continued to persist.

Forced Motor Movement During Pressure Measurements

As a last resort, code was implemented to force motor movement during pressure measurements. It was noticed that the Arduino voltage fluctuates only during the transitions between when the motor draws zero or non-zero current, and that it remains sufficiently stable if the motor is constantly drawing current. The intuition was that, by ensuring the motor is in motion during every pressure measurement, the reference voltage would be constant and the pressure readings would be accurate.

This idea was ultimately successful. In the code, it was implemented by initiating the motor to move in the anti-clockwise direction one line before the pressure reading, and stopping the motion one line after the pressure reading. The code is available in Listing C.1.

Physical ON/OFF switch

The final adjustment made to the setup was the installation of a manual switch to override the digital system. Whilst the parallel piping allowed for physical overriding of the argon flow from the cylinder into the glovebox, it was still necessary, and certainly useful, to have the capability to reset the digital control system without connecting to a computer.

To achieve this, an Eaton 1201A switch [44] was connected to the Arduino. Specifically, the wiring was such that the switch was simply placed between Pin GND and Pin 7. The full schematic of the circuitry is presented in Figure 4.22. To implement this setup in the Arduino code, the `toggleSwitch` function introduced by Arduino-GetStarted [45] was used. Whilst initial adjustments were made to decrease the debounce time from 50 ms to 20 ms, this change was eventually reverted for better performance.

The function was used to keep track of the state of the switch, `HIGH` for ON or `LOW` for OFF, and register any toggling of the switch. The code was adapted such that the PID control loop would only operate when the switch is ON. Furthermore, when the switch is turned ON after being turned OFF, the code was made to reset the calibration state and any remaining values of the PID system such as the integral term. As such, the system would recalibrate the motor encoder position and begin the PID loop from scratch. The detailed implementation of this function is depicted in the full code in Listing C.1.

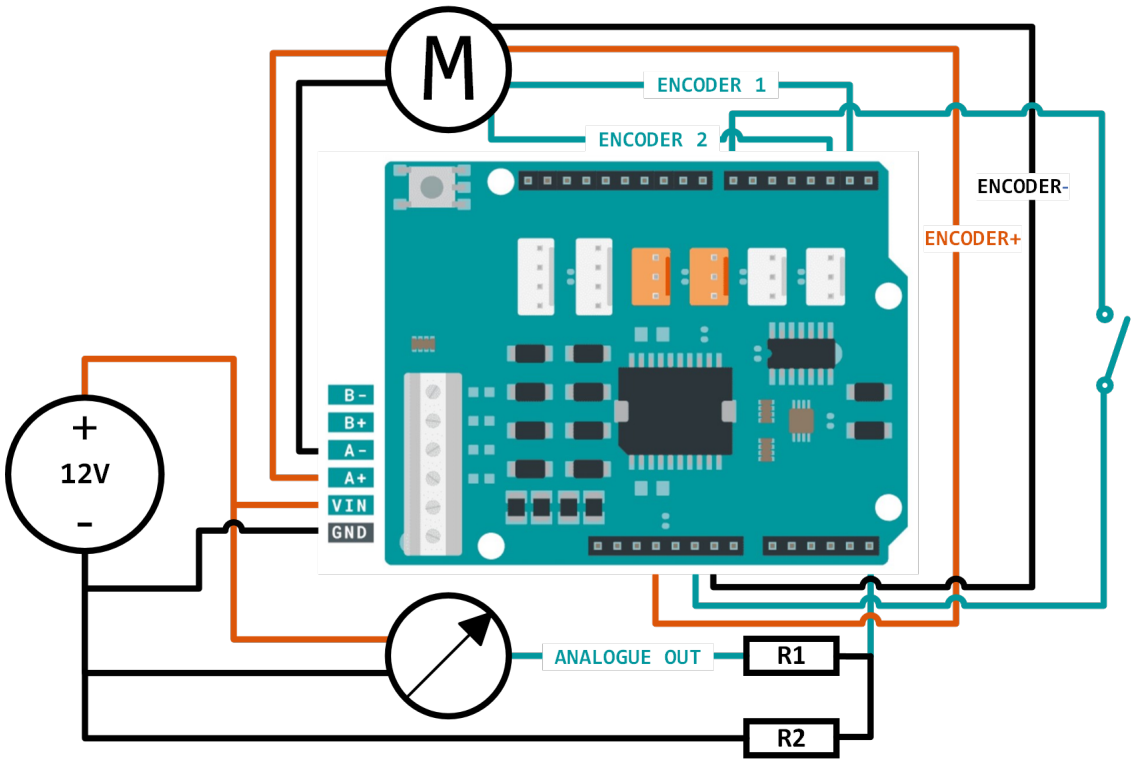

Figure 4.22: Circuitry with a two-state ON/OFF switch placed across Pin GND and Pin 7 for digital override of the system.

4.1.6 Final Setup

After all the troubleshooting attempts, implementations of the internal reference voltage, software smoothing, force motor movement and the ON/OFF switch were retained. The final setup is shown in Figure 4.23. There is certainly room for future improvements to the setup, which will be discussed in detail in Section 4.3.

4.2 Results

The PID tuning process was done through trial and error, settling with values of $K_p = 10.0$, $K_d = 0.1$ and $K_i = 0.0001$. From the final values, it is clear that the parameters tended towards an equilibrium dominated by the proportional term. Quantitative results were collected for a successful, stabilising run of the glovebox, from ambient atmospheric pressure to a target gauge pressure of 0.15 psi. Whilst the duration of this run is limited to 95 s, the system is capable and designed to maintain the slight positive argon pressure for as long as necessary.

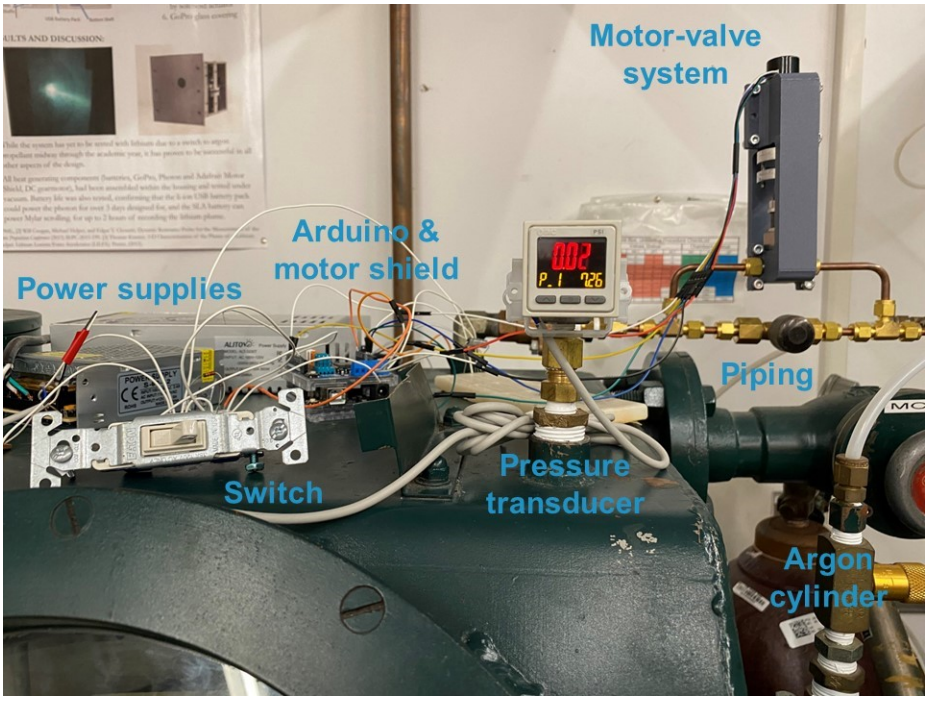

Figure 4.23: Final overall setup of the PID pressure controller system. The temporary wiring will be neatly soldered onto a small circuit board in the near future.

The internal pressure of the glovebox is plotted in Figure 4.24, along with the target pressure line for reference. The pressure begins at approximately 0.3 psi average gauge pressure, which is an accurate representation of the atmospheric pressure in EPPDyL. It quickly climbs to the target pressure and exceeds it slightly, thereafter maintaining a relatively stable pressure marginally under the target pressure. This is inevitable due to the unpredictable outflow of gas due to the movement of the gloves during operation. The critical point is that the pressure remains slightly above atmospheric pressure and never below, which is depicted in the graph (Fig. 4.24). This movement of the gloves is also the cause of pressure fluctuations throughout the run, and the movement itself was emphasised beyond nominal magnitudes during this test run. The step functions are due to the Arduino output rounding the pressure values to 2 decimal places.

The proportional, integral, derivative and total errors during this test run are also displayed in Figure 4.25. Here, proportional error is defined as the target pressure minus the current pressure. As expected considering the final values of the PID coefficients, the proportional term is clearly dominant in the plot. The derivative term is around two orders of magnitude smaller, whilst the integral term is almost negligible with a smooth line at zero. The green proportional line is completely overlapped by

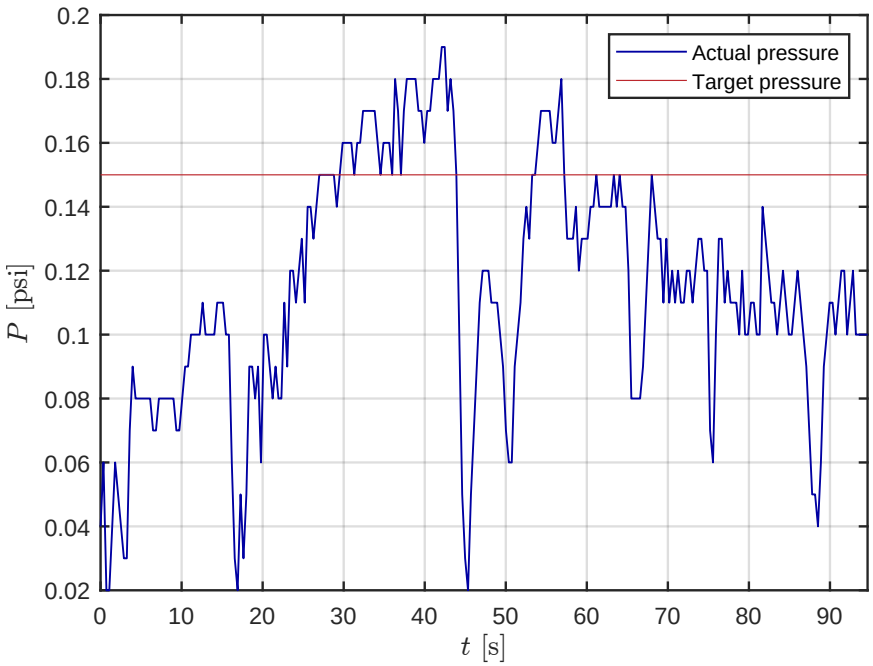

Figure 4.24: Actual and target pressures of the PID pressure controller over a 95 s run. The step functions are due to the Arduino output rounding the pressure to 2 decimal places.

the blue total line. These weightings make reasonable sense physically, as the objective of the PID system is to rapidly respond to pressure changes as opposed to consider integral contributions over a long duration. Again, the fluctuations in Figure 4.25 were due to the exaggerated movements of the gloves which caused pressure spikes.

The end of the PID function converts the error to a valve angle input. This is plotted against the actual valve angle on Figure 4.26. It is clear that the actual angle is smoother and lags slightly behind the input angle, which is inevitable due to the non-zero time it takes to achieve a certain valve angle. However, an implication of this is also that the motor sometimes struggled to fully close the valve, as seen between 33 s and 43 s. Whilst this is not of significant concern as there is also a proportional outflow of argon through the glove seals, it is certainly an area for improvement. An outflow of argon is not of concern as opposed to an inflow of air, and it was shown earlier that the internal pressure never fell below atmospheric pressure (Fig. 4.24).

4.3 Discussion

Overall, this PID pressure controller meets expectations in maintaining a slight positive internal argon pressure in the lithium handling glovebox. The setup was designed

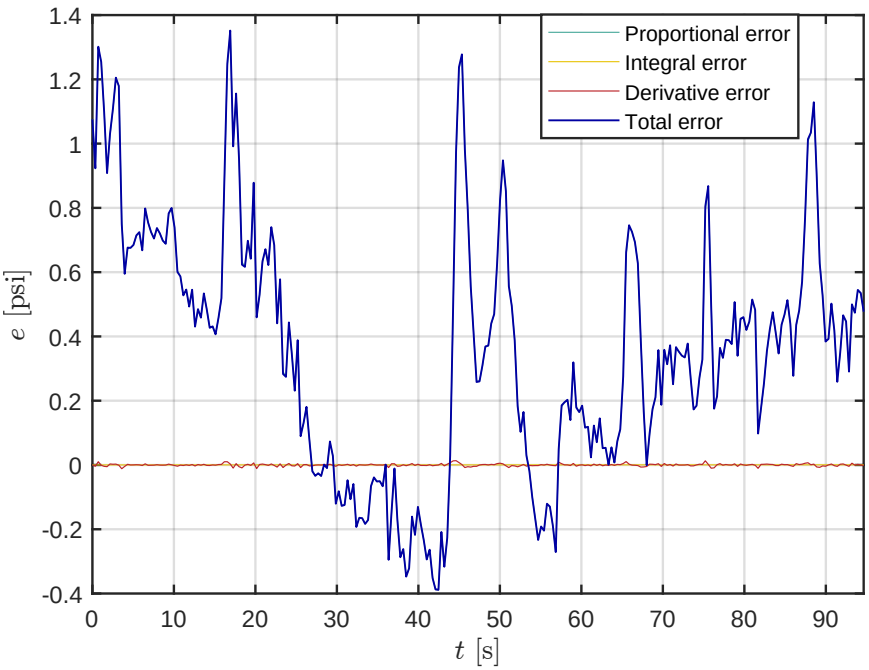

Figure 4.25: Proportional, integral, derivative and total errors of the PID pressure controller over a 95 s run. Proportional error is the target pressure minus the current pressure. Due to the dominant effect of the proportional term, the green proportional line is overlapped by the blue total line. Similarly, the yellow integral line is somewhat hidden underneath the red derivative line.

based on control system theory, and the design was realised with an emphasis on practical and reasonable simplicity. The system was built mostly from scratch, with work done on coding software, electronic hardware, physical design, machine shop manufacturing and piping mechanics. Whilst multiple obstacles stood in the way of realising the final system, successful efforts were made to achieve novel, creative and pragmatic solutions.

In particular, the low cost at which this system was developed is significant. A good quality mass flow controller, which quantifies and controls the argon mass flow rate, costs several thousand U.S. Dollars (USD) in the current market [46]. A high quality pressure controller, which regulates the argon mass flow rate to control the pressure within the glovebox, can cost upwards of $10,000 USD [47]. In this project, an equivalent system with far more capacity for personalised configurations was designed at a significantly lower total cost of $295.32 USD. This is an extremely cost-effective solution to developing a pressure-controlled glovebox, for which there is substantial demand and usage worldwide. The full cost breakdown is available in Table 4.2.

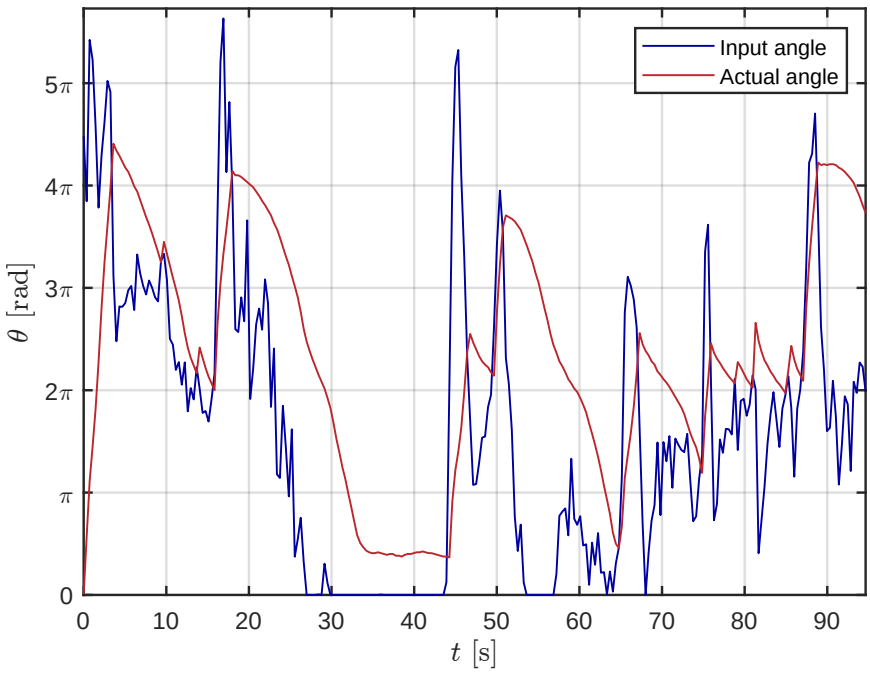

Figure 4.26: Input and actual valve angles of the PID pressure controller over a 95 s run. The actual angle lags behind the input angle due to the time-consuming practicality of rotating the valve.

Finally, whilst this system currently performs as required, there is certainly room for improvement. In particular, the solution to the Arduino voltage fluctuation was a valid workaround but did not address the root cause of the issue. Furthermore, whilst the BEMONOC motor was sufficient for this project, a stronger motor with higher torque and durability may be necessary to maintain proper operation of the system for many more years. These will be discussed, in detail, later in Section 5.2.2.

Table 4.2: Cost breakdown of the PID pressure controller project.

Component	**Cost (USD)**
BEMONOC 12 V DC Motor with Encoder	$14.88
Arduino Uno REV3	$23.96
Arduino Motor Shield REV3	$25.72
ALITOVE 12 V Power Supply	$23.99
SMC ZSE20AF Pressure and Vacuum Transmitter	$93.79
$\frac{1}{4}$" Copper Tubing and Yor-Lok Fitting	$112.98
Total	**$295.32**

Chapter 5

Conclusion and Future Work

This project investigates the thermal behaviour of the 30 kW LiLFA and explores the safety of the lithium handling process during thruster firing experiments. Using ANSYS Steady-State Thermal, the temperature profile of the thruster was obtained for both the heat-up phase and thruster firing, along with an experimental verification of the numerical simulations. Furthermore, a PID pressure controller was developed to reliably and autonomously maintain a safe internal pressure of the lithium handling glovebox. We have also laid out areas for future improvement and exploration to achieve higher fidelity thermal analyses and a more robust PID pressure controller.

5.1 Conclusion

Whilst EP possesses high fuel efficiency as a result of high exhaust velocities, its applications are often limited by low thrust. The development of MPD thrusters presents the opportunity to achieve high thrust capabilities whilst maintaining high efficiency, with potential application to heavy-cargo missions to the Moon and Mars. Currently, Princeton University's EPPDyL and NASA-JPL are working to develop the LiLFA. However, its thermal behaviour is not sufficiently understood. Furthermore, due to the hazardous nature of the lithium propellant, there is motive to improve the safety of the thruster firing process.

5.1.1 Thermal Modelling

ANSYS Steady-State Thermal was used to perform numerical simulations of the 30 kW thruster during two key phases: the heat-up phase and the thruster firing

phase. The heat-up phased simply involves heat generation within the heater rod, and thruster firing additionally considers the thermal effects of plasma on the anode and cathode. By defining temperature-dependent thermal conductivity and emissivity of all materials involved, along with thermal boundary conditions, steady-state temperature distributions of the thruster were obtained.

The thermal analysis was first set up with a preliminary study recreating an ANSYS simulation previously performed on the heater of a different EPPDyL Lorentz force accelerator. Subsequently, the heat-up phase was initially modelled with boundary conditions of a 22 °C room temperature clamping on the base cooling plate and a 22.6 kW area heat flux on the heater rod. This simulation was then refined for the same heat input but through a volumetric heat flux instead. The initial and refined results were consistent with each other. The refined heat-up simulation was experimentally validated at a lower power of 595 W, in a vacuum pressure of 10^{-1} Torr. The empirical data broadly agreed with simulation results, which were 1.3 % cooler at the thruster base, 17.7 % cooler on the feed pipe, 7.2 % cooler on the cathode plate and 19.5 % hotter on the anode plate. The hypothesis is that there was increased conductive heating from back of the heater due to the possible use of aluminium nitride instead of boron nitride for the insulator, as well as substantial heat generation in the heater back plate, both of which were unaccounted for in the simulation. This propagated most severely on the feed pipe, followed by the cathode plate. However, as the anode plate is furthest away from the heater back plate, the hypothesis is that unconsidered cooling effects outweighed the aforementioned extra heating. This cooling may have been the result of increased radiation from the boron nitride surface coating and non-zero conduction due to insufficient vacuum.

To explore beyond the heat-up phase, an ANSYS simulation was set up to model the actual thruster firing process. Taking advice from the EP team at NASA-JPL, additional boundary conditions were implemented with a 12 kW heat flux on the inner anode surface and a clamped temperature of 2600 °C on the multi-channel cathode rods. As a result, there was increased heating towards the front of the thruster, especially on the anode nozzle, anode plate and cathode plate. However, the cathode tip was significantly cooler than the initially constrained temperature, which must be investigated further.

Overall, this thermal analysis lays solid foundations from which to develop further in the future. The ANSYS thermal model is of reasonable fidelity, from which valuable findings can be obtained, although refinement is necessary to solve issues made apparent in this thesis. Fundamentally, this conservative upper bound study finds

that the thruster can withstand thermal loads during operation at 30 kW. It has also shown that it is possible to attach Type C thermocouples directly on the anode, as well as other locations of similar temperatures. This will enable even greater understanding of the thruster's thermal behaviour, likely generating knowledge on how to simultaneously progress the numerical model towards higher fidelity.

5.1.2 PID Pressure Controller

To improve the safety of the lithium handling process during thruster firing experiments, a PID pressure controller was designed and implemented to adjust the argon mass flow rate such that a slight positive gauge pressure is maintained in the glovebox. Previously, a second operator was required in addition to the main glovebox operator to monitor the gauge pressure and control the argon inflow. This is both inefficient in terms of resource allocation and inevitably prone to human error.

Starting from control theory, a PID control system was set up by reading the glovebox pressure with a pressure transducer, processing the data through a PID code on an Arduino with a motor shield and relaying the system input to a mechanically integrated motor-valve configuration between the argon cylinder and the glovebox. Despite numerous challenges, a working solution was realised and the glovebox now autonomously maintains a slight positive internal argon gauge pressure. This was achieved with an unprecedentedly low total cost of $295.32 USD, which is two orders of magnitude smaller than a high quality pressure controller on the current market.

5.2 Future Work

The findings of this thesis has generated new domains of improvement and further exploration.

5.2.1 Thermal Modelling

Many aspects of this thermal analysis were limited by the timeline of the thesis. As such, there are numerous minor improvements that can be made, given the opportunity to conduct more demanding simulations. Simulations should ideally be run on the full thruster geometry as opposed to a simplified version. Perhaps, a good balance would be to simplify complex edges of small parts, whilst maintaining key elements such as the molybdenum rod connections between the cathode and anode

plates. Furthermore, the mesh generation should be explored further to solve two persistent issues during this project. First, temperature-dependent emissivity values would provoke an insufficient memory error. Second, temperature constraint boundary conditions returned unpredictable and likely flawed results. From brief research, these are both potentially the effect of imperfect mesh geometries on local heat transfer calculations. Finally, the cooling power of the thruster base can be modelled with more complex boundary conditions to capture conductive and convective cooling phenomena.

Importantly, the material of the insulator between the back of the heater and the cathode plate should be identified and adapted in the simulation. The internal heat generation of the heater should also be adjusted such that there is appropriate heating of the back plate. This can be calculated by obtaining the cross sectional area of each segment of the circuit and using graphite's resistivity to determine the volumetric heating throughout current-carrying sections of the heater.

The experimental setup could also be improved. The tank should ideally be vacuumed down to at least 10^{-4} Torr, where the assumption of zero convection is entirely valid. Furthermore, the setup should be given a longer duration of time to completely reach steady-state, possibly over several days.

Beyond direct improvements, this thesis has opened up possibilities for further exploration. Whilst Type C thermocouples can be implemented for direct measurement of hotter surfaces, optical pyrometry can be performed from the tank windows to measure even higher temperatures, such as at the cathode tip. With a higher fidelity numerical model and experimental measurements of more surfaces, it may be possible to justify material changes for cost reduction.

5.2.2 PID Pressure Controller

The design of the PID pressure control system can be improved for increased reliability, durability and robustness.

First, the current motor should be replaced with a stronger motor. The BE-MONOC motor is sufficient for now, but it operates at its maximum PWM and a gradual decline of its performance has been noticed. Furthermore, especially during calibration, there are several occasions where the motor is forced to stall out. This slowly damages the brushed motor, and therefore a brushless motor with higher torque may be preferable in the future.

Second, a higher quality pressure transducer is desirable for more accurate pressure

readings using the Arduino. Whilst the accuracy of the transducer itself is sufficient, its resolution is insufficient and results in large fluctuations when reading its analogue voltage through the Arduino. The first method to address this is to use a transducer with less accuracy uncertainty, whilst the alternative is to implement a transducer with a smaller measurement range. A combination of both ideas would also be appropriate. For a system that requires operation between approximately $-0.5\,\text{psi}$ and $+0.5\,\text{psi}$, the transducer range of $-14.5\,\text{psi}$ and $+14.5\,\text{psi}$ provides an excessively low resolution. However, given the $400 USD budget of this thesis, it was not possible to invest in a higher quality pressure transducer.

The project could have also benefited from a higher quality microcontroller, particularly one that would not have been so affected by the current draw of the motor, although this can cost several thousand USD. Another workaround would be to implement the ADC and motor controller separately, perhaps using one Arduino to take the pressure readings, process it through a PID code and relay a digital signal to a second Arduino with a motor shield to move the motor accordingly. This can certainly be added to the current setup, but could not be attempted within the timeline of this thesis.

Finally, there is still capacity for more PID tuning. The current PID settings meet expectations, but it is most likely possible to achieve more optimal PID constants with further testing. It is also necessary to neatly solder all the temporary wiring onto a small circuit board, as the current setup (Fig. 4.23) is somewhat disorganised. Soldering the circuit will additionally eliminate any risk of wires getting disconnected or mixed up in the future.

References

[1]Robert G. Jahn and Edgar Y. Choueiri. "Electric Propulsion". In: *Encyclopedia of Physical Science and Technology, Third Edition* 5 (2002), pp. 125–141 (cit. on pp. 1, 4, 5).

[2]Edgar Y. Choueiri. *Lecture Note: Space Mission Analysis*. 2023. (Visited on 03/15/2024) (cit. on pp. 3, 4).

[3]Edgar Choueiri. "Fundamental Limit of Self-Field MPD Thruster Efficiency". In: Cambridge, MA, USA, June 2022 (cit. on p. 5).

[4]Moscow Aviation Institute. *Reports on the 100kW Lithium Thruster Development between RIAME MAI and NASA*. en. Tech. rep. RIAME, Moscow Aviation Institute, Jan. 1995 (cit. on p. 5).

[5]Sean Reilly, Richard Hofer, and Scott Hall. "Thermal Analysis of the 100-kW class X3 Hall Thruster". eng. In: (July 2017). Publisher: 47th International Conference on Environmental Systems. URL: http://hdl.handle.net/2346/73103 (visited on 03/16/2024) (cit. on p. 6).

[6]Jonathan Van Noord. "NEXT Ion Thruster Thermal Model". en. In: *43rd AIAA / ASME / SAE / ASEE Joint Propulsion Conference & Exhibit*. Cincinnati, OH: American Institute of Aeronautics and Astronautics, July 2007. ISBN: 978-1-62410-011-6. DOI: 10.2514/6.2007-5218. (Visited on 02/07/2024) (cit. on p. 6).

[7]Jack Hollingsworth. "A Graphite Orificed Hollow Cathode for an Argon Magnetoplasmadynamic Thruster". en_US. Accepted: 2017-07-24T14:25:15Z. PhD thesis. Princeton University, May 2017. URL: http://arks.princeton.edu/ark:/88435/dsp01qb98mj096 (visited on 01/21/2024) (cit. on pp. 6, 7).

[8]G Emsellem, A D Kodys, and E Y Choueiri. "Thermal Analysis of a Lorentz Force Accelerator with an Open Lithium Heat Pipe". en. In: *26th International Electric Propulsion Conference* (1999). URL: https://alfven.princeton.edu/publications/pdf/emsellem-iepc-1999-166.pdf (visited on 03/16/2024) (cit. on pp. 7, 23–26, 43).

[9]Dan Lev and David Stein. *Lithium System Operation*. Tech. rep. Mar. 2011. (Visited on 03/16/2024) (cit. on pp. 7, 8, 10).

[10]William J Coogan. "Thrust Scaling in Applied-Field Magnetoplasmadynamic Thrusters". en. PhD thesis. Princeton University, Sept. 2018. (Visited on 04/14/2024) (cit. on pp. 8, 9).

[11]Edgar Y. Choueiri. *Spacecraft Thermal Control*. 2024. (Visited on 04/12/2024) (cit. on pp. 11–15).

[12]Robert D. Karam. *Satellite thermal control for systems engineers*. eng. Progress in astronautics and aeronautics 181. Reston, Va: American Institute of Aeronautics and Astronautics, 1998. ISBN: 978-1-56347-276-3 (cit. on p. 12).

[13]Vincent L. Pisacane, ed. *Fundamentals of space systems*. 2nd ed. The Johns Hopkins University/Applied Physics Laboratory series in science and engineering. Oxford ; New York: Oxford University Press, 2005. ISBN: 978-0-19-516205-9 (cit. on p. 12).

[14]Royal Society of Chemistry. *Molybdenum - Element information, properties and uses — Periodic Table*. 2024. URL: https://www.rsc.org/periodic-table/element/42/molybdenum (visited on 04/14/2024) (cit. on p. 17).

[15]N. S. Rasor and J. D. McClelland. "Thermal properties of graphite, molybdenum and tantalum to their destruction temperatures". In: *Journal of Physics and Chemistry of Solids* 15.1 (Aug. 1960), pp. 17–26. ISSN: 0022-3697. DOI: 10.1016/0022-3697(60)90095-0. (Visited on 02/28/2024) (cit. on p. 17).

[16]L. Northcott. *Molybdenum (Metallurgy of Rarer Metals)*. English. Academic Press, 1956. ISBN: 040826500. (Visited on 04/14/2024) (cit. on p. 17).

[17]Erhard Dörre and Heinz Hübner. *Alumina: processing, properties, and applications*. eng. Materials research and engineering. Berlin Heidelberg New York [etc.]: Springer-Verlag, 1984. ISBN: 978-3-540-13576-0 978-0-387-13576-2 (cit. on p. 18).

[18]Wolfgang Bauer, Alexander Moldenhauer, and Alexander Platzer. "Emissivities of ceramic materials for for high temperature processes". In: *Optical Diagnostics*. Vol. 5880. SPIE, Aug. 2005, pp. 263–272. DOI: 10.1117/12.624512. (Visited on 03/07/2024) (cit. on p. 18).

[19]J. G. Hust and A. B. Lankford. "Thermal conductivity of aluminum, copper, iron, and tungsten for temperatures from 1 K to the melting point:" en. In: *National Bureau of Standards* (June 1984), p. 256. DOI: 10.6028/NBS.IR.84-3007 (cit. on p. 18).

[20]Erik Lassner and Wolf-Dieter Schubert. *Tungsten: Properties, Chemistry, Technology of the Element, Alloys, and Chemical Compounds*. en. Boston, MA: Springer US, 1999. ISBN: 978-1-4615-4907-9. DOI: 10.1007/978-1-4615-4907-9. (Visited on 04/20/2024) (cit. on pp. 18, 40).

[21]Entegris. *Graphite Properties and Characteristics For Industrial Applications*. 2020. (Visited on 04/14/2024) (cit. on p. 19).

[22]QS Advanced Materials. *QS Advanced Materials BN99 Specification*. 2024. URL: https://www.qsrarematerials.com/BN_docs/QS_BN99.pdf (visited on 04/14/2024) (cit. on pp. 19, 20).

[23]Guoliang Chen, Yaming Wang, Yongchun Zou, et al. "Hexagonal boron nitride and alumina dual-layer coating for space solar thermal shielding". In: *Chemical Engineering Journal* 421 (Oct. 2021), p. 127802. ISSN: 1385-8947. DOI: 10.1016/j.cej.2020.127802. (Visited on 03/07/2024) (cit. on p. 20).

[24]Corning. *MACOR Machinable Glass Ceramic For Industrial Applications*. 2012. URL: https://www.corning.com/media/worldwide/csm/documents/71759a443535%20431395eb34ebead091cb.pdf (visited on 03/07/2024) (cit. on p. 20).

[25]Gennaro Cardone, Andrea Ianiro, Gennaro dello Ioio, et al. "Temperature maps measurements on 3D surfaces with infrared thermography". en. In: *Experiments in Fluids* 52.2 (Feb. 2012), pp. 375–385. ISSN: 1432-1114. DOI: 10.1007/s00348-011-1225-9. (Visited on 03/07/2024) (cit. on p. 20).

[26]Britannica. *Lithium — Definition, Properties, Use, & Facts — Britannica*. en. Apr. 2024. URL: https://www.britannica.com/science/lithium-chemical-element (visited on 04/17/2024) (cit. on p. 32).

[27]Inc. Omega Engineering. *Mass Flow Meters — Flow Meters — Flow Instruments — Omega*. 2024. URL: https://www.omega.com/en-us/flow-instruments/flow-

meters/c/mass-flow-meters?view=list (visited on 03/27/2024) (cit. on pp. 36, 48).

[28]Eric T Malroy. "Free Molecular Heat Transfer Programs for Setup and Dynamic Updating the Conductors in Thermal Desktop". en. In: Sept. 2007. URL: https://ntrs.nasa.gov/api/citations/20070030243/downloads/20070030243.pdf (visited on 04/23/2024) (cit. on p. 38).

[29]S. Kunze, R. Groll, B. Besser, et al. "Molecular diameters of rarefied gases". en. In: *Scientific Reports* 12.1 (Feb. 2022). Publisher: Nature Publishing Group, p. 2057. ISSN: 2045-2322. DOI: 10.1038/s41598-022-05871-y. (Visited on 04/24/2024) (cit. on p. 38).

[30]Dan Lev. "Investigation of Efficiency in Applied Field MagnetoPlasmaDynamic Thrusters". PhD thesis. Princeton, New Jersey: Princeton University, Jan. 2012. (Visited on 04/14/2024) (cit. on p. 41).

[31]K. Watari, K. Ishizaki, and T. Fujikawa. "Thermal conduction mechanism of aluminium nitride ceramics". en. In: *Journal of Materials Science* 27.10 (May 1992), pp. 2627–2630. ISSN: 1573-4803. DOI: 10.1007/BF00540680. (Visited on 04/24/2024) (cit. on p. 45).

[32]Omega Engineering. *Revised Type C Thermocouple Reference Tables*. 2024. URL: https://sea.omega.com/temperature/Z/pdf/z239-240.pdf (visited on 04/24/2024) (cit. on p. 46).

[33]SMC Corporation. *ZSE20A(F) High Pressure Digital Pressure Switch 3 Screen Display*. en. 2024. URL: https://www.smcusa.com/products/zse20a(f)-high-pressure-digital-pressure-switch-3-screen-display~170849 (visited on 04/12/2024) (cit. on p. 51).

[34]BEMONOC. *BEMONOC 25GA370 DC Encoder Metal Gearmotor 12V High Speed 150RPM Gear Motor with Two-Channel Hall Effect Encoder for DIY Parts : Industrial & Scientific*. Apr. 2024. URL: https://www.amazon.com/25GA370-Encoder-Metal-Gearmotor-150RPM/dp/B07GNFYGYQ/ref=sr_1_6?crid=2N44Z8XR1E6XF&keywords=12v%2Bdc%2Bmotor%2Bwith%2Bencoder&

qid=1705869370&sprefix=12v%2Bdc%2Bmotor%2Bwith%2Bencoder%2Caps%2C67&sr=8-6&th=1 (visited on 04/09/2024) (cit. on p. 51).

[35]Swagelok. *Stainless Steel Severe Service Union Bonnet Needle Valve, 0.35 Cv, 1/4 in. Swagelok Tube Fitting, PTFE Regulating Stem — Severe-Service Needle Valves, N and HN Series — Needle and Metering Valves — Valves — All Products — Swagelok*. Apr. 2024. URL: https://products.swagelok.com/en/c/straight-pattern-regulating-stem/p/SS-3NTRS4 (visited on 04/09/2024) (cit. on p. 51).

[36]The Bored Robot. *Synchronizing Motor Position with Encoders, PID Control and Arduino*. Oct. 2023. URL: https://www.youtube.com/watch?v=bsB5shP3vls (visited on 04/11/2024) (cit. on pp. 54, 55).

[37]Arduino. *analogRead() - Arduino Reference*. Nov. 2023. URL: https://www.arduino.cc/reference/en/language/functions/analog-io/analogread/ (visited on 04/11/2024) (cit. on p. 55).

[38]Arduino. *analogReference() - Arduino Reference*. Nov. 2023. URL: https://www.arduino.cc/reference/en/language/functions/analog-io/analogreference/ (visited on 04/11/2024) (cit. on pp. 56, 58).

[39]Nick Gammon. *Gammon Forum : Electronics : Microprocessors : ADC conversion on the Arduino (analogRead)*. Feb. 2015. URL: https://www.gammon.com.au/adc (visited on 04/11/2024) (cit. on p. 56).

[40]SMC Corporation. *SMC ZSE20A(F)/ISE20A Operation Manual*. June 2023. URL: https://www.smcworld.com/upfiles/manual/en-jp/files/PSxx-OMU0003.pdf (visited on 04/10/2024) (cit. on pp. 56, 60).

[41]Analog Devices. *Precision 2.5 V, 5.0 V, and 10.0 V Voltage References: REF01 / REF02 / REF03*. 2016. URL: https://www.analog.com/media/en/technical-documentation/data-sheets/ref01_02_03.pdf (visited on 04/12/2024) (cit. on p. 58).

[42]Royal Hernandez. *Arduino Clock Speed: A Guide To Different Board Speeds*. en-US. Apr. 2023. URL: https://embedwiz.com/arduino-clock-speed/ (visited on 04/12/2024) (cit. on p. 63).

[43]Arduino Docs. *Smoothing Readings From an Analog Input — Arduino Documentation*. Aug. 2022. URL: https://docs.arduino.cc/built-in-examples/analog/Smoothing/ (visited on 04/12/2024) (cit. on p. 63).

[44]Eaton. *1201A — Eaton construction grade toggle switch*. en_US. 2024. URL: https://www.eaton.com/us/en-us/skuPage.1201A.html (visited on 04/12/2024) (cit. on p. 64).

[45]ArduinoGetStarted. *Arduino - Switch — Arduino Tutorial*. en. 2024. URL: https://arduinogetstarted.com/tutorials/arduino-switch (visited on 04/12/2024) (cit. on p. 64).

[46]MATHESON. *Specialty Gas Equipment - Flow Measurement - Mass flow controllers - MATHESON Online Store*. 2024. URL: https://store.mathesongas.com/mass-flow-controllers/ (visited on 04/22/2024) (cit. on p. 68).

[47]Instrumart. *Pressure Controllers — Instrumart*. 2024. URL: https://www.instrumart.com/categories/6130/pressure-controllers (visited on 04/22/2024) (cit. on p. 68).

Appendix A

Appendix 1

Table A.1: Thermal conductivity of molybdenum at varying temperatures.

Temperature [K]	Thermal conductivity [$\mathrm{W\,m^{-1}\,K^{-1}}$]
273.0	130.1
300.0	127.2
400.0	120.2
1083.2	105.0
1180.4	102.9
1277.7	100.8
1356.9	99.3
1442.9	97.7
1537.9	96.0
1623.9	94.7
1703.1	93.9
1773.2	93.1
1863.7	92.2
1972.3	91.2
2078.6	90.5
2178.2	89.7
2266.4	89.1
2370.5	88.3
2470.0	87.9
2587.7	87.6
2685.0	87.2
2780.0	86.8
2877.3	86.6

Table A.2: Emissivity of molybdenum at varying temperatures.

Temperature [K]	Emissivity
1000	0.096
1200	0.121
1400	0.145
1600	0.168
1800	0.189
2000	0.210
2200	0.230
2400	0.248
2600	0.265
2800	0.281
2895	0.290

Table A.3: Thermal conductivity of alumina at varying temperatures.

Temperature [K]	Thermal conductivity [$\mathrm{W\,m^{-1}\,K^{-1}}$]
293.0	35.94
308.0	34.25
325.2	32.39
342.4	30.59
361.7	28.84
383.2	27.04
400.4	25.70
417.6	24.41
432.6	23.17
449.8	21.99
469.1	20.75
488.5	19.62
531.4	17.97
567.9	16.58
608.7	15.04
634.5	14.21
662.4	13.29
705.4	12.10
737.6	11.33
791.3	10.04
853.6	9.01
911.5	8.39
1014.6	7.52
1197.2	6.44
1102.7	6.90
1255.2	6.13
1354.0	5.72
1439.9	5.56
1515.0	5.56
1616.0	5.51
1714.8	5.51
1817.8	5.61
1916.6	5.72
2017.6	5.92
2094.9	6.23
2167.9	6.49

Table A.4: Emissivity of alumina at varying temperatures.

Temperature [K]	Emissivity
474	0.733
533	0.710
589	0.686
650	0.657
710	0.630
770	0.604
831	0.581
892	0.557
952	0.535
1015	0.512
1074	0.492
1135	0.474
1194	0.459
1252	0.446
1311	0.434
1371	0.419
1426	0.410
1473	0.403

Table A.5: Thermal conductivity of tungsten at varying temperatures.

Temperature [K]	Thermal conductivity [$\mathrm{W\,m^{-1}\,K^{-1}}$]
10	488
12	574
14	651
16	718
18	768
20	799
25	786
30	692
35	586
40	494
45	418
50	357
60	281
70	250
80	236
90	225
100	217
150	197
200	189
250	182
300	174
400	158
500	145
600	136
700	130
800	125
900	122
1000	119
1100	116
1200	114
1300	111
1400	110
1500	108
1600	106
1800	103
2000	101
2200	99
2400	97
2600	95
2800	93
3000	92

Table A.6: Emissivity of tungsten at varying temperatures

Temperature [K]	Emissivity
400	0.344
800	0.331
1200	0.311
1600	0.283
2000	0.249
2400	0.208
2800	0.160
3200	0.105
3600	0.042

Table A.7: Thermal conductivity of graphite at varying temperatures.

Temperature [K]	Thermal Conductivity [$\mathrm{W\,m^{-1}\,K^{-1}}$]
300.9	113.78
387.0	106.22
475.6	99.35
569.1	92.14
662.6	85.63
778.2	78.06
906.2	70.85
1061.2	63.11
1199.0	57.48
1336.8	52.90
1469.6	49.21
1622.2	46.57
1767.4	44.99
1902.7	44.63

Table A.8: Emissivity of graphite at varying temperatures.

Temperature [K]	Emissivity
1800	0.787
1900	0.793
2000	0.799
2100	0.805
2200	0.811
2300	0.817
2400	0.823
2500	0.829
2600	0.835
2700	0.841
2800	0.847
2900	0.853

Table A.9: Thermal conductivity of MACOR® at varying temperatures.

Temperature [K]	Thermal Conductivity [$\mathrm{W\,m^{-1}\,K^{-1}}$]
297.2	1.54
314.6	1.50
333.8	1.47
354.8	1.44
378.6	1.42
411.6	1.39
450.0	1.37
485.7	1.36
532.4	1.35
589.1	1.35
648.6	1.36
705.3	1.36
761.1	1.36
811.5	1.36
864.5	1.35
911.2	1.33
959.7	1.31
1007.3	1.29
1039.3	1.27
1072.2	1.25

Appendix B

Appendix 2

Defaults	
Physics Preference	Mechanical
Element Order	Program Controlled
Element Size	Default
Sizing	
Use Adaptive Sizing	Yes
Resolution	2
Mesh Defeaturing	Yes
Defeature Size	Default
Transition	Slow
Span Angle Center	Fine
Initial Size Seed	Part
Bounding Box Diagonal	0.54507 m
Average Surface Area	1.882e-003 m^2
Minimum Edge Length	3.9268e-004 m
Quality	
Check Mesh Quality	Yes, Errors
Error Limits	Aggressive Mechanical
Target Element Quality	Default (5.e-002)
Smoothing	High
Mesh Metric	Element Quality
Min	6.5415e-002
Max	0.99998
Average	0.73182
Standard Deviation	0.15612
Inflation	
Use Automatic Inflation	None
Inflation Option	Smooth Transition
Transition Ratio	0.272
Maximum Layers	5
Growth Rate	1.2
Inflation Algorithm	Pre
Inflation Element Type	Wedges
View Advanced Options	No
Advanced	
Number of CPUs for Parallel Part Meshing	Program Controlled
Straight Sided Elements	No
Rigid Body Behavior	Dimensionally Reduced
Triangle Surface Mesher	Program Controlled
Topology Checking	Yes
Pinch Tolerance	Please Define
Generate Pinch on Refresh	No
Statistics	
Nodes	162253
Elements	87591
Show Detailed Statistics	No

Figure B.1: Global mesh settings of the ANSYS simulation setup.

Appendix C

Appendix 3

```
// PID gains (ADJUST)
float Kp = 10.0;
float Kd = 0.1;
float Ki = 0.0001;
const double uScale = 500; // Constant that relates
    encoder position to valve angle (encoder position)
float u = 0;

// Switch
#include <ezButton.h>
ezButton toggleSwitch(7);  // Create ezButton object
    that attach to PIN 7;

// Vref internal = 1.092 V, default = 5.05 V, default w/
    power supply = 4.52 V
// ADJUST values (these are unique to each manufactured
    Arduino)
const double VrefInternal = 1.078;
const double VrefDefault = 5.05;
const double VrefPower = 4.41; //4.45
double Vdivider = 5.31;

// Define pin #s
```

```
#define DIR 12 // DIR = 0 is CW (close valve), DIR = 1 is ACW (open valve)
#define PWM 3
#define encoderPinA 2
#define encoderPinB 4

// Initialise variables
volatile long encoderCount = 0;
double currentP = 0;
bool calibrated = 0;
int zeroPos = 0;
int pos = 0;

// Set constants
const int maxPos = 1680; // 240 pulses per revolution
const int maxPWM = 255; // Maximum PWM of motor
const int pTolerance = 10; // Tolerance to allow when setting valve area (to prevent PID going out of control)
const int avgCount = 1000; // Sample # for time-averaged pressure reading

// Initialise variables for PID control
long previousTime = 0;
float ePrevious = 0;
int setPos = 0;

// Initialise variables
double deltaT;
double e;
double eDerivative;
double eIntegral;


// Set up Arduino loop
void setup() {
```

```
52    Serial.begin(9600);
53
54    // Set pin modes
55    pinMode(DIR, OUTPUT);
56    pinMode(PWM, OUTPUT);
57    pinMode(encoderPinA, INPUT);
58    pinMode(encoderPinB, INPUT);
59    pinMode(A5, INPUT);
60
61    // Interrupt for encoder
62    attachInterrupt(digitalPinToInterrupt(encoderPinA),
          handleEncoder, RISING);
63
64    // Set debounce time for switch
65    toggleSwitch.setDebounceTime(50);
66
67    // Turn on internal 1.1V reference instantly
68    ADMUX = bit (REFS0) | bit (REFS1);
69    analogReference(INTERNAL);
70  }
71
72
73  // Execute Arduino loop
74  void loop() {
75
76    // Process switch behaviour
77    toggleSwitch.loop();
78    int state = toggleSwitch.getState(); // Obtain switch
          state
79    if (state == LOW){analogWrite(PWM, 0);calibrated=0;}
          // If switch is OFF, reset calibration and stop
          motor
80    if (toggleSwitch.isReleased()){
81      Serial.println(" ");
82      Serial.println("ON -> OFF"); // Display switch change
83      calibrated=0;
```

```
84      ePrevious = 0;
85      eIntegral = 0; // Reset tracking variables if switch
            is moved
86    }
87    if (toggleSwitch.isPressed()){
88      Serial.println(" ");
89      Serial.println("OFF -> ON"); // Display switch change
90      calibrated=0;
91      ePrevious = 0;
92      eIntegral = 0; // Reset tracking variables if switch
            is moved
93    }
94
95    // Display switch state
96    Serial.println(" ");
97    Serial.print("state ");
98    Serial.println(state);
99
100   // Enter PID loop if switch is ON
101   if (state == HIGH){
102
103     // Recalibrate is calibration binary is zero
104     if (calibrated == 0){
105       calibratePos();
106     }
107     pos = encoderCount - zeroPos; // Calculate current
            position relative to zero position
108
109     double targetP = 0.15; // Set point in psi
110
111     // Start moving motor before pressure reading
112     digitalWrite(DIR, 1);
113     analogWrite(PWM, maxPWM);
114     // Read time-averaged pressure from transducer
115     int count = 0;
116     double tempP = 0;
```

```
117     while (count < avgCount){
118         tempP = tempP + analogRead(A5);
119         count++;
120     }
121     currentP = tempP / avgCount;
122 
123     // Stop motor after pressure reading
124     analogWrite(PWM, 0);
125 
126     // Display analogue pressure reading
127     Serial.print("ANLG = ");
128     Serial.print(currentP);
129     Serial.print(", ");
130     currentP =
            ((((((currentP+0.5)/1024)*VrefInternal*Vdivider)
            -1)/4)*200)-100; // Analogue to kPa
131     currentP = currentP*0.145038; // kPa to psi
132 
133     // Display psi pressure reading
134     Serial.print("currentP = ");
135     Serial.print(currentP);
136     Serial.print(", ");
137 
138     // PID computation
139     u = pidController(targetP, currentP, Kp, Kd, Ki);
140     u = u*uScale; // Scaling input from pressure to
            encoder position
141     if (u < 0){
142       u = 0; // Prevents "negative" input (physically
              impossible with one-way valve)
143     }
144     if (u > maxPos){
145       u = maxPos; // Prevents maxing out valve
146     }
147 
148     // Display input encoder position
```

```
149       Serial.print("u = ");
150       Serial.print(u, 5);
151       Serial.print(", ");
152
153       // Move motor to desired input encoder angle
154       setMotor(pos, u);
155       delay(200);
156
157       // Display current encoder position
158       Serial.print("currentPos = ");
159       Serial.println(pos);
160       delay(0);
161
162     }
163 }
164
165
166 // Function to track encoder position in real-time
167 void handleEncoder() {
168   if (digitalRead(encoderPinA) >
        digitalRead(encoderPinB)){
169     encoderCount++;
170   }
171   else{
172     encoderCount--;
173   }
174 }
175
176 // Function to perform PID computation
177 float pidController(double targetP, double currentP,
      float Kp, float Kd, float Ki){
178
179   // Time elapsed since last iteration
180   long currentTime = micros();
181   deltaT = ((float)(currentTime - previousTime)) / 1.0e6;
182
```

```
183   // Compute PID errors
184   e = targetP - currentP;
185   eDerivative = (e - ePrevious) / deltaT;
186   eIntegral = eIntegral + e*deltaT;
187
188   // Compute and display PID results
189   double u = Kp*e + Kd*eDerivative + Ki*eIntegral;
190   Serial.print("e_P = ");
191   Serial.print(Kp*e, 4);
192   Serial.print(", ");
193   Serial.print("e_D = ");
194   Serial.print(Kd*eDerivative, 4);
195   Serial.print(", ");
196   Serial.print("e_I = ");
197   Serial.print(Ki*eIntegral, 4);
198   Serial.print(", ");
199   Serial.print("e = ");
200   Serial.print(u, 4);
201   Serial.print(", ");
202
203   // Update variables for next iteration
204   previousTime = currentTime;
205   ePrevious = e;
206
207   return u;
208 }
209
210 // Function to move motor to achieve input encoder
      position
211 void setMotor(int pos, int setPos){
212   if (abs(setPos-pos) > pTolerance){
213     if (setPos - pos > 0){
214       digitalWrite(DIR, 1);
215       analogWrite(PWM, maxPWM);
216     }
217     else if (setPos - pos < 0){
```

```
218         digitalWrite(DIR, 0);
219         analogWrite(PWM, maxPWM);
220       }
221     }
222 }
223
224 // Function to calibrate valve zero position
225 void calibratePos(){
226
227   // Reset PID errors
228   e = 0;
229   eDerivative = 0;
230   eIntegral = 0;
231   ePrevious = 0;
232
233   // Open valve for 1 second in case valve is already
        closed
234   digitalWrite(DIR, 1);
235   analogWrite(PWM, 255);
236   delay(1000);
237   analogWrite(PWM, 0);
238
239   // Keep closing valve until valve doesn't move (i.e.
        closed)
240   while (calibrated == 0){
241
242     // Move valve for 0.25s and track encoder
          before-after positions
243     int tempA = encoderCount;
244     digitalWrite(DIR, 0);
245     analogWrite(PWM, 255);
246     delay(250);
247     int tempB = encoderCount;
248
249     // If valve hasn't moved, calibration is DONE and
          countdown until start of PID loop
```

```
250       if (tempB - tempA == 0 && (abs(tempA)<5 &&
              abs(tempB) < 5) == 0){
251         zeroPos = encoderCount; // Calibrate encoder zero
                position
252         calibrated = 1; // Switch calibration binary
253         digitalWrite(DIR, 0);
254         analogWrite(PWM, 0); // Stop motor
255         Serial.println(" ");
256         Serial.println("CALIBRATION DONE");
257         delay(1000);
258         Serial.print("Five. ");
259         delay(1000);
260         Serial.print("Four. ");
261         delay(1000);
262         Serial.print("Three. ");
263         delay(1000);
264         Serial.print("Two. ");
265         delay(1000);
266         Serial.println("One. ");
267         delay(1000); //Complete 5s countdown before PID
                loop
268       }
269     }
270 }
```

Listing C.1: Full Arduino code for the PID controller.